UNIVERSITÀ DELLA CALABRIA

DIPARTIMENTO DI INGEGNERIA INFORMATICA, MODELLISTICA,

ELETTRONICA E SISTEMISTICA

DIMES

DOTTORATO DI RICERCA IN

Information and Communication Engineering for Pervasive Intelligent Environments

XXIX Ciclo

TITOLO TESI

Design of point contact solar cell by means of 3D numerical simulations

Settore Scientifico Disciplinare: ING-INF/01 ELETTRONICA

Coordinatore: Ch.mo Prof. Felice Crupi

Firma Felice Crupi

Supervisore/Tutor: Ch.mo Prof. Felice Crupi

Firma Felice Crupi

Dottoranda: Noemi Lisette Guerra González

Firma Noemi Lisette Guerra

Declaration of Authorship

I, Noemi Lisette Guerra González, declare that this thesis titled, "Design of point contact solar cell by means of 3D numerical simulations" and the work presented in it are my own. I confirm that:

- This work was done wholly or mainly while in candidature for a research degree at this University.
- Where any part of this thesis has previously been submitted for a degree or any other qualification at this University or any other institution, this has been clearly stated.
- Where I have consulted the published work of others I have clearly referenced them.
- Where I have quoted from the work of others, the source is always given. With the exception of such quotations, this thesis is entirely my own work.
- I have acknowledged all main sources of help.
- Where thesis content is based on work done by myself jointly with others, I have made clear what was done by others and what I have contributed myself.

Signed:

Date:

"Electric power is everywhere present in unlimited quantities and can drive the world's machinery without the need of coal, oil, gas, or any other of the common fuels."

"The sun is the spring that drives all."

Nikola Tesla (1856-1943)

Abstract

Nikola Tesla said that "the sun maintains all human life and supplies all human energy". As a matter of fact, sun furnishes with energy all forms of living, e.g., starting from the photosynthesis process, plants absorb solar radiation and convert it into stored energy for growth and development, thus supporting life on earth. For this reason, sun is considered one of the most important and plentiful sources of renewable energies. This star is about 4.6 billion years old with another 5 billion years of hydrogen fuel to burn in its lifetime. This characteristic gives to all living creatures a sustainable and clean energy source that will not run out anytime soon. In particular, solar power is the primary source of electrical and thermal energy, produced by directly exploiting the highest levels of the irradiated energy from the sun to our planet. Therefore, solar energy offers many benefits such as no-releasing greenhouse gases (GHG_s) or other harmful gases in the atmosphere, it is economically feasible in urban and rural areas, and evenly distributed across the planet. Moreover, as it was mentioned above, solar power is also essentially infinite, reason why it is close to be the largest source of electricity in the world by 2050. On the other hand, most of the energy forms available on earth arise directly from the solar energy, including wind, hydro, biomass and fossil fuels, with some exceptions like nuclear and geothermal energies.

Accordingly, solar photovoltaic (PV) is a technology capable of converting the inexhaustible solar energy into electricity by employing the electronic properties of semiconductor materials, representing one of the most promising ways for generating electricity, as an attainable and smart option to replace conventional fossil fuels. PV energy is also a renewable, versatile technology that can be used for almost anything that requires electricity, from small and remote applications to large, central power stations. Solar cell technology is undergoing a transition to a new generation of efficient, low-cost products based on certain semiconductor and photoactive materials. Furthermore, it has definite environmental advantages over

competing electricity generation technologies, and the PV industry follows a pro-active life-cycle approach to prevent future environmental damage and to sustain these advantages. An issue with potential environmental implications is the decommissioning of solar cell modules at the end of their useful life, which is expected to about 30 years. A viable answer is recycling or re-used them in some ways when they are no longer useful, by implementing collection/recycling infrastructure based on current and emerging technologies. Some feasibility studies show that the technology of end-of-life management and recycling of PV modules already exists and costs associated with recycling are not excessive. In particular, Photovoltaic is a friendly and an excellent alternative to meet growing global energy-demand by producing clean and sustainable electricity that can replace conventional fossil fuels and thus reducing the negative greenhouse effects (see section 1.1).

Reasoning from this fact, solar cell specialists have been contributing to the development of advanced PV systems from a costly space technology to affordable terrestrial energy applications. Actually, since the early 1980s, PV research activities have been obtaining significant improvements in the performance of diverse photovoltaic applications. A new generation of low-cost products based on thin films of photoactive materials (e.g., amorphous silicon, copper indium diselenide (CIS), cadmium telluride (CdTe), and film crystalline silicon) deposited on inexpensive substrates, increase the prospects of rapid commercialization. In particular, the photovoltaic industry has focused on the development of feasible and high-efficiency solar cell devices by using accessible semiconductor materials that reduce production costs. Nonetheless, photovoltaic applications must improve their performance and market competitiveness in order to increase their global install capacity. In this context, the design of innovative solar cell structures along with the development of advanced manufacturing processes are key elements for the optimization of a PV system. Nowadays, TCAD modeling is a powerful tool for the analysis, design, and manufacturing of photovoltaic devices. In fact, the use of a properly calibrated TCAD model allows investigating the operation of the studied solar cells in a reliable and

a detailed way, as well as identifying appropriate optimization strategies, while reducing costs, test time and production.

Thereby, this Ph.D. thesis is focused on a research activity aimed to the analysis and optimization of solar cells with Interdigitated Back Contact (IBC) crystalline silicon substrate *c*-Si, also known as Back Contact-Back Junction (BC-BJ). This type of solar cell consists of a design where both metal contacts are located on the bottom of the silicon wafer, simplifying the cell interconnection at module-level. Characteristics that guarantee high-conversion efficiency η due to the absence of front-contact shadowing losses. In particular, the main purpose of this thesis is to investigate the dominant physical mechanisms that limit the conversion efficiency of these devices by using electro-optical numerical simulations. Three-dimensional ($3D$) TCAD-based simulations were executed to analyze the performance of an IBC solar cell featuring point-contacts (PC) as a function of the metallization fraction. This scheme was also compared with a similar IBC structure featuring linear-contacts (LC) on the rear side of the device. In addition, the impact of introducing a selective emitter scheme (SE) in the PC cell was evaluated. The analyses were carried out by varying geometric and/or process parameters (for example, the size and shape of metal-contacts, doping profiles, carrier lifetime, and recombination rates). This approach provides a realistic and an in-depth view of the behavior of the studied IBC solar cells and also furnishes with useful information to optimize the architecture design of the device in order to enhance the conversion efficiency and minimize production costs.

Sommario

Nikola Tesla ha detto che "il sole mantiene tutta la vita umana e fornisce tutta l'energia umana". Infatti, il sole fornisce energia a tutte le forme di vita, ad esempio, partendo dal processo di fotosintesi, le piante assorbono la radiazione solare e lo trasformano in energia immagazzinata per la crescita e lo sviluppo, sostenendo così la vita sulla terra. Per questo motivo, il sole è considerato una delle fonti più importanti e abbondanti di energia rinnovabile. Questa stella ha circa 4,6 miliardi di anni e ha una quantità di combustibile (idrogeno) in grado di farla bruciare per altri 5 miliardi di anni. Questa caratteristica dona a tutte le creature viventi una sorgente di energia sostenibile e pulita che non si esaurirà presto. In particolare, l'energia solare è la fonte primaria di energia elettrica e termica, prodotta direttamente sfruttando l'energia irradiata dal sole al nostro pianeta. Pertanto, l'energia solare offre molti vantaggi come il fatto di non rilasciare gas serra (GHG) o altri gas nocivi nell'atmosfera, è economicamente sostenibile nelle aree urbane e rurali ed è distribuita uniformemente in tutto il pianeta. Inoltre, come accennato in precedenza, l'energia solare è praticamente infinita, motivo per cui sarà la più grande fonte di elettricità nel mondo entro il 2050. D'altro canto, la maggior parte delle forme di energia disponibili sulla terra nascono direttamente dalla energia solare, compresi vento, idrocarburi, biomasse e combustibili fossili, con alcune eccezioni che includono l'energia nucleare e geotermica.

Di conseguenza, il fotovoltaico (PV) è una tecnologia in grado di trasformare l'inesauribile energia solare in energia elettrica utilizzando le proprietà elettroniche dei materiali semiconduttori. Questi materiali rappresentano uno dei modi più promettenti per la generazione dell'elettricità, e sono un'opzione accessibile e intelligente per sostituire i combustibili fossili convenzionali. L'energia fotovoltaica è anche una tecnologia rinnovabile e versatile che può essere utilizzata per quasi tutto ciò che richiede energia elettrica; dalle applicazioni più piccole e remote alle grandi centrali elettriche. La tecnologia delle celle solari è in fase di transizione verso

una nuova generazione di prodotti efficienti e a basso costo basati su specifici materiali semiconduttori e foto-attivi. Inoltre, ha vantaggi ambientali rispetto alle tecnologie di produzione di energia elettrica concorrenti visto che l'industria PV segue un approccio proattivo al ciclo di vita per prevenire futuri danni ambientali. Un potenziale problema ambientale è lo smaltimento dei moduli solari alla fine della loro vita utile, che è prevista a circa 30 anni. Una risposta valida è riciclarli o riutilizzarli in qualche modo, implementando infrastrutture di raccolta/riciclaggio basate sulle tecnologie attuali ed emergenti. Alcuni studi sulla sostenibilità dimostrano che la tecnologia della gestione finale e il riciclo dei moduli fotovoltaici è già esistente e i costi associati al riciclaggio non sono eccessivi. In particolare, il PV rappresenta un'ottima alternativa per soddisfare la costante domanda di energia in tutto il mondo attraverso la produzione di energia elettrica pulita con lo scopo di sostituire i combustibili fossili è in questo modo ridurre l'effetto serra (vedere paragrafo 1.1).

Visto ciò, specialisti sulle celle solari hanno contribuito allo sviluppo di sistemi PV avanzati partendo da una costosa tecnologia spaziale ottenendo applicazioni energetiche terrestri a prezzi accessibili. Infatti, sin dai primi anni '80, l'attività di ricerca in questo settore ha ottenuto notevoli miglioramenti nel funzionamento e le prestazioni di diverse applicazioni fotovoltaiche. Una nuova generazione di prodotti a basso costo basati su film sottili di materiali foto-attivi (ad esempio, silicio amorfo, disinuro di indio di rame (CIS), cadmio telluride (CdTe) e silicio cristallino) depositati su substrati poco costosi, aumentano le prospettive di una rapida commercializzazione. In particolare, l'industria del settore fotovoltaico si è focalizzata sullo sviluppo di dispositivi di celle solari affidabili e ad alta efficienza, garantendo allo stesso tempo un abbattimento dei costi di produzione mediante l'utilizzo di materiali semiconduttori accessibili. Tuttavia, le applicazioni fotovoltaiche devono migliorare le proprie prestazioni e la competitività sul mercato in modo tale da incrementare la capacità d'installazione globale. In tale contesto, la progettazione di strutture innovative di celle solari insieme allo sviluppo di avanzati processi di fabbricazione sono elementi fondamentali per l'ottimizzazione di un sistema PV. Oggigiorno,

la modellazione TCAD rappresenta un potente strumento di supporto all' analisi, progettazione e fabbricazione dei dispositivi fotovoltaici. Difatti, l'utilizzo di un modello TCAD adeguatamente calibrato consente di investigare in modo affidabile e approfondito il funzionamento delle celle solari sotto esame e di conseguenza individuare opportune strategie di ottimizzazione, riducendo allo stesso tempo i costi e i tempi di test e produzione.

A tal proposito, questa tesi di dottorato è orientata su un'attività di ricerca finalizzata all'analisi e all'ottimizzazione di celle solari con substrato di silicio cristallino *c*-Si di tipo Interdigitated Back Contact (IBC), anche conosciute come Back Contact-Back Junction (BC-BJ). Questa tipologia di cella solare è costituita da un disegno in cui entrambi i contatti metallici si trovano sulla parte posteriore del wafer di silicio, semplificando l'interconnessione delle celle a livello di modulo. Caratteristiche che garantiscono elevate efficienze di conversione η a causa dell'assenza di perdite di ombreggiatura frontali. In particolare, lo scopo principale di questo lavoro di tesi è quello di indagare i meccanismi fisici dominanti che limitano l'efficienza di conversione di questi dispositivi mediante l'utilizzo di simulazioni numeriche elettro-ottiche di dispositivo. Sono state eseguite simulazioni TCAD tridimensionali ($3D$) per analizzare le prestazioni di uno schema di cella solare IBC a contatti posteriori puntuali (PC) in funzione della frazione di metallizzazione, confrontate con quelle di una struttura IBC analoga con contatti lineari (LC) sul lato posteriore. In aggiunta, è stato valutato l'impatto dell'introduzione di uno schema ad emettitore selettivo (SE) nella cella PC. Le analisi sono state effettuate variando diversi parametri geometrici e/o di processo (ad esempio, le dimensioni e la forma dei contatti metallici, i profili di drogaggio, il tempo di vita dei portatori e i tassi di ricombinazione). Tale approccio fornisce una visione realistica e approfondita del funzionamento delle celle solari IBC studiate e offre inoltre informazioni utili per ottimizzare la progettazione del dispositivo allo scopo di incrementare l'efficienza di conversione e ridurre al minimo i costi di produzione.

Acknowledgements

First and foremost, I thank God Almighty for the blessings He has bestowed upon me and for giving me the strength and wisdom to achieve this dream. This doctoral thesis is in its current form due to the assistance and encouragement of several people. It is a pleasure to express my sincere thanks to all those who helped me for the success of this study and made it an unforgettable experience. I express my heartfelt gratitude to my advisor Prof. Felice Crupi. Words are insufficient to appreciate my professor for his earnest involvement, inspiration and constant support during the entire period of this research work. I especially thank him for the care, empathy, and kindness, always willing to support his students, encouraging all of us with such an enthusiastic and positive attitude, and a big smile!

I would also like to thank the Panamanian government represented by the Institute for Training and Benefit of Human Resources (IFARHU) and the Technological University of Panama (UTP) which financially supported my research activities and my stay in Italy. I express my sincere thanks to all the professors and staff of the Department of Computer Engineering, Modeling, Electronic, and Systems Engineering (DIMES) for their support and cooperation during the period of this work. My appreciation also extends to my great laboratory colleagues Silvio, Sebastiano, Antoñito, Fany, Domenico, Francesco, Vincenzo, Fabio, Paul and also to our students, Massimo, Ernesto, Rosita, Ximena, Paolo, Gianluigi, Giuseppe, Maksym, Luigi, Cesar, Francesco, Giorgio, Alessandro, Angelo, Stef e Marcos. I am thankful for the support and guidance received over these years from Dr. Raffaele de Rose and Prof. Marco Lanuzza. I am extremely grateful and indebted to my unforgettable fellows and friends Eliana, Marco, Paoligno, Estelita and Rami "Los papacitos" for all their love, kindness, honesty, fun and support especially in difficult times.

I am extremely fortunate and blessed to have such caring and loving parents, Mr. Walter Guerra and Mrs. Noemi González, my gorgeous sisters, Madeline, Geneva, Cristy, and Wilka, and my adorable nephews and nieces, Alexander, Walter, Jhared, Madelaine, Giovanna and Naomi Lue. My brothers in law Einar and Jayson, as well as all my cousins, aunties, and uncles. My dream of completing this work would not have blossomed without their wholehearted support, sacrifice, and prayers. They deserve special mention for providing me with all the opportunities to explore my potentials and pursue my dreams ever since I was a child. "Por esto y muchas cosas más, este logro lo dedico de manera especial a mi hermosa Familia". ¡Ustedes son la razón de mi existir!.

Special and sincere word of gratitude to my beloved Italian and foreign friends Antonello, Biagio, Nicola, Tonino, Raffaele, Roberto, Anto, Giulia, Vin, Paol@, Luciano, Naru, Bruno, Michela, Gianfranco, Francesc@, Rossella, Mateo, Rosy, Daniela, M^{a}Domenica, Hamady, Emy, Emilia^2, Navin, Laura, Maria, Caro, Jime, Andre, Ale, Marce, Mauri, Gianluca, Silvio, Mirian, Yairis, Freddy, Ilaria, Marco, Ivan, Bartek, Mis chicos Unical, Edo, Peppe, Claudia, Sara, M^{a}Francesca, Erica, Stefano, Carlitos, Mario, Alberto, Anna, Natale, Sari and all the beautiful people I have met during this long journey. I just want to tell them: Ragazzi, mi mancherete molto!. And last but not least, I would like to place my special thanks to my precious friends from Panama and from around the world for encouraging me and lending me their helping hand in this adventure.

Noemi Lisette

Contents

List of Figures

List of Tables

List of Abbreviations

1D	**One-Dimensional**
2D	**Two-Dimensional**
3D	**Three-Dimensional**
ADEPT	**A Device Emulation Program and Toolbox**
Ag	**Silver**
Al	**Aluminum**
AM1.5G	**Air Mass 1.5 Global Spectrum**
AMPS-1D	**Analysis of Microelectronic and Photonic Structure in 1D**
ANU	**Australian National University**
ARC	**Anti-Reflective Coating**
a-Si	**Amorphous Silicon**
BGN	**Band-Gap Narrowing**
BSF	**Back-Surface Field**
BSR	**Back Surface Reflection**
BTE	**Boltzmann Transport Equation**
CdTe	**Cadmium Telluride**
CIGS	**Copper Indium Gallium Selenide**
CIS	**Copper Indium Selenide**
COP21	**21st Conference of the Parties / Paris Climate Conference**
CPV	**Concentrated Photovoltaics**
c-Si	**Monocrystalline Silicon**
CVD	**Chemical Vapor Deposition**
Cz-Si	**Czochralski Silicon**
DESSIS	**Device Simulation for Smart Integrated Systems**
DD	**Drift-Diffusion**
DoE	**Design of Experiments**
DP	**Double Screen-Printing**

EDA	**Electronic Design Automation**
ESP	**Electroless Silver Plating**
FDTD	**Finite-Difference Time-Domain**
FEM	**Finite-Element Method**
FMM	**Fourier Modal Method**
FSF	**Front-Surface Field**
Fz-Si	**Float-zone Silicon**
GaAs	**Gallium Arsenide**
GHE	**Green House Effect**
GHGs	**Green House Gasses**
GISS	**Goddard Institute for Space Studies**
GISTEMP	**GISS Surface Temperature Analysis**
HE	**Homogeneous Emitter**
HOOP	**Highly-Doped**
I-V	**Current-Voltage**
LFC	**Laser Firing Contact**
LID	**Light-induced degradation**
LOOP	**Lowly-Doped**
LOTI	**Land-Ocean Temperature Index**
mc-Si	**Multi-crystalline Silicon**
NASA	**National Aeronautics and Space Administration**
NaOH	**Dilute Caustic Soda**
NOAA	**National Oceanic and Atmospheric Administration**
PC1D	**Personal Computer One Dimensional**
PECVD	**Plasma Enhanced Chemical Vapor Deposition**
PERC	**Passivated Emitter and Rear Cell**
PERL	**Passivated Emitter Rear Locally diffused**
POE	**Partial Differential Equation**
PUPHS	**Purdue University Program for Hetero-junction Simulation**
PV	**Photovoltaics**
QNR	**Quasi-Neutral Region**
RCWA	**Rigorous Coupled Wave Analysis**
RPA	**Random-Phase Approximations**
RPC	**Rear Point Contact**

RT	**Ray-Tracing**
SCAP1D	**Solar Cell Analysis Program, One-Dimensional**
SE	**Selective Emitter**
SEM	**Scanning Electron Microscope**
Si	**Silicon**
Si02	**Silicon Dioxide**
SiNx	**Silicon Nitride**
SNMESH	**Sentaurus Mesh**
SP	**Single Screen-Printing**
SQ	**Shockley-Queisser**
SRH	**Shockley-Read Hall**
SRV	**Surface Recombination Velocity**
TCAD	**Technology Computer Aided Design**
TFSSP	**Thin-Film Semiconductor Simulation Program**
TMM	**Transfer Matrix Method**
UN-FCCC	**United Nations Framework Convention on Climate Change**
USNW	**University of North South Wales**

Physical Constants

c_0	speed of light in vacuum	$(299\,792\,458\,\mathrm{m\,s^{-1}})$
ϵ_0	vacuum permittivity	$(8.854\,187 \times 10^{-12}\,\mathrm{A\,s\,V^{-1}\,m^{-1}})$
F	Faraday constant	$(96\,485.3365\,\mathrm{A\,s\,mol^{-1}})$
h	Planck constant	$(6.626\,069 \times 10^{-34}\,\mathrm{J\,s})$
k_B	Boltzmann constant	$(1.380\,649 \times 10^{-23}\,\mathrm{J\,K^{-1}})$
μ_0	vacuum permeability	$(4\pi \times 10^{-7}\,\mathrm{V\,s\,A^{-1}\,m^{-1}})$
q	elementary charge	$(1.602 \times 10^{-19}\,\mathrm{C})$
σ	Stefan-Boltzmann constant	$(5.670\,373 \times 10^{-8}\,\mathrm{W\,m^{-2}\,K^{-4}})$
Z_0	impedance of free space	$(367.7\,\Omega)$

List of Symbols

$\alpha(\lambda)$	Absorption coefficient	cm^{-1}
$\Delta\eta$	Efficiency variation	$\%_{abs}$
Δn	Variation electron density	cm^{-3}
Δp	Variation hole density	cm^{-3}
ε	Electromagnetic permittivity	$\mathrm{F\,cm}^{-1}$
ξ	Electric field intensity, or correlation length	$\mathrm{V\,m}^{-1}$ or µm
ξ_m	Maximum electric field intensity	$\mathrm{V\,m}^{-1}$
η	Power conversion efficiency	%
η_c	Quantum collection efficiency	%
θ	Angle of incidence of the radiation	$^\circ$
λ	Wavelength	nm
μ_n	Electron mobility	$\mathrm{cm}^2\,\mathrm{V}^{-1}\,\mathrm{s}^{-1}$
μ_p	Hole mobility	$\mathrm{cm}^2\,\mathrm{V}^{-1}\,\mathrm{s}^{-1}$
ρ	Charge density	$\mathrm{C\,cm}^{-3}$
ρ_c	Specific contact resistivity	$\Omega\,\mathrm{cm}^2$
ρ_m (or ρ_f)	Metal finger resistivity	$\Omega\,\mathrm{cm}$
σ_A	Standard deviation of the finger cross-section	$\mu\mathrm{m}^2$
σ_H	Standard deviation of the finger height	µm
σ_n	Electron capture cross-section	cm^2
σ_p	Hole capture cross-section	cm^2
φ	Electrostatic potential	V
φ_0	Built-in electrostatic potential	V
$\Phi(\lambda)$	Incident photon flux	$\mathrm{s}^{-1}\,\mathrm{cm}^{-2}$
Φ_b	Barrier height at metal/semiconductor interface	eV
Φ_F	Fermi potential	V
Φ_n	Quasi-Fermi potential for electrons	V
Φ_p	Quasi-Fermi potential for holes	V
T_{Bulk}	Bulk minority carrier recombination lifetime	s
τ_{eff}	Effective minority-carrier recombination lifetime	s
τ_n	Recombination lifetime for electrons	s
τ_p	Recombination lifetime for holes	s
ν	Frequency	s^{-1}
χ	Electron affinity	eV

$A(\lambda)$	Absorbance	%
A_m	Finger cross-section area	μm^2
B	Radiative recombination coefficient	$cm^3\,s^{-1}$
CF_{rear}	Rear contact fraction	%
C_n	Auger coefficient for electrons	$cm^6\,s^{-1}$
C_p	Auger coefficient for holes	$cm^6\,s^{-1}$
C_{peak}	Peak surface doping concentration	cm^{-3}
D_n	Electron diffusion coefficient	$cm^2\,s^{-1}$
D_p	Hole diffusion coefficient	$cm^2\,s^{-1}$
D_{sub}	Wafer thickness	µm
E_C	Conduction band edge energy	eV
E_F	Fermi level	eV
E_{Fn}	Quasi-Fermi level for electrons	eV
E_{Fp}	Quasi-Fermi level for holes	eV
E_g	Energy band-gap	eV
$E_{g,eff}$	Effective energy band-gap	eV
$E_{ph}(\lambda)$	Photon energy	eV
$EQE(\lambda)$	External quantum efficiency	%
E_V	Valence band edge energy	eV
F	Finger area factor	*numerical value*
F_n	Geometric factor for electrons	*numerical value*
F_p	Geometric factor for holes	*numerical value*
FF	Fill factor	%
G	Net generation rate	$cm^{-3}\,s^{-1}$
G_{opt}	Optical generation rate	$cm^{-3}\,s^{-1}$
H_{bb}	Busbar height	µm
H_{fm} (or H_m)	Front finger height	µm
I_{in}	Incident solar irradiance	$W\,m^{-2}$
$IQE(\lambda)$	Internal quantum efficiency	%
J_0 (or $J_{0,tot}$)	Saturation current density	$A\,cm^{-2}$
$J_{0,b}$	Base saturation current density	$A\,cm^{-2}$
$J_{0,BSF}$	BSF saturation current density	$A\,cm^{-2}$
$J_{0,e}$	Emitter saturation current density	$A\,cm^{-2}$
$J_{0,min}$	Minimum saturation current density	$A\,cm^{-2}$
J_{depth}	Junction depth	µm
J_{in}	Incident photon current density	$A\,cm^{-2}$
J_L (or J_{ph})	Photogenerated current density	$A\,cm^{-2}$
J_{mpp}	Current density at maximum power point	$A\,cm^{-2}$
J_n	Electron current density	$A\,cm^{-2}$
J_p	Hole current density	$A\,cm^{-2}$
J_{sc}	Short-circuit current density	$A\,cm^{-2}$
$J_{sc,max}$	Maximum short-circuit current density	$A\,cm^{-2}$

κ_{lambda}	Extinction coefficient (imaginary part of the refractive index)	*numerical value*
k	Boltzmann constant	$\mathrm{J\,K^{-1}}$
L_{bb}	Busbar length	cm
L_{fm} (or L_m)	Front finger length	cm
L_n	Diffusion length for electrons	cm
L_p	Diffusion length for holes	cm
L_T	Transport length	cm
m_e^*	Effective mass for electrons	g
m_p^*	Effective mass for holes	g
n	Electron concentration	$\mathrm{cm^{-3}}$
$\tilde{n}$	Complex refractive index	*numerical value*
$\tilde{n}_\lambda$	Real part of the complex refractive index	*numerical value*
n_i	Intrinsic carrier density	$\mathrm{cm^{-3}}$
$n_{i,eff}$	Effective intrinsic carrier density	$\mathrm{cm^{-3}}$
n_{n0}	Electron equilibrium concentration in n-type semiconductors	$\mathrm{cm^{-3}}$
n_{p0}	Electron equilibrium concentration in p-type semiconductors	$\mathrm{cm^{-3}}$
N_A	Acceptor density	$\mathrm{cm^{-3}}$
N_C	Effective density of states in the conduction band	$\mathrm{cm^{-3}}$
N_D	Donor density	$\mathrm{cm^{-3}}$
N_{dop}	Net doping density	$\mathrm{cm^{-3}}$
N_s	Surface doping concentration	$\mathrm{cm^{-3}}$
$N_{s,chem}$	Chemical surface doping concentration	$\mathrm{cm^{-3}}$
N_{sub}	Substrate doping density	$\mathrm{cm^{-3}}$
N_t	SRH trap density	$\mathrm{cm^{-3}}$
N_V	Effective density of states in the valence band	$\mathrm{cm^{-3}}$
p	Hole concentration	$\mathrm{cm^{-3}}$
P_{in}	Incident solar power	$\mathrm{W\,cm^{-2}}$
P_{mpp}	Maximum output power	$\mathrm{W\,cm^{-2}}$
P_{n0}	Hole equilibrium concentration in n-type semiconductors	$\mathrm{cm^{-3}}$
P_{p0}	Hole equilibrium concentration in p-type semiconductors	$\mathrm{cm^{-3}}$
q	Electronic charge	C
R	Net recombination rate	$\mathrm{cm^{-3}\,s^{-1}}$
$R(\lambda)$	Reflectance	$\%$
R_b	Bulk semiconductor resistance	Ω
R_{bb}	Resistance of the front busbars	Ω
R_{bc}	Back contact resistance	Ω
R_{ch}	Characteristic resistance of a solar cell	Ω
$R_{ext,front}$	External front reflectivity	*numerical value*
R_{fc}	Front contact resistance	Ω
$R_{fm} (or R_m)$	Resistance of the front metal fingers	Ω
$R_{int,back}$	Internal back reflectivity	*numerical value*
$R_{int,front}$	Internal front reflectivity	*numerical value*

R_s	Series resistance	Ω
R_{sh}	Shunt resistance	Ω
R_{sq}	Emitter sheet resistance	$\Omega \cdot sq^{-1}$
S	Interruption size	µm
S_n	Surface recombination velocity for electrons	$\mathrm{cm\,s^{-1}}$
S_p	Surface recombination velocity for holes	$\mathrm{cm\,s^{-1}}$
$SR(\lambda)$	Spectral response	$\mathrm{A\,W^{-1}}$
ν_{oc}	Normalized open-circuit voltage	*numerical value*
t	Time	s
$T(\lambda)$	Transmittance	%
T	Temperature	K
V_a	Applied bias voltage	V
V_{mpp}	Voltage at maximum power point	V
Voc	Open-circuit voltage	V
ν_{oc}	Normalized open-circuit voltage	*numerical value*
ν_{th}	Thermal velocity	$\mathrm{cm\,s^{-1}}$
W_{bb}	Busbar width	mm
W_{fm} (or W_m)	Front finger width	µm
W_{se}	Lateral width ofthe SE diffusion	µm
W_{sub}	Front contact pitch	µm
W_{wafer}	Wafer width	cm
χ_F	Interruption position	µm
ω	Angular frequency	rad

To my beautiful & beloved Family…

Chapter 1

Introduction & Background

Nowadays renewable energies are becoming an essential part of our daily life thanks to the new governmental agreements and policies that pursue at least partially replacing fossil fuels, reducing global warming below $2°$C, and achieving additional benefits. By implementing an action plan to protect our environment and by fulfilling established targets to develop renewable-energy systems we can greatly contribute to the security of the global energy supply, the reducing of greenhouse gas (GHG_s) emissions, an the solving of the climate crisis and related health issues.

Since non-renewable energy sources as well-known as fossil fuels are limited and have contributed negatively to global warming through the dramatic increment of greenhouse gas emissions, energy security has a role to play in meeting the fast and constant demand of electricity supply. Clean energies like solar power represent the best alternative to overcome the challenge of meeting a growing energy demand, which includes populations from both industrialized cities and remote areas (with long distances to a basic distribution grid electricity and where communication is not available but it is also necessary). To give a general idea of the enormous potential of the sun, consider that one ten-thousandth of the solar radiation that reaches the earth's surface is enough to cover the yearly global energy consumption. This potential capability of sun power has been well used by the denominated photovoltaic (PV) energy. PV technology consists of solar cells that directly convert sunlight into electricity at the atomic level. This can be obtained through the photovoltaic effect by using the electronic properties of semiconductor materials, which is one of the most promising energy conversion process.

PV systems offer many attractive features, including pollution-free operation, very low GHGs emissions, relatively low maintenance costs, and economical feasibility in urban and rural areas. Definitively, PV solar cells will foster many aspects related to energy supply security and industrial development by providing improved access to electricity, job opportunities welfare, increased health, and a better quality of life while reducing the negative impact of massive burning fossil fuels.

This chapter presents a concise introduction to the problem of steadily growing energy consumption and the dramatic situation of global warming due to the greenhouse gas emissions. Additionally, we will review a summary of the technological developments made in the photovoltaic industry since the middle of the 20th century.

1.1 Global warming and the energetic paradigm

Nowadays, our planet is facing enormous environmental challenges. The disorder of the greenhouse effect (GHE) is a major threat to the global climate. The GHE is a natural process that typically plays a critical role in regulating global temperature. It warms the earth's surface and contributes to maintaining the temperature approximately 15°C in average, allowing sustained life [1] on earth. Without this, the overall temperature would be much colder (i.e. -18°C average) and life on our planet would be impossible [2, 3]. This natural phenomenon was discovered in 1827 by Joseph Fourier and quantified in 1896 by Svante Arrhenius [4]. The GHE is mainly caused by the interaction of sunlight with greenhouse gases (GHG/GHG_s) and present components of the atmosphere, which can be both anthropogenic and natural gases. The main mixture of gases (also known as trace gases) related to the GHE are carbon dioxide (CO_2), methane (CH_4), water vapour (H_2O) and ozone (O_3).

A helpful comparison is to compare a greenhouse (where a trace gas acts) to a glass that allows sunlight to pass into it, but keeps the resulting heat radiation inside. These gases contributes to warming up the glass, which is similar to how the greenhouse effect works. Nonetheless, an uncontrolled concentration of GHG_s in the atmosphere can highly increase the average global temperature. In 2016, Nerilie Abram, a researcher at the Australian National University (ANU), published an article [5] revealing robust evidence about the impact of anthropogenic sources (i.e. CO_2, CO and CH_4) on climate, for more than 170 years that exactly match with the boom of the industrial revolution.

Actually, many research publications state that human activities and industrial developments are responsible for the steep rise in concentrations of greenhouse gases. Carbon dioxide, which comes out to the atmosphere because of the fossil fuel combustion (coal, gas, natural gas, or petroleum), is major contributor as result of our relentless pursuit of energy. These massive emissions probably represent the main threat for the planet's ecosystem. In fact, according to IEA the permanent use of fossil energy is responsible for approximately 85% of the high anthropogenic CO_2 emissions produced annually. Other activities such as agriculture, land clearing and deforestation also contribute negatively to the global warming [6]. To clarify the greenhouse effect on earth, examine and consider Figure 1.1, where ⓐ sunlight (visible and infrared radiation) crosses the atmosphere almost unobstructed and is ⓑ absorbed by the ground. This warms the surface ⓒ and ⓓ emits heat radiation (also called *black body*) which once again is ⓔ absorbed by the trace gases and ⓕ set free into the

environment as heat. Only a small portion of this heat energy gets back into space whereas the majority remains in the atmosphere and increases the earth's temperature [7].

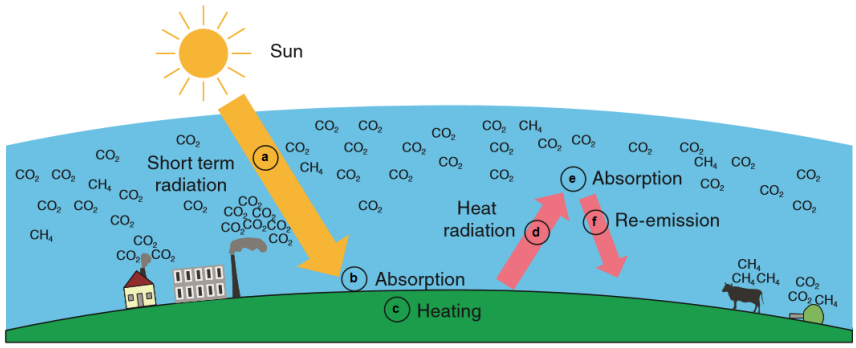

FIGURE 1.1: Greenhouse effect schematic. The heat radiation reflected from the earth surface is held back into the atmosphere by the greenhouse gases. Taken from [7].

In 2013, the concentration of CO_2 in the atmosphere reached 396-ppm (parts per million) average, a value that was never reached during millions of years, and representing 142% of the rate reported before the Industrial era (1750, taken as the reference year) [8]. Additionally, a study about the global distribution of greenhouse gas emissions that covered a timeframe from the late-20th century until 2014 shows that the annual CO_2 levels were almost exclusively from the United States and Europe, however, since 2006 China became the main CO_2 emitter, and accounted for 30% of the global emissions as depicted in Figure 1.2 [9].

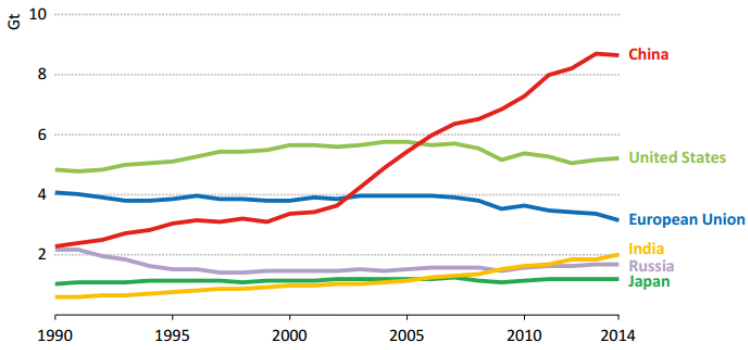

FIGURE 1.2: Energy and industrial production-related CO_2 emissions by selected region [9].

According to Japan Meteorological Agency (JMA) global warming is a reality and the day by day, increase in temperature levels and their effects is noticeable [10]. Likewise,

in January 2017 NASA & NOAA confirmed that since the 19th century, Earth's average temperature has increased to 1.1°C (2° Fahrenheit) because of the extra trapping of heat released into the atmosphere, a result of the additional emission of trace gases caused by the so-called anthropogenic greenhouse effect [11]. Moreover, a recent monthly analysis of global temperatures revealed that February 2017 was the second warmest February in 137 years of modern record-keeping (shown in Figure 1.3). For this reason, NASA's actions are fundamental to properly facing the challenge of climate change of this generation, as stated by Charles Bolden, former NASA administrator (until January 2017) [12].

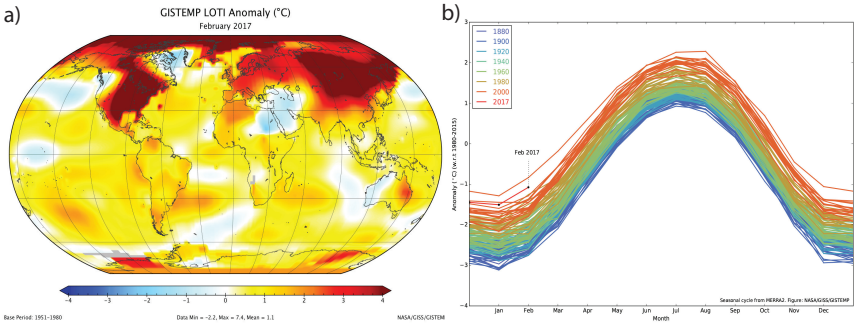

FIGURE 1.3: a) Representation of global map for February 2017 LOTI (land-ocean temperature index) anomaly evidencing that Northern countries were much warmer than they were in the 1951-1980 base period, b) GISTEMP monthly global temperature anomalies for the 1980-2017 period [12].

Consequently, governments are currently building greater commitments in order to face climate change through new global agreement policies. Opposite to the limited participation of the countries in the Protocol of Kyoto in 2005, the European Union (EU) proposed a new strategy to mitigate global warming and communicated it in December 2015 at the Paris Climate Conference (COP21), which became effective in November 2016 [13]. The Paris agreement established a global action plan to keep the long-term global mean temperature below 2°C (postulated in the Copenhagen Accord of the UN-FCCC) [14] and reducing future internal GHGs emissions (i.e. CO_2), to at least 40% average, within the next thirteen years, regarding the levels reported in 1990 [15]. Furthermore, it highlights the EU commitment of increasing the green energy quote and improving the energetic efficiency. However, in 2015 through the strategy "Europe 2020", the EU GHG_s emissions were 22% below the 1990 level. Actually, after the 20th-century emissions continue to decline over time, and a significant drop of 18% is expected by 2030 (as illustrated in Figure 1.4) [16]. Therefore, all of these guidelines are aimed at implementing a sustainable energy model where both developing and developed countries are collectively undertaking appropriate actions to avoid harmful environmental impacts, and thus, the energy sector will change to the extent necessary to meet the internationally agreed objectives.

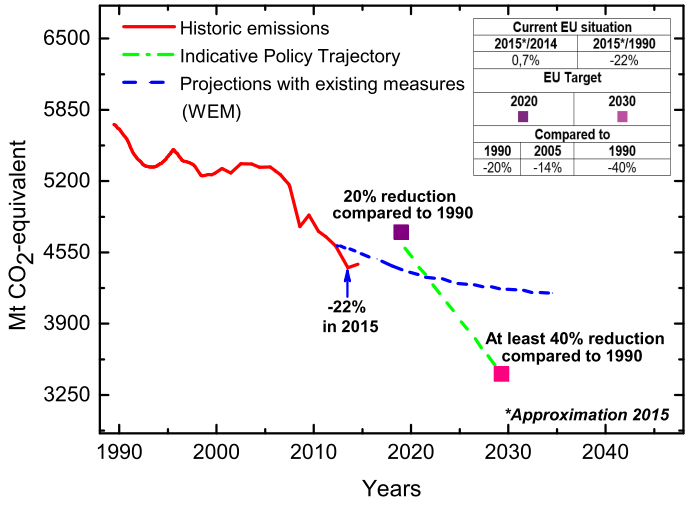

FIGURE 1.4: Progress towards the achievement of the Europe 2020 targets [16].

These government efforts are focused on specific priorities as climate protection through the reduction of carbon dioxide intensity (by 2030), and carry out a transition plan toward a new renewable energy supply system capable of meeting the energetic needs of an ever increasing population. The following is an interesting analysis based on the currently implemented policies by the International Energy Agency (IEA). After the first quarter of the 21th century, world energy demand is expected to increase by about 50% every 10 years until 2050. Figure 1.5 is a graph, which depicts the present situation and the possible future scenario for global energy supply with respect to the constant rise in energy demands and the associated dramatic increment of CO_2 emissions. Contributions from various primary energy sources (particularly coal, oil, gas, nuclear, hydro, bio-energy, among other renewable ones) are shown [9]. This shows that fossil fuels will remain as base-load electricity production, working together with renewable energy sources until 2030, and regulated by the Europe 2020 target policies.

Afterwards, the expected scenario consists of boosting alternative clean energy investments in order to furnish future energy demands, as well as overcoming fossil fuel dependence whereas energy-related CO_2 emissions will keep constant after 2040 with a possible decline of 39% over the same period. However, the fossil fuels industry continues to lead the global energy supply and to be primarily subsidized by governments (see Figure 1.6), gathering high economic incomes that probably overcome other types of technologies. This is expected despite the fact that their prices tend to increase, and renewable energy prices

tend to decrease because of continued productivity improvements and economies of scale.

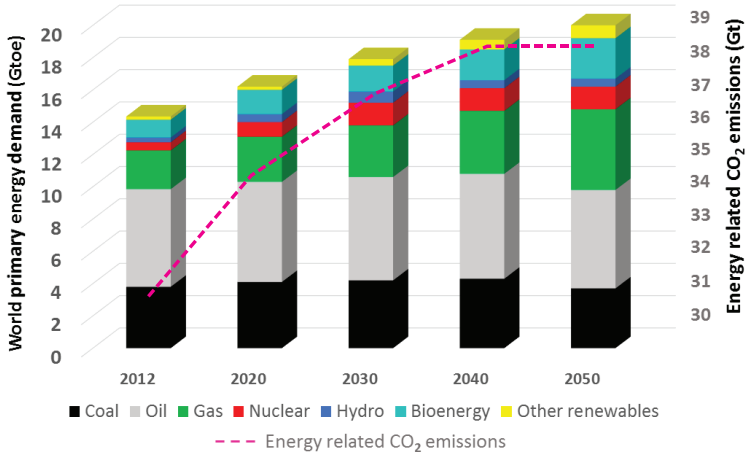

FIGURE 1.5: Estimated global primary energy supply scenario by IEA policies [9].

1.2 Facing the global energy demand by adopting renewable energy supply technologies

In this matter, a change in the way of producing and using energy is fundamental. In particular, the industry must be concerned about reducing the dependence on fossil fuels to generate electricity (coal, gas, and oil), and instead, substitute them for the development and use of eco-friendly and sustainable energy sources such as solar and wind. Among the viable options, solar energy by far represents the largest energy resource capable of fulfilling the whole energy demand of humankind (by just using one ten-thousandth part of the incoming sunlight), compared to other non-renewable sources. Thus, as being an inexhaustible and sustainable energy source that cannot be over-consumed, solar energy can easily become the world's primary energy supply. This relationship is clearly described in the schematic of the energy cube values depicted in Figure 1.7. There is a comparison between the annual solar incidental radiation, and the available reserves of fossil fuels, and nuclear energy carriers regarding the world annual energy demand. The current limited non-renewable energy sources are represented by the small boxes at the bottom-left. The solar radiation is sketched by the biggest yellow cube, representing its vast power available every new year. Conversely, at the bottom-right there is a small box of the global annual energy usage, which appears to be very small when compared to the large solar box. This is because sunlight potential is proportionally more than ten thousand times the current yearly global energy consumption.

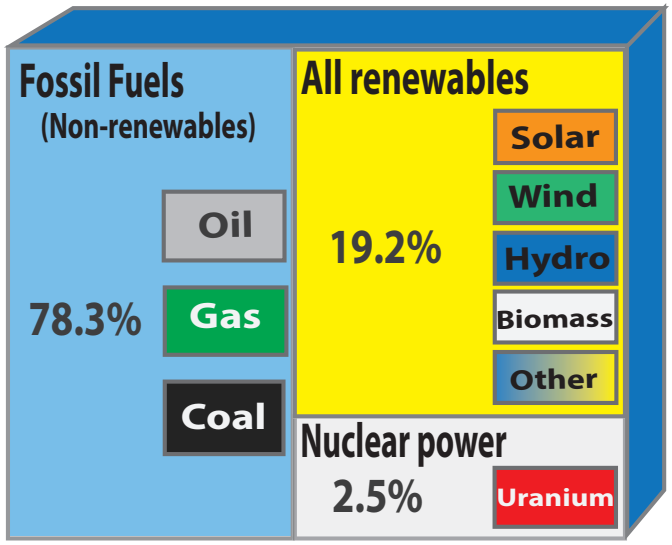

FIGURE 1.6: Estimated renewable energy share of global final energy consumption, 2014 [17].

Additionally, solar energy helps society to meet its increasing energy needs, reducing electricity costs as well as being environmentally friendly. It provides solutions for decreasing or even stopping the global warming crisis because harnessing it does not generally cause pollution, which is different and better than conventional and non-renewable energy sources. Its end wastes are already handled by current pollution controls and regulations. On the other hand, most of the today's solar power systems (including photovoltaic and solar thermal) are easily deployable at the consumer level, requiring low maintenance. The primary maintenance focuses on cleaning the solar panel a couple of times per year. Since the early 1980's technological advancements have consistently been made in the photovoltaic industry. In particular, research groups have greatly contributed to enhancing the power density and general performance of solar cell systems by exploiting the potential of nanotechnology and quantum physics. Thus, solar power clearly represents the solution of satisfying the world's future energy necessities while also significantly reducing the production of GHG emissions and negative implications for our global climate. It provides energy security and the offer of an independent way to produce electricity, because it is free and available to everyone all over the world. For these reasons, solar energy has been established as "The People's Power supply".

The map sketched in Figure 1.8 shows the solar energy potential of the European Union (EU). Despite the fact that Northern regions do not have the best location for maximum solar PV potential, the EU as a whole is producing a significant electricity quota from solar power. For instance, Germany is dominating the EU installed PV capacity, due mainly to

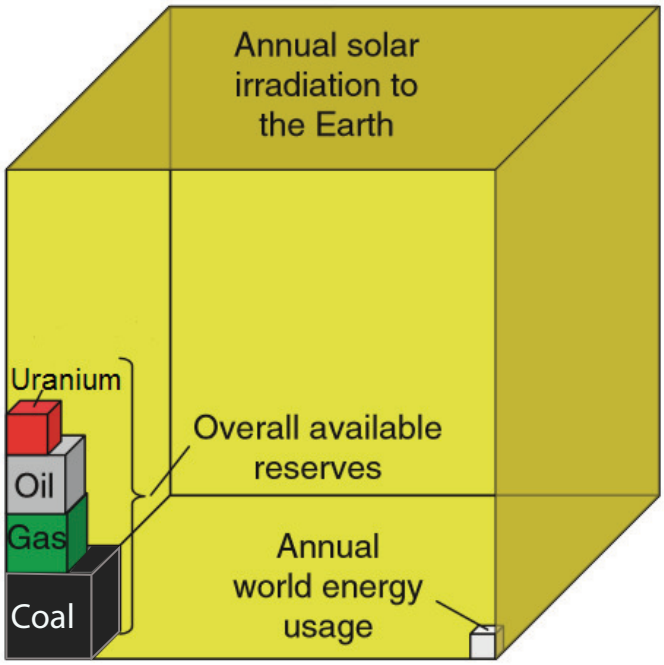

FIGURE 1.7: Schematic of the energy cubes: an estimate of the potential of solar energy. The annual solar irradiation exceeds several times the total world energy demand as well as the whole fossil fuel energy reserves. [3, 7].

the environmental concern supported by generous subsides. However, a couple of Southern countries with even greater solar potential are also making efforts to improve and accelerate actions for the sake of a low carbon society. This is the case of Italy and Greece, countries that are currently dependent on fossil fuel as the primary energy supply, but their geographic location is rather favorable for the exploitation of PV technologies. In effect, photovoltaic systems are becoming a strategic real choice, and in the case of the European Union (EU), the solar cell production supplies nearly 4% of its whole electricity demand (see Figure 1.9). This has been possible thanks to the solar contributions of 17 of the European Union's 28 members to more than 1% of their power needs. Actually, Italy, Greece and Germany have been established as the top solar electricity consumers, each producing more than 7% of their energy usage. It is worth mentioning that, in Italy around 8% of the power consumption is entirely covered by its own solar PV production. Accordingly, at the end of 2015, the production of photovoltaic plants in Italy reached 22.942 GWh. As it is shown in Figure 1.10 the increase compared to 2014 (+ 2.9%) is lower than that recorded in previous years. Looking at the performance of PV plant production throughout 2015, July recorded the largest solar capacity with nearly 3 TWh of energy produced in Italy. In effect, the chart of Figure 1.11 illustrates the daily average of solar irradiation stating that

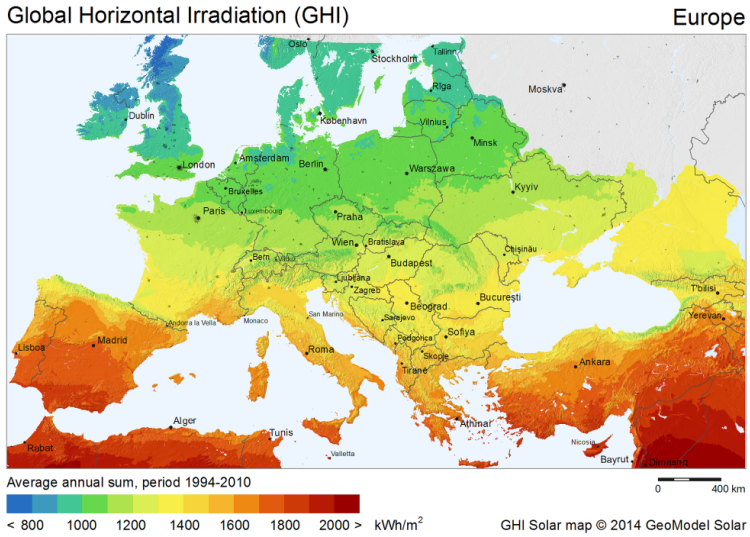

FIGURE 1.8: Global solar irradiation in European countries published by SolarGIS: Geographic Information System data and maps [18].

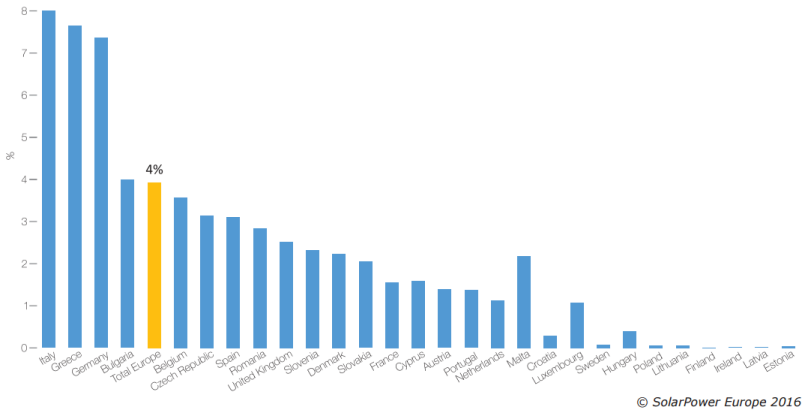

FIGURE 1.9: Share of electricity demand covered by solar photovoltaic production in European countries, 2015 [19].

July was the sunniest month of 2015. Besides, in the same month, the highest peak reached 874 W/m^2 average.

Conversely, November, December, and January had the lowest solar irradiation; and the maximum value of daylight hours was recorded in June, as it can be seen in the bell curve. Indeed, in the specific case of Southern Italy, solar production is offering a significant contribution to the alternative energy supply with the presence of companies dedicated to

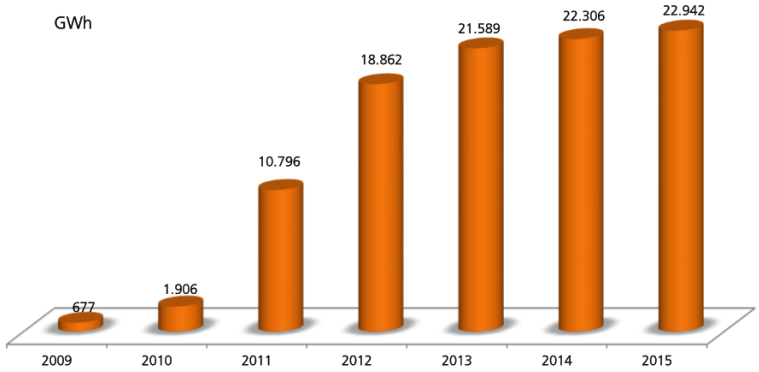

FIGURE 1.10: Annual production of photovoltaic plants in Italy (2009-2015) published by the energy service manager agency (GSE, Italy) [20, 21].

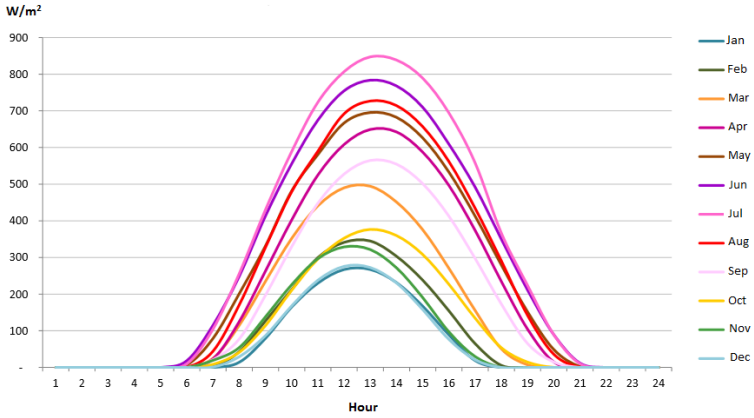

FIGURE 1.11: Hourly average of solar radiation in Italy, published by the energy service manager agency (GSE, Italy), 2015. [20].

the development of PV solutions, such as Omnia Energia (oe), certificated as the best eco-sustainable urban building in the EU (A+). In terms of fuel consumption, oe saves around 70% energy compared to traditional buildings, as well as, 83 Ton CO_2 avoided in a solar year [22]. Hence, as the benefits accomplished by implementing energy solutions based on solar power are clear in Europe, PV systems have reached an important position among the green energies portfolio of this generation.

1.3 Overview of PV recycling

The deployment of PV technology has grown dramatically in recent years, reaching a cumulative global installed capacity of 222 *GW* at the end of 2015. PV offers economic and environmentally friendly electricity production but like any technology, it ages and ultimately requires decommissioning (which includes dismantling, recycling, and disposal). As PV increasingly becomes a global commodity, and to ensure its sustainable future, stakeholders involved with each step of the product life-cycle must implement sound environmental processes and policies, including responsible *end-of-life* treatment. Regulatory frameworks that support the early development of life-cycle management techniques and technologies will foster such processes and policies [23].

The PV industry has adopted a pro-active and longterm strategy to preserve the environmentally friendly nature of the industry. Manufacturing solar panels presents some health, safety and environmental *HSE* concerns which were the focus of numerous studies at *Brookhaven National Laboratory*, under the auspices of the US Department of Energy's National Photovoltaic Program [24–26]. One issue is what to do with PV modules at the end of their use?. Modules are expected to last about 30 years, and, then will have to be decommissioned and disposed or re-used in some ways. There is a concern about disposing them in municipal landfills because they may contain small amounts of regulated materials. Environmental regulations can determine the cost and complexity of dealing with end-of-life PV modules. At present, only the European Union *EU* has adopted PV-specific waste regulations. Most countries around the world classify PV panels as general or industrial waste. In limited cases, such as in Japan or the US, general waste regulations may include panel testing for hazardous material content as well as prescription or prohibition of specific shipment, treatment, recycling and disposal pathways. The *EU*, however, has pioneered PV electronic waste *e-waste* regulations, which cover PV-specific collection, recovery and recycling targets. Based on the extended producer responsibility principle, the EU Waste Electrical and Electronic Equipment *WEEE* Directive requires all producers supplying PV panels to the EU market (wherever they may be based) to finance the costs of collecting and recycling *end-of-life* PV panels put on the market in Europe. Lessons can be learned from the experience of the *EU* in creating its regulatory framework to help other countries develop locally appropriate approaches. The PV recycling industry is expected to expand significantly over the next 10-15 years. Annual *end-of-life* PV panel waste is projected to increase to more than $60-78$ million metric tonnes cumulatively by 2050 according to [23] (see Fig. 1.12). This increasing scale should improve the cost-effectiveness and energy/resource efficiency of recycling while stimulating the technical innovations needed to handle the wide variety of materials used in fast-evolving PV technologies.

Based on the best available information today and according to [9, 23] the next graphic suggests the actual future PV panel waste volumes considering a regular-loss scenario. Regarding to the probability of PV panels becoming waste before reaching their estimated

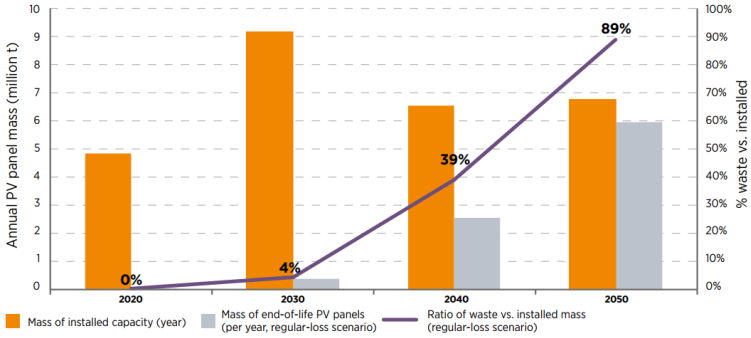

FIGURE 1.12: Annually installed and end-of-life PV panels 2020-2050 (in % waste vs. t installed) by a regular-loss scenario. Based on [9, 23].

end-of-life targets, the potential origin of failures for rooftop and ground-mounted PV panels has been analyzed independently from the PV technology and application field [9, 23]. Basically, the three main panel failure phases detected are the following (see Fig. 1.13):

- Infant failures defined as occurring up to four years after installation (average two years),
- Midlife failures defined as occurring about five to eleven years after installation,
- Wear-out failures defined as occurring about 12 years after installation until the assumed end-of-life at 30 years.

The main infant failure causes include light-induced degradation (observed in $0.5\% - 5\%$ of cases), poor planning, incompetent mounting work and bad support constructions. On the other hand, causes of midlife failures are mostly related to the degradation of the anti-reflective coating of the glass, discoloration of the ethylene vinyl acetate, delamination and cracked cell isolation. And the causes of frequently observed failures within all phases in the first 12 years after exposure to mechanical load cycles (e.g. wind and snow loads) and temperatures changes include potential induced degradation, contact failures in the junction box, glass breakage, loose frames, cell interconnect breakages and diode defects.

The operation of PV systems does not produce any noise, toxic-gas emissions, nor greenhouse gases as exposed in section 1.1. PV energy not only can help meeting the growing worldwide demand for electricity, but it can do so without incurring the high environmental costs of burning fossil fuels. Relative to burning coal, every gigawatt-hour of electricity generated by PV would prevent the emission of up to $10ton$ of sulfur dioxide, $4ton$ of nitrogen oxides, $0.7ton$ of particulates (including $1kg$ of Cd and $120kg$ of As), and up to $1000ton$ of carbon dioxide [27]. Recycling PV systems at the end of their useful life adds to the environmental benefits and can further enhance market support. Subsequently,

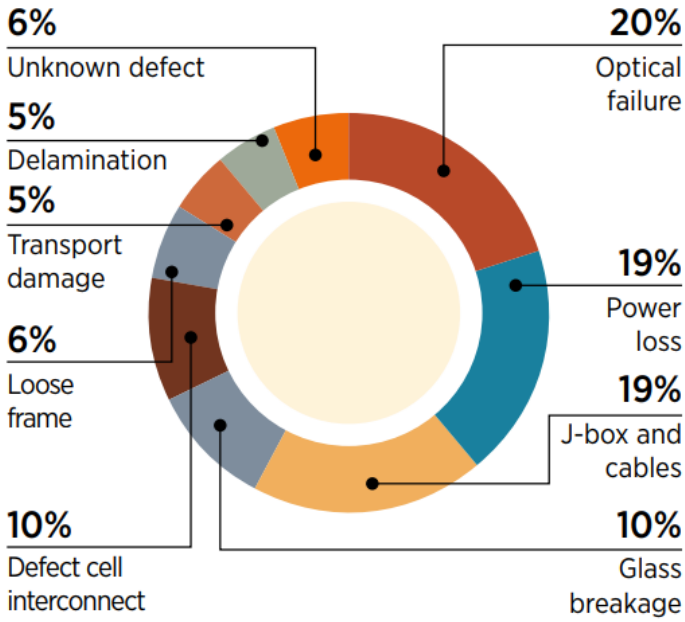

FIGURE 1.13: Failure rates on PV panels according to customer complaints. Based on [9, 23].

recycling answers public concerns about hazardous materials in PV modules which can create barriers to market penetration.

1.4 Review of PV technology developments

Photovoltaic technology is one of the foremost ways to harness solar energy. A PV cell consists of an electrical device made out of certain semiconductor materials such as Silicon, that exhibit a particular property known as the *bulk photovoltaic effect*. The PV effect is a process that causes the absorption of photons of light and releases electrons, and when these free electrons are captured, an electric current is obtained. In other words, the PV conversion directly converts sunlight (photons) into electricity (voltage) without an intermediate heat engine. The PV effect was accidentally discovered in 1839 by the French physicist Alexander-Edmond Becquerel at the age of 19 years old when he observed a light-dependent voltage between electrodes immersed in an electrolyte [28]. Nonetheless, it was not until 1954 when the scientists Daryl M. Chapin, Calvin S. Fuller and Gerald L. Pearson built the first modern silicon-based photovoltaic cell at Bell Laboratories in the United States. Practically, they discovered that silicon material can create an electric charge when exposed to sunlight. Thus, their solar cell registered an efficiency of about 6% [29].

This paramount invention defines a new era for the current and future developments in the PV industry by offering advantages as described in Table 1.1. Note that the list includes technical and environmental parameters, taking as a reference the positive and negative issues of conventional fossil-fuel power plants. Later on, laboratories started developing the first silicon solar cells to power space satellites and solar cells are considered essential in this type of application. Moreover, in the late 1970s and 1980s, the developed PV systems were focused on terrestrial applications, and the first thin-film solar cell based on copper-sulphide/ cadmium-sulphide junction amounted to an efficiency (η) above 10%. In contrast to this invention, in 1975 R. Schwartz initiated research of a new architecture known as back-contact solar cells, considered an alternative to photovoltaic cells, featuring both a front and rear contact [30]. In 1985, the University of New South Wales (UNSW) built crystalline silicon (*c*-Si) solar cells and reached efficiencies above 20%, and in 1999 they stated a new record of 25%, considered the world highest efficiency [31, 32]. The structure was also *c*-Si-based. In 1994, the National Renewable Energy Laboratory (NREL) from Colorado, U.S.A, built a solar cell based on indium-gallium-phosphide/gallium-arsenide tandem junction that exceeded 30% efficiency.

Advantages of PV technology
Quite evenly distributed energy across the planet and essentially infinite
Low emissions, no combustion or radioactive fuel for disposal
Ambient temperature operation (no high-temperature corrosion)
Low operating cost (no fuel)
Low maintenance cost
No moving parts
Quick installation
High public acceptance
Excellent safety record
High reliability in modules ($\geq 20 years$)
Modular (small or large increments)
Economically feasible in urban and rural areas
Integrated into new or existing building structures
Installed at nearly any point-of-use
Daily output peak may match local demand

TABLE 1.1: Advantages of photovoltaic technology [33].

Until the late 1990s, solar cell innovations continued to be introduced, pushing up the photovoltaic industry and the related manufacturing processes. Consequently, PV research and developments of solar cell systems were notably growing interest in North America, Europe, and Asia. To confirm this, the world total installed PV power systems in 1999 outstripped the 1 GW, defining a renewed beginning for the public discussion of solar energy, bearing in mind essential aspects such as the environment and the climate change,

economy, health and the common welfare. Afterwards, many laboratories and companies continued developing silicon photovoltaic cells, achieving new conversion efficiency records of approximately 25% as in the case of SunPower & Panasonic in 2014 [34, 35]. Over the same year, the Australian National University designed an interdigitated back contact (IBC) solar cell featuring point contacts on the rear side achieving an efficiency of 24.4%, the highest reported value to date for this promising back contact architecture [36].

Furthermore, at the end of 2016 Yoshikawa et. al from Kaneka Corporation built an interdigitated back contact (IBC) *c*-Si-based solar cell, obtaining the world's highest conversion efficiency of 26.33% [37]. Additionally, it is important to highlight that this kind of back contact-back junction (BC-BJ) solar cell structures are recognized by the many advantages over the conventional PV cells, but more complex configuration implies specific fabrication processes and higher costs. Anyhow, point contact cells have shown a pledging performance, thus representing a potential architecture to optimize by the extensive study carried out in this work [38]. It is worth mentioning, that each of these innovations have contributed significantly to the worldwide record growth of the photovoltaic market during the last years. In particular, the global cumulative capacity of PV systems have been fitting an exponential curve in the last twenty-five years, amounting from less than 1 GW at the beginning of the 1990s to a steadily rise of 242 GW reported by 2015, 302 GW in 2016 and an expected future projection of 368 GW of solar power capacity at the end of 2017, as sketched in Figure 1.14 a). Therefore, according to data compiled by the Institute for Solar Energy (Fraunhofer, ISE), it is evident that the installation of PV systems will spread rapidly to the emerging markets all over the world in the next ten years.

In fact, the installed renewable electric capacity by the end of 2015 was mainly driven by leaders such as China, Japan, United States, and the pioneering European countries as Germany, Italy, and Greece. In fact, it seems that these countries will remain a considerable influence on the worldwide renewable energy market, especially in the solar PV installations (see Figure 1.14 b)) [39, 40]. Accordingly, PV will play a significant role in the world future energy supply, as one of the best renewable sources to meet the alarming and growing energy demand. Although different types of solar cells with various kinds of semiconductor materials have been studied and produced, crystalline silicon wafer-based cells accounted for about 93% of the total production reported in 2015. It was stated as the cheaper way to produce on mass-scale, given the diffusion of facilities dedicated to the fabrication of diverse silicon applications [39]. Silicon is the second most abundant element in the Earth's crust (about 28%) after oxygen, and it is also a non-toxic material and represents a fundamental component in the microelectronic industry.

As silicon solar cells have shown satisfactory properties in creating an electric charge when exposed to sunlight, it has led the PV industry for more than the three decades and is still improving. Actually, this valuable semiconductor material offers a reliable technology that can easily achieve a large-scale deployment [41]. However, the key to accomplishing

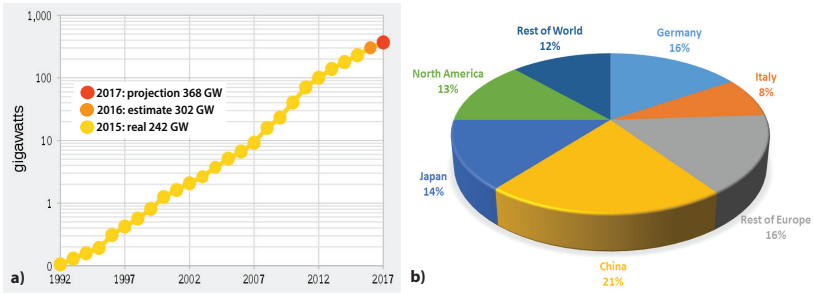

FIGURE 1.14: a) Global cumulative PV capacity, period 1992-2017, b) Global PV system installation by region, status 2015 [39, 40].

this objective is based on the understanding of the device operation and the reduction of the related loss mechanism, focusing on the optimization of the process design, increasing the conversion efficiencies, as well as, reducing manufacturing complexity and cost.

1.5 Motivation & Thesis outline

The improvement of photovoltaic solar cells in terms of increasing conversion efficiency and minimizing manufacturing costs requires a careful device optimization, including the proper architecture, design of metal-contacts, doping profiles and passivation layers, the choice of materials and the implementation of advanced light trapping strategies. In this regard, modeling of photovoltaic devices has become increasingly strategic and helpful for the PV industry in order to aid the design of solar cells, thus accelerating the optimization and at the same time, reducing the testing costs. Solar cell modeling, based on numerical simulation techniques and advanced models for representing the physical properties of the devices, is a powerful tool to investigate the physical mechanisms that limit the cell conversion efficiency. While numerical simulation has been extensively used by the electronics industry since the early days of computer modeling, only recently it has become widely used in the PV industry [42].

In particular, prior to last decade, the first simulation works in the PV context relied on analytical approaches, partially supported by the aid of computer programs, and, consequently, they were mainly focused on the modeling of one-dimensional $1D$ devices due to the low requirement of computational resources, and on its very simple and intuitive user interface. Nonetheless, its predictive capability is limited by a few assumptions. Among these limitations, the most important are the adoption of Boltzmann statistics, that is not suitable to adequately model some performance-limiting highly-doped regions of the solar

cell, and the restriction to the mono-dimensional analysis, thus preventing an accurate investigation of innovative cell architectures [43]. In fact, during the last years, the growing interest for advanced solar cell architectures, featuring inherently two-dimensional $2D$ or even three-dimensional $3D$ geometries, and the requirement for a more accurate analysis of cell losses have driven to the adoption in the PV research community of multi-dimensional and general-purpose TCAD (Technology Computer-Aided Design) device simulators, able to solve numerically the fully coupled set of semiconductor differential equations within the drift-diffusion approximation, accounting also for the Fermi-Dirac statistics.

Nowadays, one of the most commonly adopted commercial TCAD program in the PV community is *Sentaurus by Synopsys*. However, in order to achieve sufficiently high prediction capabilities, several physical models and parameters of these simulators, which are usually tailored to CMOS devices, must be accurately calibrated for the specific requirements of solar cells [43, 44]. In addition to the electrical simulation, the simulation of PV devices under illumination requires an accurate modeling of light propagation and absorption inside the solar cells. To this purpose, several approaches can be adopted to calculate the optical generation rate inside the device, depending on the specific requirements about accuracy and computational effort. Among the most commonly used optical solvers in PV simulations, it is worth mentioning the Transfer Matrix Method (TMM), the Ray-Tracing (RT) method or the Finite-Difference Time-Domain (FDTD) method [43]. Likewise, a mixed-mode simulation approach, based on the combination of numerical device simulations and circuit simulations, can be successfully adopted for the modeling of entire large-area solar cells, thus accounting also for their full metallization geometry and their edges [42].

The aim of this Ph.D. thesis is to provide a contribution to the numerical simulation and modeling of *c*-Si solar cells by using a state-of-the-art *TCAD-based computer program* [45]. In order to achieve realistic predictions on silicon solar cell performance, an ad-hoc refinement of the physical models and parameters implemented in the TCAD simulator for specific PV requirements. Moreover, the thesis is written as a collection of the main concepts, previous investigations and the research work contributions related to the study of the crystalline silicon back contact-back junction (BC-BJ) solar cells. In the following, the detail of the contents of this thesis is summarized. A general overview of the current situation of climate change and a way to face the global energy demand by adopting green energy supplies is given in *Chapter 1*. A brief review of photovoltaic (PV) developments and a short motivation for the work are also included. *Chapter 2* is meant to provide the reader the theoretical background necessary to follow the discussion of the next chapters. The chapter contains the basics of solar cell operation, semiconductor model equations, recombination mechanisms and the effective lifetime.

A concise review of different passivation materials used for *c*-Si solar cells is presented. The last section of the chapter discusses the advanced solar cell concepts and introduce the

reader to the understanding of the electro-optical output parameters and the related losses of solar cells. Then, *chapter 3* furnishes the general state-of-the-art properties related to *c*-Si solar cells were described focusing on their implementation in numerical simulations as the basic methodology used in the remaining chapters. After introducing the most important parameters for characterizing solar cells, in *chapter 4* is described and analyzed the impact of the point-contact and linear-contact schemes in the back contact-back junction (BC-BJ) solar cells. The thesis concludes in *chapter 5* with a discussion on the point-contact (PC) solar cell performance with the adoption of a selective emitter design.

Chapter 2

Device physics of solar cells

Solar PV cells are quite simple devices that convert sunlight into voltage or electric current by exploiting the capabilities of semi-conducting materials (e.g., *c*-Si) to absorb light and to deliver a portion of energy to carriers of electrical current. The second chapter presents a concise review of the basic physical principles that characterize the method of function of solar cell devices. Initially, we will describe the architecture of a conventional solar cell followed by the explanation of the main process-related to the PV effect. Secondly, we will study the concepts of generation and recombination mechanisms, movement, and collection of charge carriers by using p-n junction. Also a review of the set of the basic equations that describe the ideal properties of semiconductor devices in the drift-diffusion approximation is presented. Subsequently, the simple 1D diode model is first discussed in order to analytically derive the ideal solar cell output dark and illuminated I-V characteristics. Finally, the theoretical efficiency limits and the main loss mechanisms that affect the performance of silicon solar cells are explained.

2.1 Conventional solar cells

A conventional solar cell structure is simply based on a semiconductor p-n junction diode that operates under solar illumination as sketched in Fig. 2.1. When sunlight strikes the surface of a semiconductor, a certain portion of photons is transmitted and, then, absorbed into the semiconductor material, thus giving rise to photogenerated electron-hole pairs, while the remainder is reflected from the surface. Some of these photogenerated charge carriers are separated by the internal built-in electric field of the p-n junction before they recombine and, then, they are collected at the cell terminals, thus contributing to the cell output current in the external circuit [28, 46]. On the other hand, one of the major disadvantages founded in this type of architecture is the shading losses effect caused by the presence of metal (front contacts) on the top surface of the solar cell which prevents light from entering the solar cell. The shading losses are determined by the transparency of the top surface, which, for a planar top surface, is defined as the fraction of the top surface covered by metal. The transparency is determined by the width of the metal lines on the surface and

on the spacing of the metal lines. An important practical limitation is the minimum line-width associated with a particular metallization technology. For identical transparencies, a narrow line-width technology can have closer finger spacing, thus reducing the emitter resistance losses (see Fig. 2.2) [47–49].

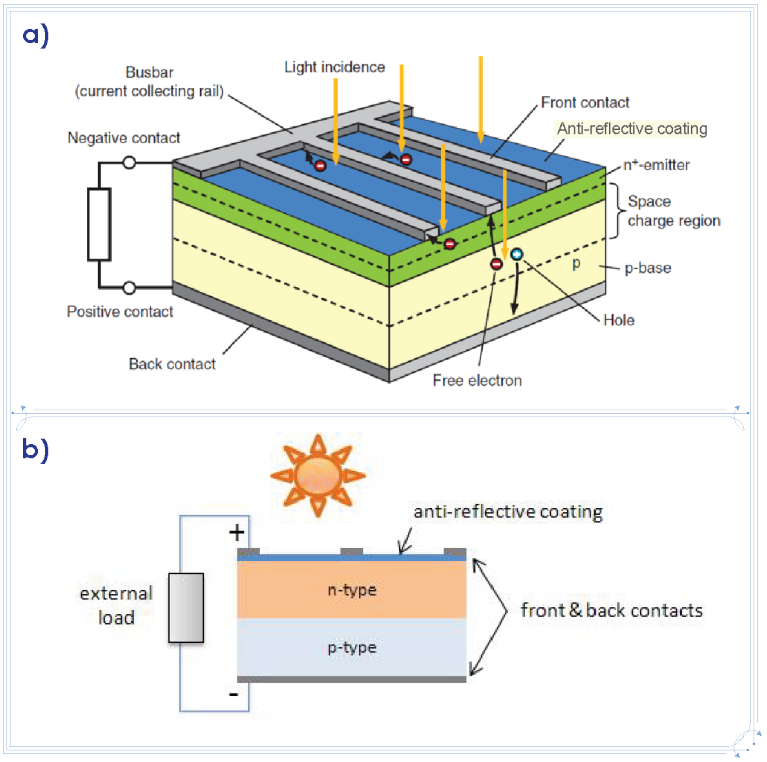

FIGURE 2.1: a) Three-dimensional (3D) view of a conventional solar cell featuring front and back contacts. b) Two-dimensional (2D) cross-section of a conventional solar cell. Taken from [7, 50].

In table 2.1 there is a summary of some of the latest published manufacturing data of *c*-Si solar cells and their certified efficiency records.

2.2 Solar cell operating principle

The working principle of a silicon solar cell is based on the well-known photovoltaic effect discovered by the French physicist Alexander Becquerel in 1839 [60]. As described in section 1.4 this effect generates an electric field at the junction of two materials in response to electromagnetic radiation (photons). It is worth noting that the PV effect is closely related to the photoelectric effect which was explained by Albert Einstein in 1905. Basically, he

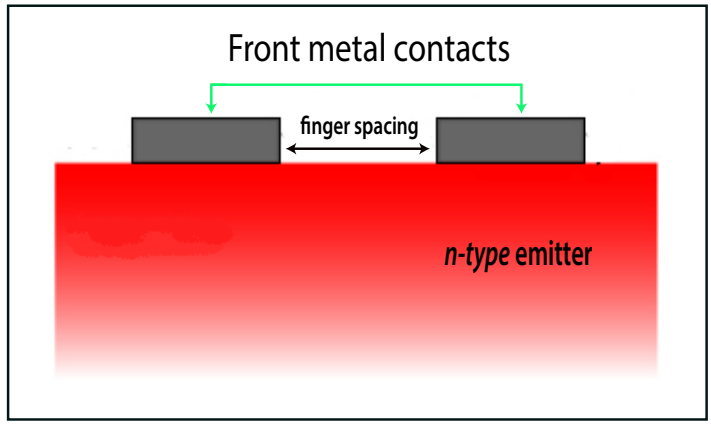

FIGURE 2.2: Sketch of a conventional solar cell featuring the top surface contacting scheme.

Device	Area [cm^2]	V_{OC} [mV]	J_{SC} [mA/cm^2]	FF[%]	η [%]	Test Center (Date)	Reference
Kaneka IBC HIT	180.43 (da)	744	42.3	83.8	26.3	FhG-ISE (7/16)	[37]
Panasonic IBC HIT	143.7 (da)	740	41.8	82.7	25.6	AIST (2/14)	[34]
SunPower IBC	153.5 (ta)	737	41.3	82.7	25.2	Fraunhofer ISE (10/15)	[51]
Kaneka SHJ	151.9 (ap)	738	40.8	83.5	25.1	Fraunhofer ISE (9/15)	[52]
Fraunhofer ISE TOPCon	4.0 (da)	718	42.1	83.2	25.1	Fraunhofer ISE (8/15)	[53, 54]
UNSW PERL (*p*-type)	4.0 (da)	706	42.7	82.8	25.0	Sandia(3/99)	[31, 55]
Panasonic HIT	101.8 (ta)	750	39.5	83.2	24.7	AIST (12/12)	[56]
EPFL MoOx SHJ	3.9 (ap)	725	38.6	80.4	22.5	Fraunhofer ISE (2015)	[57]
IMEC PERT (*n*-type)	238.9 (ta)	695	40.2	80.5	22.5	Fraunhofer ISE (2015)	[58, 59]
Trina solar mono-Si PERC (*p*-type)	243.7	680	40.5	80.3	22.1	Fraunhofer ISE (2015)	[51]

TABLE 2.1: Performance parameters of certified *c*-Si solar cells. (*da: Designated area, *ta: Total area, *ap: Aperture area)

assumed that photons are quantum energy which are present in light, and this energy is given by the following expression,

$$E = h \cdot v \tag{2.1}$$

where h is Planck's constant and v is the frequency of the light. This scientific explanation granted Einstein the Nobel Prize in Physics in 1921 [61]. Accordingly, the photovoltaic effect takes places in a solar cell, a structure based on two types of semiconductor materials that are joined together to create a p-n junction diode that operates under solar illumination (see Fig. 2.3).

Essentially, the PV effect is described by three basic process:

1. ***Generation of charge carriers (electron-hole pair) due to the absorption of light***. When sunlight hits the semiconductor surface, a portion of photons is transmitted and, then, absorbed into the material producing photo-generated electron-hole pair; while the rest is

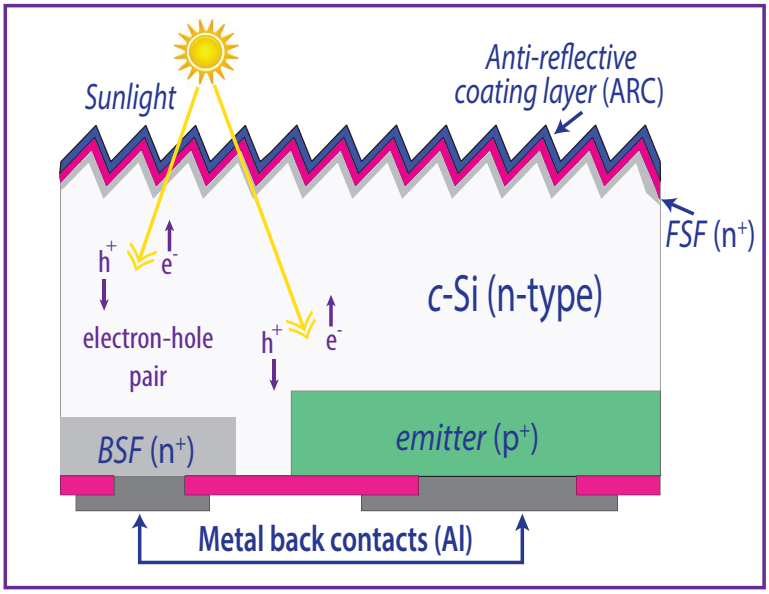

FIGURE 2.3: Schematic of a simple single-junction back contact solar cell structure, where the photogeneration of electron-hole pairs is exhibited. Re-designed from [62].

reflected.

2. ***Separation of the photo-generated charge carriers in the junction***. The electron-hole pair is separated by the internal built-in electric field of the p-n junction before they recombine.

3. ***Collection of the photo-generated charge carriers at the terminals of the junction***. The charge carriers are extracted from the solar cell with electrical contacts, thus contributing to the output current in the external circuit. Finally, the chemical energy of the charge carriers is converted to electric energy. At this point, as electrons have passed through the circuit, they will recombine with holes at a metal absorber interface, as sketched in Fig. 2.4 [28].

2.3 Semiconductor model equations

Once the electron-hole pairs are generated due to the light absorption process, they move around inside the crystal lattice and before recombining they should be collected in order to extract power from the PV cell. The way these electrical currents are generated is due to the transport of the electron-hole charges. Therefore, the well known Drift-Diffusion (D-D) model transport is the appropriated mechanism to describe the operation of charge carriers in the substrate under the influence of light and/or electric field, thus leading to a variation from the thermal equilibrium conditions. Basically, the D-D approximation consists in the

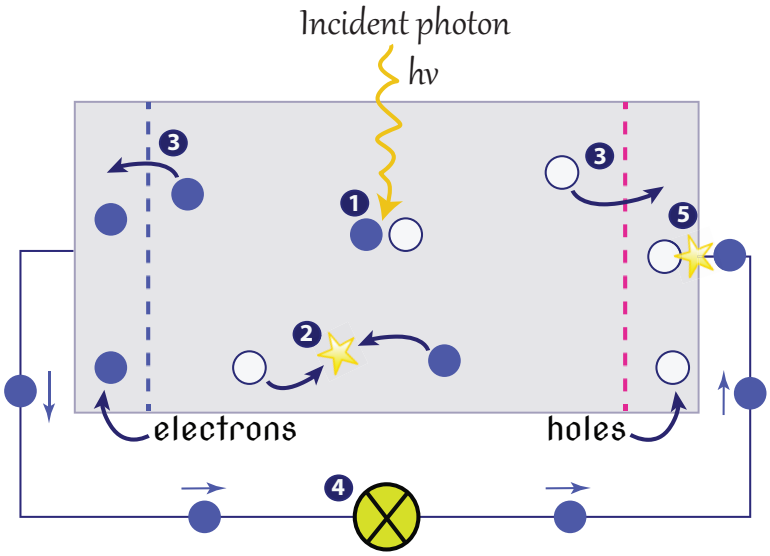

FIGURE 2.4: Schematic of a very simple solar cell model. ① Absorption of a photon leads to the generation of an electron-hole pair. ② Normally, the electrons and holes will recombine. ③ Electrons and holes can be separated by the n-type and p-type materials. ④ The separated electrons can be used to drive an electric circuit. ⑤ After the electrons have passed through the circuit, they will recombine with holes. Taken from [28].

solution of a set of five basic equations which derive the ideal properties of semiconductor devices including Si solar cells.

2.3.1 Poisson equation

Poisson equation describes the electrostatics by relating the divergence of the static electric field ξ to the charge density ρ:

$$\nabla \cdot \xi = -\nabla^2 \varphi = \frac{\rho}{\varepsilon} \tag{2.2}$$

where φ is the electrostatic potential and ε is the material permittivity. The charge density in a semiconductor device is given by,

$$\rho = q\left(p - n + N_D^+ - N_A^-\right) \tag{2.3}$$

where n and p are the electron and hole densities, and N_D^+ and N_A^- are the densities of ionized donors and acceptors, respectively.

2.3.2 Drift-Diffusion transport model equations

It is widely known that the electrical current flow in a semiconductor device is generated by the transport of electrons and holes. This is possible through the two basic drift-diffusion (D-D) transport processes. First of all, drift mechanism takes place when applying an electric field ξ across the semiconductor, whereas diffusion transport process is driven by a concentration gradient. Accordingly, the total current densities of electrons and holes denoted by, J_n and J_p are defined as,

$$J_n = q\mu_n n\xi + qD_n\nabla n \tag{2.4}$$

$$J_p = q\mu_p p\xi - qD_p\nabla p \tag{2.5}$$

where μ_n and μ_p are the electron and hole mobilities, and D_n and D_p are the electron and hole diffusion coefficients, respectively. The first terms on the right side of equation (2.4) and equation (2.5) represent the drift currents, whereas the second terms denote diffusion currents approximation. The mobility and diffusion coefficients are related through the Einstein relationship, as follows,

$$D_n = \mu_n \frac{kT}{q} \quad \text{and} \quad D_p = \mu_p \frac{kT}{q} \tag{2.6}$$

For the case of solar cell devices, the simulator estimates charge distribution and transport mechanisms according to the well known Drift Diffusion (D-D) Model.

2.3.3 Continuity equations

In order to define the complete set of semiconductor equations, two more expressions are required. These last equations associate the divergence of the current densities to the generation and recombination rates of the related charge carriers. Besides, they take into account the law of conservation of charges. Under steady-state conditions, the electron and hole continuity equations can be defined as,

$$\frac{1}{q}\nabla \cdot J_n = R_n - G_n \tag{2.7}$$

$$\frac{1}{q}\nabla \cdot J_p = -(R_p - G_p) \tag{2.8}$$

where G represents the optical generation rate of electron-hole pairs and, R_n and R_p are the recombination rates for electrons and holes respectively. For a uniformly doped semiconductor; band-gap, electric permittivity, mobility and diffusion coefficients are independent of position. Therefore, the equations (2.2), (2.4), (2.5), (2.7) and (2.8) represent the base

for obtaining the reduced version of semiconductor equations. Under one dimensional assumption (i.e. variations in other two spatial dimensions are neglected) the equations turn into,

$$\frac{d\xi}{dx} = \frac{q}{\varepsilon}(p - n + N_D^+ - N_A^-) \tag{2.9}$$

$$J_n = q\mu_n n\xi + qD_n \frac{dn}{dx} \tag{2.10}$$

$$J_p = q\mu_p p\xi - qD_p \frac{dp}{dx} \tag{2.11}$$

$$\frac{1}{q}\frac{dJ_n}{dx} = R_n - G_n \tag{2.12}$$

$$\frac{1}{q}\frac{dJ_p}{dx} = -(R_p - G_p) \tag{2.13}$$

By including the expressions of the current densities described in equations (2.10) and (2.11) into the continuity equations (2.12) and (2.13), a new set of transport equations can be obtained,

$$D_n \frac{d^2n}{dx^2} + \mu_n \xi \frac{dn}{dx} + n\mu_n \frac{d\xi}{dx} - R_n + G_n = 0 \tag{2.14}$$

$$D_p \frac{d^2p}{dx^2} + \mu_p \xi \frac{dp}{dx} - p\mu_p \frac{d\xi}{dx} - R_p + G_p = 0 \tag{2.15}$$

These last two equations are coupled through the electric field ξ defined in the Poisson equation (see equation (2.9)) and they form a set of non-linear differential equations which do not have an analytical solution. Nevertheless, these equations can be solved analytically or numerically by making some assumptions, as described in section 2.4 related to the 1D diode model.

2.4 1D p-n junction diode model

An ideal PV cell illuminated *I-V* characteristics and output dark can be easily solved, from the set of equations already presented in the previous section 2.3. To achieve this, it is mandatory to adopt a simple 1D *p-n* junction diode model for a silicon solar cell featuring

a constant doping in the *n*- and *p*-type regions, and a blunt doping step transition, as well as additional simplified assumptions [63].

2.4.1 Electrostatics of the p-n junction

As already explained a conventional solar cell is simply formed by the well-known *p*-*n* junction. It consists of a simple union of two oppositely doped silicon blocks that allows the operation of the device, aggregating all carrier transport (e.g., drift and diffusion effects) as illustrated in Fig. 2.5. The *n*-type block has a large number of free electrons negatively charged. Meanwhile, *p*-type block has also a big amount of free holes positively charged. Both charged carriers can move freely through the semiconductor material.

When two pieces of *n*-type and *p*-type doped semiconductors are brought into contact, electrons diffuse from the region of high concentration (*n*-type side) to the region of low concentration (*p*-type side), due to the concentration gradient between the two types of material. Similarly, holes diffuse from *p*-type side to *n*-type side. As a consequence, the electrons diffusion current from the *n*-doped to the *p*-doped region creates a charge imbalance in the *n*-type side, leading to a positively charged region in that side (see Fig. 2.6). Likewise, the holes diffusion causes a negative charge in the *p*-type side. This leads to the creation of an electric field that opposes the diffusion transport, thus resulting in an equilibrium situation.

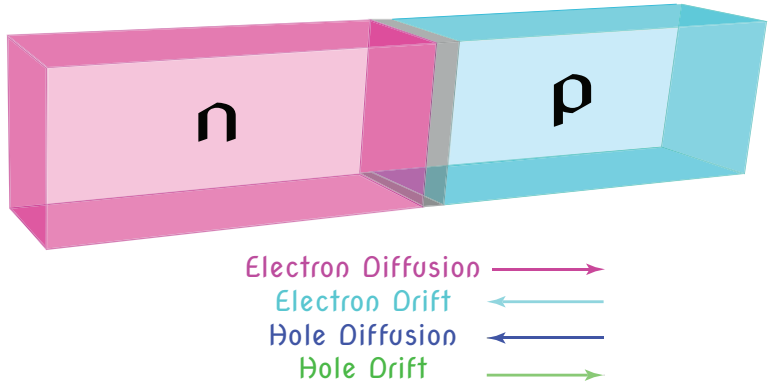

FIGURE 2.5: Sketch of a 3D p-n junction semiconductor diode. Re-designed from [64].

The transition region between the n-type and p-type of the semiconductor material, where the electric field E is present, is known as the *depletion region* (denoted by W), since it is depleted of free carriers (i.e. electrons and holes swept by the E electric field) [65, 66].

With regards to the energy band diagrams, the main concepts are illustrated in Fig. 2.7a) where a structure of an *n*-type interdigitated back contact (IBC) crystalline silicon solar cell is sketched and features two phosphorus diffusions (n^+) to create the top region knows as

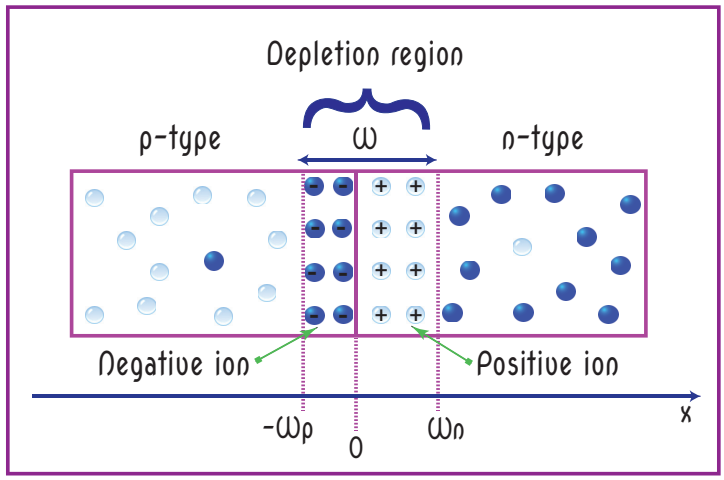

FIGURE 2.6: Simple solar cell schematic showing a 1D p-n junction. The junction is in $x = 0$, W is the width of the depletion region, whereas $-W_p$ and W_n represent the edges of the depletion region [67].

front surface field (FSF) and the bottom region called *back surface field* (BSF). The junction is at the back by the injection of Boron in the emitter region. Specific details such as lifetimes, concentrations, and thickness, will be presented in detail through the development of this work of thesis. On the other hand, Figure 2.7b) the p-n junction is in equilibrium. It shows a constant Fermi level E_F, thus causing the band bending of the conduction energy band E_C and the valence band E_V. In Fig. 2.7c) the Fermi energy level splits into two quasi-Fermi energy levels when the solar cell is working in a *maximum power point*. This is a consequence of the excess concentration of carriers generated by the one-sun illumination. A small gradient of the quasi-Fermi energy levels drives electrons to fall (as balls) to the left, whereas holes rise up (as bubbles) to the right side. This directional flow of electron-hole carriers is due to the fact that, electron density is several orders of magnitude higher than hole density on the left (n^+ region), and the opposite happens on the right side (p^+ region), as shown in Fig. 2.7d).

In terms of energy bands, the Fermi levels E_f of two separated *p*-and *n*- doped regions are different. Instead, the *p-n* junction in equilibrium shows a constant Fermi level, thus causing the band bending of the conduction energy band E_C and the valence energy band E_V (see Fig. 2.7b)). From Fig. 2.7b), the electrostatic potential difference across the junction, known as the built-in potential φ_0, can be expressed as,

$$q\varphi_0 = E_g - E_1 - E_2 \tag{2.16}$$

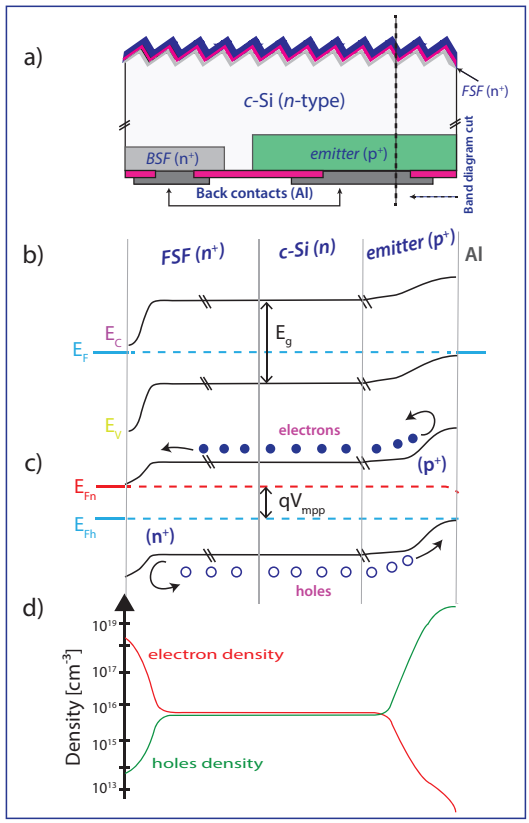

FIGURE 2.7: Energy band diagrams of a) simulated inter-digitated back contact (IBC) n-type ($5\,\Omega\,\mathrm{cm}$) c-Si solar cell featuring main regions such as bulk, FSF, BSF, and emitter. b) p-n junction in equilibrium. c) maximum power point operation. d) electron-hole density or concentration in the FSF, bulk and emitter regions, respectively.

where $E_g = E_C - E_V$ is the energy band-gap between the conduction and valence band edges. E_1 and E_2 can be derived from the Boltzmann expressions of the free carrier concentrations for non-degenerate doped semiconductors at thermal equilibrium, assuming that the dopants are fully ionized [68]:

$$n_0 = N_D = N_C \exp\left(-\frac{E_C - E_F}{kT}\right) \tag{2.17}$$

$$p_0 = N_A = N_V exp\left(-\frac{E_F - E_V}{kT}\right) \tag{2.18}$$

where N_C and N_V are the effective densities of states of the conduction and valence bands, respectively. Consequently:

$$E_1 = E_F - E_V = kT \ln\left(\frac{N_V}{N_A}\right), E_2 = E_C - E_F = kT \ln\left(\frac{N_C}{N_D}\right) \tag{2.19}$$

At thermal equilibrium conditions, the semiconductor mass-action law is still valid, and, by using equations (2.17) and (2.18) it can be written as,

$$n_i^2 = n_0 p_0 = N_C N_V \exp\left(-\frac{E_g}{kT}\right) \tag{2.20}$$

Therefore, by including equations (2.19) and (2.20) in equation (2.16), it is possible to express the built-in potential as,

$$\phi_0 = \frac{kT}{q} \ln\left(\frac{N_A N_D}{n_i^2}\right) \tag{2.21}$$

The electrostatics of the *p-n* junction is defined by Poisson equation (see equation (2.2)). Since the space-charge region across the junction (i.e., for $-W_p$ < x < W_n in Fig. 2.6) is almost completely depleted of mobile charge carriers (i.e., *p* and *n* are negligible compared to the donor and acceptor densities), a simple model for this region, based on the *depletion approximation*, can be considered by assuming rectangular charge density distributions in the device, as shown in Fig. 2.8a. In this way, the device can be divided into two types of regions: the *quasi-neutral regions* (QNRs) where the charge density is assumed to be zero throughout (i.e., for x $\leq$-W_p and x $\geq W_n$ in Fig. 2.6) and the *depletion region* where the carrier densities are assumed to be negligible and, therefore, the only contribution to the charge density comes from the ionized dopants. Accordingly, Poisson equation in the depletion region is given by,

$$\frac{\mathrm{d}\xi}{\mathrm{d}x} = -\frac{\mathrm{d}^2\phi}{\mathrm{d}x^2} = -\frac{q}{\epsilon} N_A \quad \text{if} \quad -W_p < x < 0 \tag{2.22}$$

$$\frac{\mathrm{d}\xi}{\mathrm{d}x} = -\frac{\mathrm{d}^2\phi}{\mathrm{d}x^2} = \frac{q}{\epsilon} N_D \quad \text{if} \quad 0 < x < W_n \tag{2.23}$$

On the contrary, in the QNRs, Poisson equation becomes,

$$\frac{\mathrm{d}\xi}{\mathrm{d}x} = -\frac{\mathrm{d}^2\phi}{\mathrm{d}x^2} = 0 \quad if \ -W_p \leq x \ and \ x \geq W_n \tag{2.24}$$

Therefore, the electric field in the depletion region can be found by integrating Poisson equation, expressed in equation (2.22) and equation (2.23), from x = 0 to the edges of this region, thus obtaining,

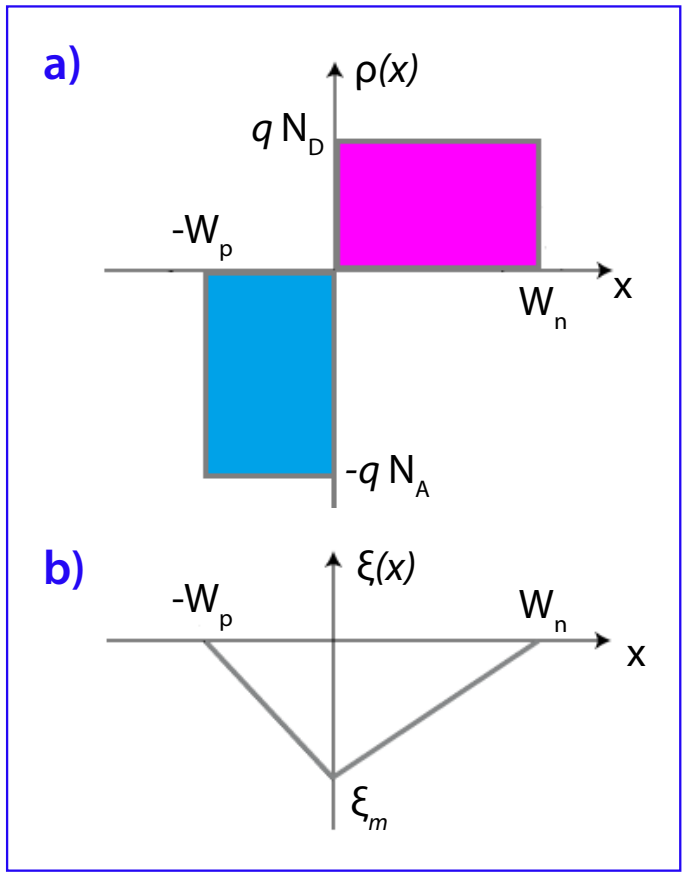

FIGURE 2.8: a) Charge density distributions in the p-n junction under the depletion approximation. b) Corresponding electrical field profile.

$$\xi(x) = -\frac{qN_A}{\epsilon}(x + W_p) \qquad if \ -W_p < x < 0 \tag{2.25}$$

$$\xi(x) = \frac{qN_D}{\epsilon}(x - W_n) \qquad if \ 0 < x < W_n \tag{2.26}$$

$$\xi_m = \frac{qN_D W_n}{\epsilon} = \frac{qN_A W_p}{\epsilon} \qquad in \ \ x = 0 \tag{2.27}$$

where ξ_m is the maximum intensity of the electric field in x=0 (Fig. 2.8b)). This figure

also shows the linear dependence of the electrical field on the position in the depletion region, while the electric filed vanishes in the QNRs, according to the assumed charge density distributions. By integrating equations (2.25) and (2.26) along x, the electrostatic potential in the depletion region can be found as,

$$\phi_p(x) = \frac{qN_A}{2\epsilon}x(2W_p + x) \qquad if \ -W_p < x < 0 \tag{2.28}$$

$$\phi_n(x) = \frac{qN_D}{2\epsilon}x(2W_n - x) \qquad if \ 0 < x < W_n \tag{2.29}$$

Consequently, the potential difference at the depletion region edges is given by,

$$\phi_0 = \phi_n(W_n) - \phi_p(-W_p) = \frac{q}{2\epsilon}(N_D W_n^2 + N_A W_p^2) = \frac{1}{2}\xi_m W \tag{2.30}$$

where $W = W_n + W_p$ is the width of the depletion region (see Fig. 2.6). Moreover, the electrical neutrality of the device can be expressed as,

$$W_p N_A = W_n N_D \tag{2.31}$$

By combining equations (2.30) and (2.31), the width of the depletion region can be defined as,

$$W = \sqrt{\frac{2\epsilon}{q}\left(\frac{N_A + N_D}{N_A N_D}\right)\phi_0} \tag{2.32}$$

An external applied bias voltage V_a disturbs the equilibrium conditions, shifting the potential barrier and, consequently, the potential difference across the *p-n* junction, that becomes $(\phi_0 - V_a)$. Accordingly, equation (2.32) changes as,

$$W = \sqrt{\frac{2\epsilon}{q}\left(\frac{N_A + N_D}{N_A N_D}\right)(\phi_0 - V_a)} \tag{2.33}$$

2.4.2 Ideal dark I-V characteristics

In order to derive the ideal *I-V* characteristics of a *p-n* junction, the minority-carrier densities at the edges of the depletion region as a function of bias have to be found. At thermal equilibrium, conditions (zero bias), their values are already known [68].

$$p_{n0} = p_{p0}\exp\left(-\frac{q\phi_0}{kT}\right) \approx \frac{n_i^2}{N_D} \tag{2.34}$$

$$n_{p0} = n_{n0} \exp\left(-\frac{q\phi_0}{kT}\right) \approx \frac{n_i^2}{N_A} \tag{2.35}$$

where p_{p0} and n_{n0} are the majority-carrier concentrations in the quasi-neutral regions, respectively. Under low-injection conditions, i.e. the minority-carrier densities are negligible as compared to the majority-carrier ones on both sides ($n_n >> p_n \; and \; p_p >> n_p$), the majority-carrier concentrations can be expressed as,

$$n_n\ (W_n) = n_{n0} = N_D, \quad p_p\ (-W_p) = p_{p0} = N_A \tag{2.36}$$

Under this assumption, the expressions for the minority-carrier concentrations at the edges of the depletion region (see Fig. 2.9) are given by [68],

$$p_n(W_n) = p_{n0} \exp\left(\frac{qV_a}{kT}\right) = \frac{n_i^2}{N_D} \exp\left(\frac{qV_a}{kT}\right) \tag{2.37}$$

$$n_p\ (-W_p) = n_{p0} \exp\left(\frac{qV_a}{kT}\right) = \frac{n_i^2}{N_A} \exp\left(\frac{qV_a}{kT}\right) \tag{2.38}$$

Therefore, the concentrations of the minority carriers at the edges of the depletion region increase exponentially with the applied bias voltage. Moreover, it is possible to demonstrate that, if a uniformly doped region of semiconductor material is quasi-neutral (i.e., the charge density is approximately zero) and minority-carrier flows are not irrelevant, the minority-carrier transport in this quasi-neutral region is predominantly diffusive. Thus,

$$J_n = qD_n \frac{\partial n}{\partial x} \quad \text{(in p-type quasi-neutral region)} \tag{2.39}$$

$$J_p = -qD_p \frac{\partial p}{\partial x} \quad \text{(in n-type quasi-neutral region)} \tag{2.40}$$

Basically, it happens that the small number of minority carriers compared to majority carriers shields them from the effect of an electric field [68].

The calculation of the quantitative expression for the ideal dark *I-V* characteristics of the *p-n* junction requires the solution of the transport equations for electrons and holes (see equations (2.14) and (2.15)). As already discussed, both these two equations contain

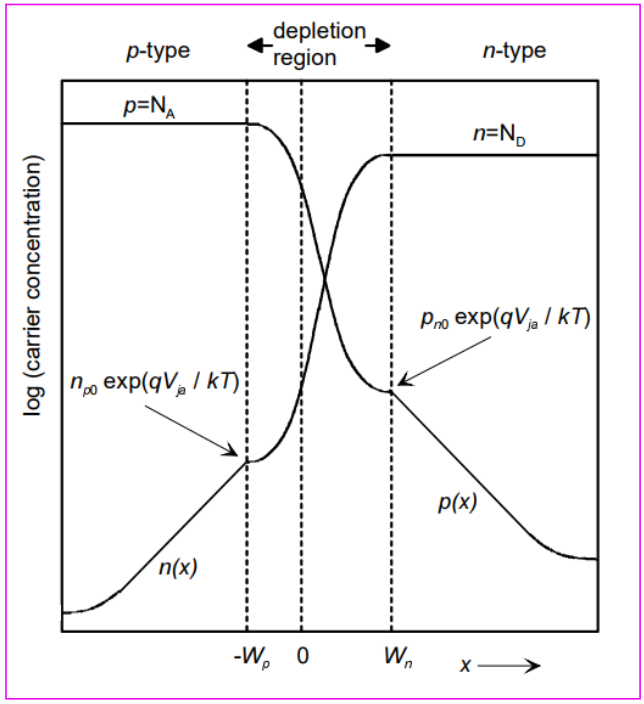

FIGURE 2.9: Electron and hole carrier concentrations across the dark forward-biased p-n junction. Taken from [69].

the electrical field ξ, thus forming a coupled set of differential equations, where the unknowns are the carrier concentrations n and p, and the electrical field. Therefore, if the spatial dependence of the electric field and of the carrier concentrations is known, the current densities can be easily calculated from equations (2.10) and (2.11). Through the approximations discussed in section 2.4.1, it has been found that the electric field vanishes in the QNRs of the *p-n* junction and, hence, the transport equations (2.14) and (2.15) decouple in these regions. As a consequence, the carrier transport is purely diffusive and, therefore, the minority-carrier concentrations can be calculated separately for both quasi-neutral regions from the following decoupled linear differential equations,

$$D_n \frac{\mathrm{d}^2 n_p}{\mathrm{d}x^2} - R_n + G_n = 0 \quad \text{(in p-type quasi-neutral region)} \tag{2.41}$$

$$D_p \frac{\mathrm{d}^2 p_n}{\mathrm{d}x^2} - R_p + G_p = 0 \quad \text{(in n-type quasi-neutral region)} \tag{2.42}$$

Furthermore, under low-injection conditions, the perturbation of the majority-carrier

concentrations due to generation and recombination mechanisms can be neglected [69]. Consequently, the recombination rate of minority carriers on both sides of the *p-n*junction is proportional to the excess minority-carrier concentrations, as given by,

$$R_n = \frac{n_p - n_{p0}}{\tau_n} \quad \text{(in p-type quasi-neutral region)} \tag{2.43}$$

$$R_p = \frac{p_n - p_{n0}}{\tau_p} \quad \text{(in n-type quasi-neutral region)} \tag{2.44}$$

where τ_n and τ_p are the minority-carrier lifetimes of electrons and holes, respectively, assumed to be independent of carrier concentrations. Therefore, transport equations become,

$$D_n \frac{\mathrm{d}^2 n_p}{\mathrm{d}x^2} - \frac{n_p - n_{p0}}{\tau_n} + G_n = 0 \quad \text{(in p-type quasi-neutral region)} \tag{2.45}$$

$$D_p \frac{\mathrm{d}^2 p_n}{\mathrm{d}x^2} - \frac{p_n - p_{n0}}{\tau_p} + G_p = 0 \quad \text{(in n-type quasi-neutral region)} \tag{2.46}$$

In dark conditions, G = 0, then, equations (2.43) and (2.44) in the QNRs reduce to homogeneous differential equations,

$$\frac{\mathrm{d}^2 \Delta n}{\mathrm{d}x^2} - \frac{\Delta n}{L_n^2} = 0 \qquad (x \leq -W_p) \tag{2.47}$$

$$\frac{\mathrm{d}^2 \Delta p}{\mathrm{d}x^2} - \frac{\Delta p}{L_p^2} = 0 \qquad (x \geq W_n) \tag{2.48}$$

$$L_n = \sqrt{D_n \tau_n} \qquad L_p = \sqrt{D_p \tau_p} \tag{2.49}$$

where L_n and L_p are the diffusion length of electrons in the *p*-type side and holes in the n-type side, respectively. For the solution of equations (2.47) and (2.48), the two following boundary conditions have to be considered:

1) at x $\rightarrow \infty$, by assuming that there are no recombination losses at the surface of both quasi-neutral regions (i.e., *n*-type and *p*-type regions are of infinite dimensions), n_p and p_n are finite, therefore,

$$\frac{\mathrm{d}n}{\mathrm{d}x}|_{x \mapsto -\infty} = 0 \qquad \frac{\mathrm{d}p}{\mathrm{d}x}|_{x \mapsto \infty} = 0 \tag{2.50}$$

2) at x = W_n and x = -W_p, the boundary conditions are given by equations (2.37) and (2.38), respectively. These boundary conditions give the following particular solutions [69],

$$n_p(x) = n_{p_0} + n_{p_0}\left[\exp\left(\frac{qV_a}{kT}\right) - 1\right]\exp\left(\frac{W_p + x}{L_n}\right) \tag{2.51}$$

$$p_n(x) = p_{n0} + p_{n0}\left[\exp\left(\frac{qV_a}{kT}\right) - 1\right]\exp\left(\frac{W_n - x}{L_p}\right) \tag{2.52}$$

From equations (2.51) and (2.52), it is possible to note that the excess carrier concentrations for electrons in the *p*-type QNR and holes in the *n*-type QNR decay exponentially from position x = -W_p and x = W_n, respectively, with the diffusion lengths as characteristic lengths (see Fig. 2.9). Once the minority-carrier density distributions are known, the minority-carrier diffusive current densities in the QNRs can be easily calculated from equations (2.39) and (2.40),

$$J_n(x) = \frac{qD_n n_{p0}}{L_n}\left[\exp\left(\frac{qV_a}{kT}\right) - 1\right]\exp\left(\frac{W_p + x}{L_n}\right) \tag{2.53}$$

$$J_p(x) = \frac{qD_p p_{n0}}{L_p}\left[\exp\left(\frac{qV_a}{kT}\right) - 1\right]\exp\left(\frac{W_n - x}{L_p}\right) \tag{2.54}$$

Instead, considering the current flows in the depletion region, the continuity equations in this region are given by:

$$\frac{1}{q}\frac{\mathrm{d}J_n}{\mathrm{d}x} = R - G = -\frac{1}{q}\frac{\mathrm{d}J_p}{\mathrm{d}x} \tag{2.55}$$

By assuming that no recombination losses occur in the depletion region, it follows that, in dark conditions (i.e., G = 0), both the current densities are essentially constant across the depletion region. Consequently, the total current density can be found from equations (2.53) and (2.54) as,

$$J_{tot} = J_n(-W_p) + J_p(W_n) = J_0\left[\exp(\frac{qV_a}{kT}) - 1\right] \tag{2.56}$$

where

$$J_0 = \frac{qD_n n_{p0}}{L_n} + \frac{qD_p p_{n0}}{L_p} = qn_i^2\left[\frac{D_n}{L_n N_A} + \frac{D_p}{L_p N_D}\right] \tag{2.57}$$

is the dark saturation current density of the p-n junction. The equation (2.56), also known as the *Shockley equation*, represents the ideal dark *I-V* characteristics of the *p-n* junction.

2.4.3 Ideal illuminated *I-V* characteristics

The ideal illuminated *I-V* characteristics are generally derived by considering, for mathematical simplicity, the case of a spatially-uniform generation rate *G* of electron-hole pairs inside the device. This assumption strongly simplifies the mathematical treatment, without altering the most important conclusions. Therefore, in illuminated conditions (i.e., $G \neq 0$), the transport equations (2.45) and (2.55) in the QNRs become inhomogeneous differential equations:

$$\frac{\mathrm{d}^2\Delta n}{\mathrm{d}x^2} - \frac{\Delta n}{L_n^2} = -\frac{G_n}{D_n} \qquad (x \leq -W_p) \tag{2.58}$$

$$\frac{\mathrm{d}^2\Delta p}{\mathrm{d}x^2} - \frac{\Delta p}{L_p^2} = -\frac{G_p}{D_p} \qquad (x \geq W_n) \tag{2.59}$$

Since the terms G_n / D_n and G_p / D_p are constant, the solutions of equations (2.58) and (2.59) can be found by applying the superposition principle, i.e., by adding particular solutions of the inhomogeneous differential equations to the general homogeneous solutions, as explained in [69]. By following this approach, the minority-carrier densities in the QNRs under illumination can be calculated as,

$$n_p(x) = n_{p0} + G_{\tau_n} + \left[n_{p0} \left(\exp\left(\frac{qV_a}{kT}\right) - 1 \right) - G_{\tau_n} \right] \exp\left(\frac{W_p + x}{L_n}\right) \tag{2.60}$$

$$p_n(x) = p_{n0} + G_{\tau_p} + \left[p_{n0} \left(\exp\left(\frac{qV_a}{kT}\right) - 1 \right) - G_{\tau_p} \right] \exp\left(\frac{W_n - x}{L_p}\right) \tag{2.61}$$

Then, the corresponding diffusive current densities become,

$$J_n(x) = \frac{qD_n n_{p0}}{L_n} \left[\exp\left(\frac{qV_a}{kT}\right) - 1 \right] \exp\left(\frac{W_p + x}{L_n}\right) - qGL_n \exp\left(\frac{W_p + x}{L_n}\right) \tag{2.62}$$

$$J_p(x) = \frac{qD_p p_{n0}}{L_p} \left[\exp\left(\frac{qV_a}{kT}\right) - 1 \right] \exp\left(\frac{W_n - x}{L_p}\right) - qGL_p \exp\left(\frac{W_n - x}{L_p}\right) \tag{2.63}$$

In the depletion region, neglecting again the recombination losses, the effect of the uniform photogeneration of electron-hole pairs gives a change in the total current density equal to *qGW* [68]. Consequently, in illuminated conditions, the total current density is given by,

$$J_{tot} = J_n(-W_p) + J_p(W_n) - qGW = J_0 \left[\exp\left(\frac{qV_a}{kT}\right) - 1\right] - J_{ph} \tag{2.64}$$

where J_{ph} is the photogenerated current, expressed as,

$$J_{ph} = qG(W + L_n + L_p) \tag{2.65}$$

The equation (2.64) represents the ideal illuminated *I-V* characteristics of a solar cell (see Fig. 2.10). It is worth noting in Fig. 2.10 that the illuminated *I-V* curve is simply the dark curve shifted down from the first quadrant to the fourth quadrant by the photogenerated current density J_{ph}.

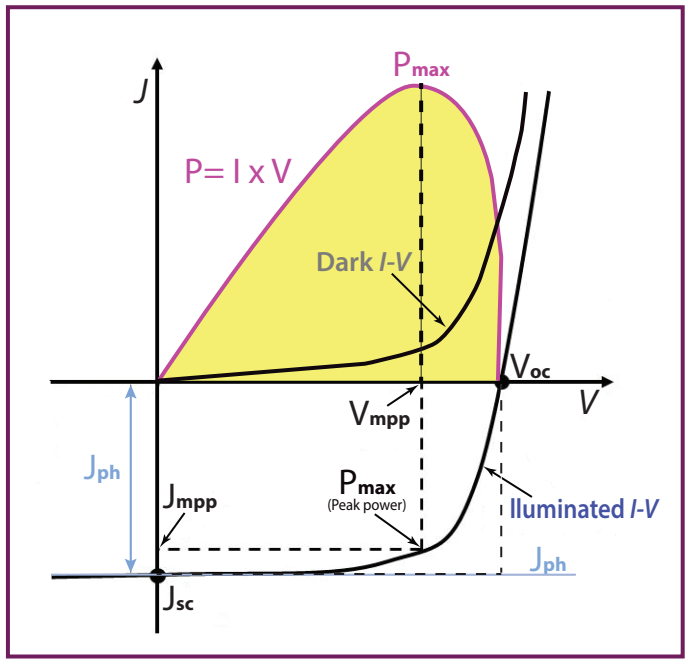

FIGURE 2.10: Typical illuminated and dark I-V curves of a solar cell. Note that P_{max} is the point where the output power is maximum. J_{sc} is the maximum current and V_{oc} is the maximum voltage. Redesigned from [28].

2.4.4 Electrical output parameters

The electrical characteristics of solar cells can be described by the equivalent circuit of a single- or double-diode model, as the most commonly used ones. Both models provide simple and fast methods to extract the electrical parameters as well as the *I-V* and *P-V*

curves, with minimum errors. However, the two diode circuit is a complex modified form of the single diode model which considers the effect of the recombination process by introducing a second diode in parallel. Therefore, typically the illuminated *I-V* characteristics of a real solar cell are analytically described through the *two-diode equivalent circuit model*, given by,

$$J(V) = J_{01}\left[exp\left(\frac{q(V-J(V)R_s)}{n_1 kT}\right)-1\right] + J_{02}\left[exp\left(\frac{q(V-J(V)R_s)}{n_2 kT}\right)-1\right] + \frac{V-J(V)R_s}{R_{sh}} - J_{ph} \tag{2.66}$$

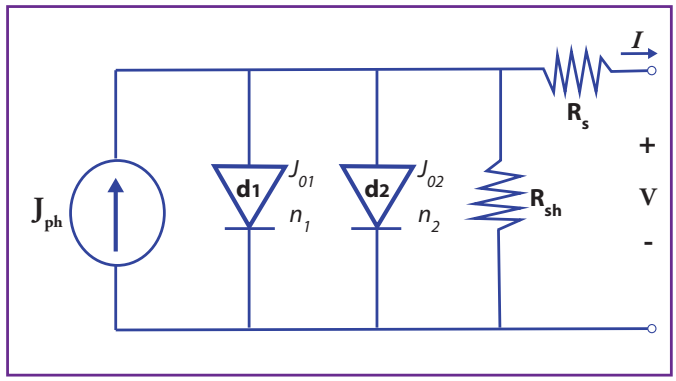

FIGURE 2.11: The equivalent circuit of a solar cell described by means of the double-diode model (according to equation (2.66)). The circuit includes the parasitic series (R_s) and shunt (R_{sh}) resistances, respectively.

Fig. 2.11 shows the equivalent circuit of equation (2.66), composed by two diodes in parallel with different ideality factors n_1 and n_2, and different saturation current densities J_{01} and J_{02} representing the recombination current terms, the photocurrent generator J_{ph}, and the series and shunt resistances R_s and R_{sh}. By varying n_1, n_2, J_{01}, J_{02}, R_s and R_{sh} parameters, a wide range of experimentally measured or simulated I-V characteristics can be fitted [70]. Typically, n_1 characterizes the recombination in the quasi-neutral regions and, hence, it is close to 1, while $1.5 < n_2 < 3$ is used to represent the recombination occurring in the depletion region and other non-ideal recombination effects.

Thereby, the most important parameters commonly used to characterize solar cell performance can directly be extracted from the illuminated *I-V* characteristics of the p-n junction, depicted in Fig. 2.10. As it was mentioned before, from this diagram, it can be noticed that the illuminated I-V curve is simply the dark curve shifted down from the first quadrant to the fourth quadrant by the photogenerated current density J_{ph}.

The following electrical output parameters are typically used to characterize the performance of a solar cell:

- the *Photogenerated current density* J_{ph} under illumination, normally expressed in mA/cm^2.
- the *short-circuit current density* J_{sc} is commonly expressed in mA/cm^2. It denotes the current density at zero voltage (see Fig. 2.10); ideally (i.e., zero recombination), the J_{sc} is equal to the *Photogenerated current density* J_{ph}.
- the *open-circuit voltage* V_{oc} is typically expressed in mV. It represents the voltage at zero current, as illustrated in Fig. 2.10; by setting J_{tot} = 0 in equation (2.64), the relationship between the V_{oc} and the dark saturation current density J_0 can be found as,

$$V_{oc} = \frac{kT}{q} ln \left(\frac{J_{ph}}{J_0} + 1 \right) \tag{2.67}$$

- the *maximum power point* P_{mpp} is normally expressed in mW/cm^2 and can be described by the following expression,

$$P_{mpp} = J_{mpp} V_{mpp} \tag{2.68}$$

  where J_{mpp} and V_{mpp} represent the current density and voltage at the maximum power point, respectively.

- the *fill factor* FF, normally expressed as a percentage, is defined as the ratio of the maximum output power to the theoretical maximum output power, as follows,

$$FF = \frac{P_{mpp}}{J_{sc} V_{oc}} = \frac{J_{mpp} V_{mpp}}{J_{sc} V_{oc}} \tag{2.69}$$

  Graphically, the FF is a measure of the *I-V* characteristic squareness, which is defined as the ratio of the two rectangular areas shown in Fig. 2.10. Ideally, the FF is a function only of the open-circuit voltage V_{oc}. A typical empirical expression, that relates FF and V_{oc}, is given by,

$$FF = \frac{V_{oc} - \ln(V_{oc} + 0.72)}{V_{oc} + 1} \tag{2.70}$$

  where V_{oc} is the normalized open-circuit voltage, defined as $V_{oc}/(kT/q)$.

- the *power conversion efficiency* (η) is typically expressed as a percentage, and is defined as the ratio of the maximum output power to the incident solar power P_{in}, which is determined by the properties of the light spectrum incident upon the cell.

Thus, the incident solar power P_{in} is commonly equal to 1000 W/m^2 at 300 K, air mass 1.5 Global spectrum (i.e. under standard test conditions (STC) for terrestrial applications) [71]. The *Power conversion efficiency* (η) can be written as,

$$\eta = \frac{P_{mpp}}{P_{in}} = \frac{J_{mpp}V_{mpp}}{P_{in}} = \frac{J_{sc}V_{oc}FF}{P_{in}} \tag{2.71}$$

2.4.5 Optical output parameters

The electrical figures of merit like short-circuit current J_{sc}, open-circuit voltage V_{oc} and fill factor *FF*, are already described in section 2.4.4. They are not sufficient to fully characterize the performance of a solar cell. Generally, these parameters may provide partial information about processes such as the light absorption and the recombination. Thence, some optical output parameters are helpful to analyze and understand in detail, the behavior of the solar cell and the dominant loss mechanisms that contribute to the degradation of the yield of the device.

- the *reflectance* $R(\lambda)$, defined as,

$$R(\lambda) = \frac{P_R(\lambda)}{P_{in}(\lambda)} \tag{2.72}$$

  where P_R is the reflected portion of the incident solar power.

- the *transmittance* $T(\lambda)$, given by,

$$T(\lambda) = \frac{P_T(\lambda)}{P_{in}(\lambda)} \tag{2.73}$$

  where P_T is the transmitted portion of the incident solar power.

- the *absorbance* $A(\lambda)$, expressed as,

$$A(\lambda) = \frac{P_A(\lambda)}{P_{in}(\lambda)} \tag{2.74}$$

  where P_A is the absorbed portion of the incident solar power.
  It is worth noting that, for the optical conservation law, (see Fig. 2.12)

$$R(\lambda) + T(\lambda) + A(\lambda) = 1$$

- the *spectral response* $SR(\lambda)$, normally expressed in A/W, is defined as the ratio of the current generated by the solar cell under short-circuit current conditions $J_{sc}(\lambda)$ to the incident irradiance $I_{in}(\lambda)$, as a function of the wavelength λ of the radiation,

$$SR(\lambda) = \frac{J_{sc}(\lambda)}{I_{in}(\lambda)} \tag{2.75}$$

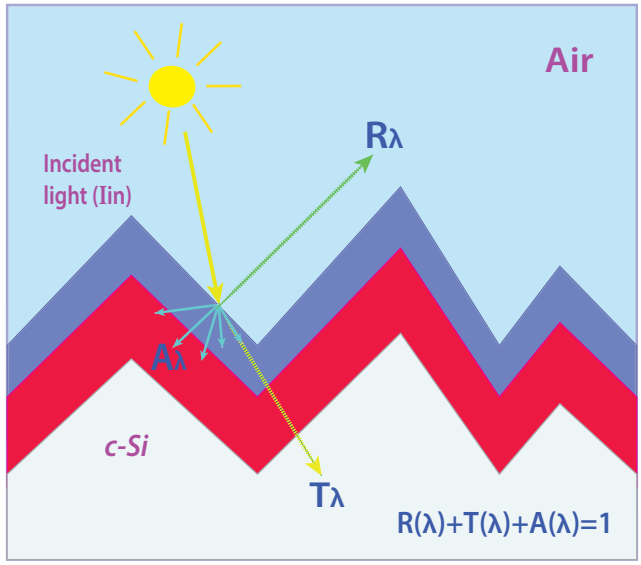

FIGURE 2.12: Schematic of the reflection R(λ), absorption A(λ), and transmission T(λ) of light in a textured *c*-Si solar cell.

- the *external quantum efficiency* $EQE(\lambda)$, represents the probability that carriers are generated and collected at the cell terminals under illumination, which is defined as the ratio of the number of carriers collected by the solar cell under short-circuit conditions to the number of incident photons of a given energy,

$$EQE(\lambda) = \frac{\eta_{sc}(\lambda)}{\eta_{in}(\lambda)} = \frac{J_{sc}(\lambda)}{J_{in}(\lambda)} \tag{2.76}$$

where $\eta_{sc}(\lambda)$ is the rate of carriers collected by the solar cell under short-circuit conditions, $\eta_{in}(\lambda)$ is the incident photon rate (i.e. the number of incident photons per unit time), $J_{sc}(\lambda)$ is the short-circuit current density, and $J_{in}(\lambda)$ is the incident photon current density, respectively, as a function of the wavelength λ of the radiation. The incident photon flux $\Phi(\lambda)$ (i.e. the number of photons per time and area unit) is given by,

$$\Phi(\lambda) = \frac{I_{in}(\lambda)}{E_{ph}(\lambda)} = \frac{I_{in}(\lambda)}{h\nu} \tag{2.77}$$

where $E_{ph}(\lambda)$ is the photon energy as a function of the wavelength λ of the radiation. The collection rate of carriers under short-circuit conditions is given by $J_{sc} \cdot A/q$, while the incident photon rate is $\Phi(\lambda) \cdot A$, where A is the area of the solar cell. Therefore, equation (2.76) can be rewritten as,

$$EQE(\lambda) = \frac{J_{sc}(\lambda)/q}{I_{in}(\lambda)/E_{ph}(\lambda)} = SR(\lambda)\frac{E_{ph}(\lambda)}{q} \tag{2.78}$$

The equation (2.78) thus relates the external quantum efficiency and the spectral response.

- the *internal quantum efficiency* $IQE(\lambda)$ is the ratio of the number of carriers which contribute to the cell output current under short-circuit conditions to the number of photons that are not reflected by the cell,

$$IQE(\lambda) = \frac{EQE(\lambda)}{1 - R(\lambda)} \tag{2.79}$$

- the *quantum collection efficiency* $\eta_c(\lambda)$ is the ratio of the number of carriers collected by the solar cell under short-circuit conditions with respect to the total number of photogenerated electron-hole pairs inside the device,

$$\eta_c(\lambda) = \frac{J_{sc}(\lambda)}{J_{ph}(\lambda)} = \frac{EQE(\lambda)}{1 - R(\lambda) - T(\lambda)} \tag{2.80}$$

It is worth mentioning that, while EQE includes the effect of all related optical losses, including transmission and reflection losses, IQE only considers the transmission losses as evidenced in equation (2.79), thus reporting about the efficiency whereby photons that are not reflected by the solar cell generate carriers which are then collected at the cell terminals. Conversely, η_c does not account for the effect of both optical loss mechanisms (according to equation (2.80)), hence referring to the efficiency whereby the solar cell collects the carriers, once generated in the device.

2.5 Carrier Recombination Mechanisms

As discussed in section 2.2, generation and recombination of charge carriers are fundamental to the operation of several optoelectronic semiconductor devices such as solar PV cells. Moreover, it is crucial to know that both processes take place continuously in the crystal structure *c*-Si, where electrons and holes are created and then annihilated. On top of this, under equilibrium conditions, they are equal, and carrier density is constant. The recombination rate U per unit time and volume can be defined as the difference between the recombination rate R and the generation rate G,

$$U = R - G \tag{2.81}$$

The generation of the electron-hole pair is originated when a piece of semiconductor is illuminated by a light pulse with photon energy bigger than the band gap energy; enhancing the transition of electrons from the valence band to the conduction band, leaving

holes behind in the valence band. In order to reach the thermal equilibrium in the system, the reverse process must also occur, the excess electrons in the conduction band will recombine with holes and the energy is released in the form of photons or phonons. The time whereby this event takes place is known as either recombination lifetime or minority carrier lifetime, τ, and it quantifies the recombination losses in the material. Henceforth, recombination lifetime represents the average time an excited electron survives before recombining, and is defined as,

$$\tau = \frac{\Delta n}{U} \tag{2.82}$$

where Δn is the excess carrier concentration for volume unit (cm^{-3}) and U is the volume recombination rate (cm^{-3}/s). Hence, the excess carrier lifetime depends on the doping concentration of the semiconductor as well as the excess carrier density. Then, as it is possible to assume that different recombination rates U_i can occur independently from each other, the total recombination rate U_{total} can be calculated from adding together every single recombination rate. Thereby, the total excess carrier lifetime τ_{eff} is calculated from the inverse sum of the reciprocal carrier lifetimes τ_i, as follows,

$$\begin{aligned} U_{total} &= \sum_i U_i \\ \frac{1}{\tau_{eff}} &= \sum_i \frac{1}{\tau_i} \end{aligned} \tag{2.83}$$

Accordingly, recombination rates strongly determine the performance of PV cells, as the photo-generated charge carriers may recombine before they contribute to the collected current. On the other hand, different types of charge carrier recombination may arise depending on the properties of the semiconductor material and several physical processes. In fact, as our case of study is focused on the *interdigitated back contact* solar cells well-known as IBC structures, we have to set a specific optimization for a given set of recombination and transport properties. Likewise, recombination losses are frequently classified according to the region of the cell where they take place [7, 28]. Thus, the main areas of recombination are usually located in both, the bulk and surface of the wafer. Thereby, the most common recombination mechanisms which contribute to electrical losses in solar PV cells are outlined in the next sections.

2.5.1 Bulk recombination

In the semiconductor, there are a few intrinsic recombination processes, i.e. they are inherent to the existence of separated energy bands of the material. In the substrate of a single-crystal structure, the basic recombination mechanism is composed by the Radiative,

Shockley-Read-Hall (SRH) and Auger (see Fig. 2.13). The effects of the different recombinations add together to a total rate of recombination in the bulk, as described in equation (2.84).

$$R_{Bulk} = (R_{RAD}) + R_{AUGER} + R_{SRH} \tag{2.84}$$

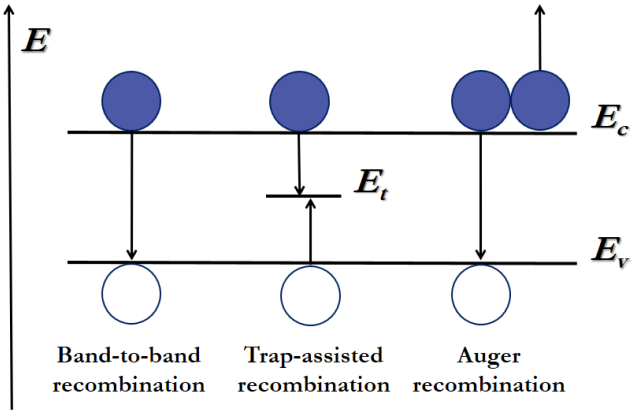

FIGURE 2.13: Schematic of the bulk recombination mechanisms in semiconductors. Taken from [64].

2.5.1.1 Radiative recombination

Radiative recombination also known as direct (band-to-band) recombination is the inverse process of the light absorption. Basically, an electron in the conduction band (E_c) falls back to its previous energy state and directly combines with a hole in the valence band (E_v), releasing the energy as a photon (E_{ph}), as illustrated in Fig. 2.14.

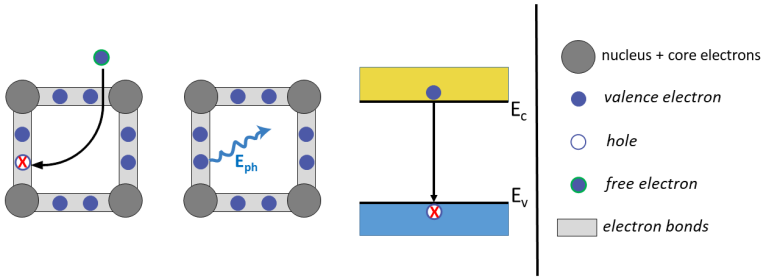

FIGURE 2.14: Radiative or direct recombination mechanism using the bonding model and the energy band diagram [28].

This kind of recombination represents the dominant loss mechanism of photo-generated charge carriers in applications such as space solar cells and concentrators, typically made from direct band-gap materials as gallium arsenide (GaAs), under moderate illumination conditions. However, most terrestrial solar PV cells are made from indirect band-gap materials such as crystalline silicon (*c*-Si) whereby radiative recombination is extremely small and inefficient, and normally negligible. The radiative recombination rate is defined as:

$$R_{RAD} = Bnp \tag{2.85}$$

where B is the radiative recombination coefficient, and n and p are the electrons and holes concentration, respectively. Further, the radiative recombination rate per unit time and volume is expressed as:

$$U_{RAD} = Bnp = B(n_0 + \Delta n)(p_0 + \Delta p) \tag{2.86}$$

where n_0 and p_0 represent the concentration of electrons and holes in dark conditions (due to doping) where there is no incident photons, and Δn and Δp are the excess concentration of electrons and holes respectively (due to light generation). The low value of B measured for silicon ($9.5 \times 10^{-15} cm^3 \cdot s^{-1}$) shows the small probability of occurrence of this type of recombination [72].

As we can see from equation (2.82) and 2.86 the lifetime due to radiative recombination can be defined as:

$$\tau_{RAD} = \frac{\Delta n}{B(n_0 + \Delta n)(p_0 + \Delta p)} \tag{2.87}$$

Nonetheless, radiative recombination is, particularly, a desired and useful mechanism in semiconductor lasers and light emitting diodes (LED).

2.5.1.2 Auger recombination

In comparison to SRH and Radiative or direct recombination which are just two particles, i.e. an electron-hole pair, Auger recombination involves three particles interaction as sketched in Fig. 2.15. This means it is the reverse process of the impact ionization, where an electron and a hole recombine, transferring the excess energy to a nearby third carrier. This can be either an electron excited into higher levels in the conduction band (eeh process) or a hole similarly excited into deeper levels of the valence band (ehh process); instead of emitting the energy as a photon or heat. Finally, the involved third carrier, gradually gives off its energy to the semiconductor crystal lattice by thermal relaxation.

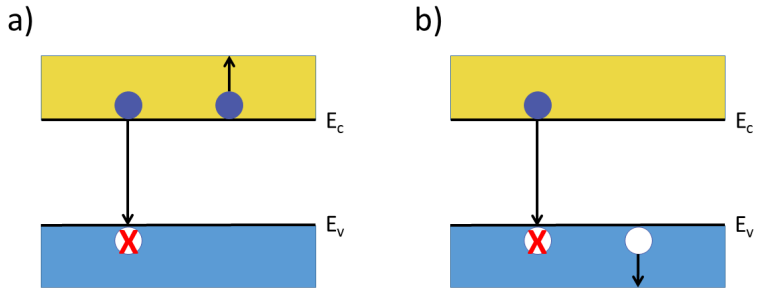

FIGURE 2.15: Illustration of Auger recombination process with a) two electrons; and b) two holes involved. Taken from [28].

Auger recombination is particularly important at highly doped material (which is caused when doping concentration is above $10^{17} cm^{-3}$), and also starts playing a role at very high illumination conditions (i.e. high-level injection under concentrated sunlight). Besides, it is considered one of the main loss mechanisms which must be accounted for when designing highly doped regions of a silicon-based solar cell. Especially, because this kind of recombination process limits the ultimate efficiency and lifetime [73].

As mentioned before, Auger recombination rate U_{AUG} strongly depends on the charge carrier densities for the electrons n and holes p. The recombination rates for the eeh and ehh processes are defined as,

$$R_{eeh} = C_n n^2 p \tag{2.88}$$

$$R_{ehh} = C_p n p^2 \tag{2.89}$$

where C_n and C_p are temperature dependent coefficients [65]. Additionally, R_{eeh} is dominant when the electrons are the majority charge carriers, while R_{ehh} is dominant when the holes are the majority charge carriers. Thus, taking them into account leads to the net Auger recombination rate,

$$\begin{aligned} R_{AUG} &= R_{eeh} + R_{ehh} \\ &= C_n n^2 p + C_p n p^2 \\ &= (C_n n + C_p p)(pn - n_i^2) \end{aligned} \tag{2.90}$$

2.5.1.3 Shockley-Read-Hall recombination

It consists of a recombination process of electron-hole pairs via extra-intermediate energy levels in the band-gap (i.e. presence of impurities and structural defects such as foreign atoms in the semiconductor crystal lattice). Imperfections that create discrete intermediate energy levels inside the forbidden silicon band-gap, acting as traps for charge carriers and thereby completing the recombination rate to a higher degree (see Fig. 2.16). The theory of this mechanism in minority carrier kinetics was only based on statistical considerations proposed by William B. Shockley, William T. Read [74] and Robert N. Hall [75]. Thus, as a reverence to their work, this process it is commonly known as Shockley-Read-Hall or SRH recombination as well as trap-assisted recombination.

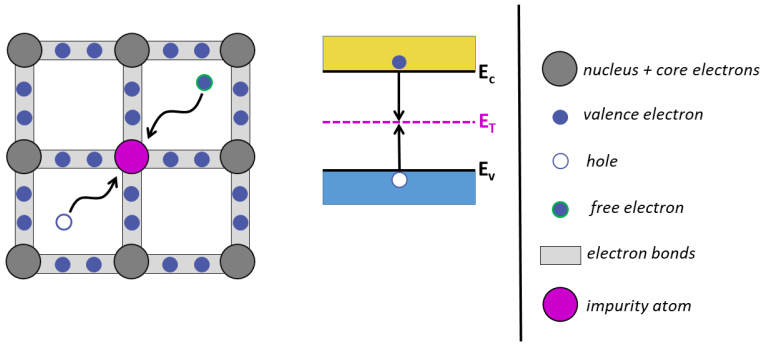

FIGURE 2.16: Sketch of Shockley–Read–Hall (SRH) recombination process using the bonding model and the energy band diagram [28].

The SRH statistics is based on a four-step process that is involved in a single-electron trap recombination, as depicted in Fig. 2.17:

(a) an electron is captured by an unoccupied energy level,

(b) an electron is emitted from an occupied level into the conduction band,

(c) a hole is captured by an occupied energy level,

(d) a hole is emitted into an unoccupied state in the valence band.

To account for Shockley–Read–Hall (SRH) recombination due to defects at material interfaces (either planar and textured), we used the doping dependent models of surface recombination velocity at passivated interfaces, proposed by Glunz et al. [76] with the parameterization reported in [77].

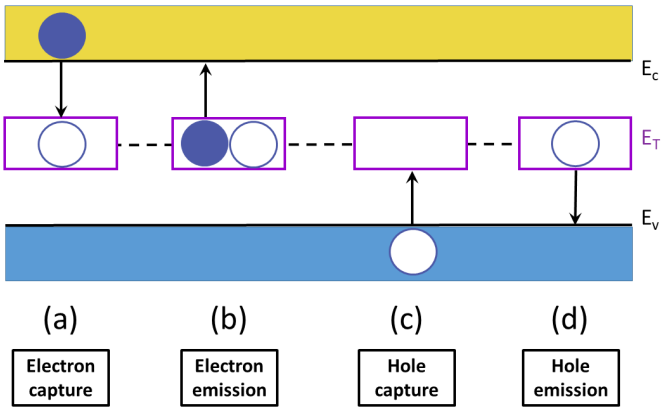

FIGURE 2.17: Sketch of Shockley–Read–Hall (SRH) recombination process using the bonding model and the energy band diagram [28].

The recombination rate caused by a trap-assisted mechanism with a single-energy of the defect level E_t is described by,

$$R_{SRH} = \frac{np - n_{i,eff}^2}{\tau_p \left(n + n_{i,eff} e^{\frac{E_{trap}}{kT}}\right) + \tau_n \left(p + n_{i,eff} e^{-\frac{E_{trap}}{kT}}\right)} \tag{2.91}$$

where τ_n and τ_p are the minority carrier lifetimes for electrons and holes, respectively, and E_{trap} is the difference between the defect level and the intrinsic level, and by default, $E_{trap} = 0$ in crystalline silicon. Usually, τ_n and τ_p are temperature-dependent and doping-dependent. Hence, the carrier lifetime within the crystal lattice may heavily deteriorate through SRH recombination process by the high thermal velocities and a large density of traps.

The doping dependence of the SRH lifetimes is modeled through the Scharfetter relation [45, 78].

$$\tau_{SRH}(N_{dop}) = \tau_{min} + \frac{\tau_{max} - \tau_{min}}{1 + \left(\frac{N_{dop}}{N_{ref}}\right)^{\gamma}} \tag{2.92}$$

where N_{dop} is the bulk doping concentration, and τ_{max}, τ_{min}, N_{ref}, and γ are the tuning parameters of the model. The default values for silicon are: τ_{min} = 0 s, τ_{max} = 10 μs for electrons and τ_{max} = 3 μs for holes, N_{ref} = $1 \times 10^{16} cm^{-3}$, and γ = 1 both for electrons and holes. According to equation (2.92), the SRH lifetimes decrease with increasing doping concentration.

The temperature dependence is described by a power-law [45],

$$\tau_{SRH}(T) = \tau_0 \left(\frac{T}{300K} \right)^{\alpha} \tag{2.93}$$

where τ_0 is the SRH lifetime at 300 K, and by default α = -1.5 for silicon, thus leading to a decrement of the SRH lifetimes with rising temperature [45].

2.5.2 Surface recombination

So far, the recombination mechanisms we have discussed are related to the *bulk recombination* process which takes place inside the substrate or bulk of a semiconductor material. For example, impurities can cause trap states within the semiconductor band-gap leading to Shockley–Read–Hall recombination. However, there is another important type of recombination which significantly impacts the performance of a semiconductor device, and we refer to it as *surface recombination*. This type is promoted by the presence of impurities and crystallographic imperfections at the surface, interface or within the material causing a high local recombination rate.

These defects are denominated *dangling bonds* and generally are originated by interruptions to the periodicity of the silicon crystal lattice. Essentially, the dangling bond occurs when valence electrons on the silicon surface cannot find a partner to create a covalent bond with, leaving an abrupt discontinuity of the crystal lattice, as exhibited in Fig. 2.18 a). As a consequence, dangling bonds enhance the creation of surface energy states in the forbidden band-gap, acting as trapping (recombination) centers for the minority carriers, inducing to *SRH* recombination (see Fig. 2.18b)) [66]. In very pure semiconductors, recombination might be dominated by surface recombination. The *surface recombination rate* R_s for an *n*-type semiconductor can be approximated with [65],

$$R_s \approx v_{th} \sigma_p N_{sT} \left(p_s - p_0 \right) \tag{2.94}$$

where v_{th} is the thermal velocity in cm/s, N_{sT} is the surface trap density in cm^{-2}, and σ_p is the capture cross-section for holes in cm^{-2}. p_s is the hole concentration at the surface and p_0 is the equilibrium hole concentration in the *n*-type semiconductor. For a *p*-type semiconductor, we have to replace σ_p by σ_n, p_s by n_s, and p_0 by n_0. Note that the product $v_{th}\ \sigma\ N_{sT}$ has the unit of a velocity; it is called the *surface recombination velocity*,

$$S_r := v_{th} \sigma N_{sT} \tag{2.95}$$

with σ_p or σ_n for an *n*- or *p*-type semiconductor, respectively. A low surface recombination velocity means that little recombination takes place while a (theoretical) value of S_r = ∞ would mean that every minority carrier coming to the proximity of the surface recombines. It is worth noting that, the presence of dangling bonds or defect (recombination)

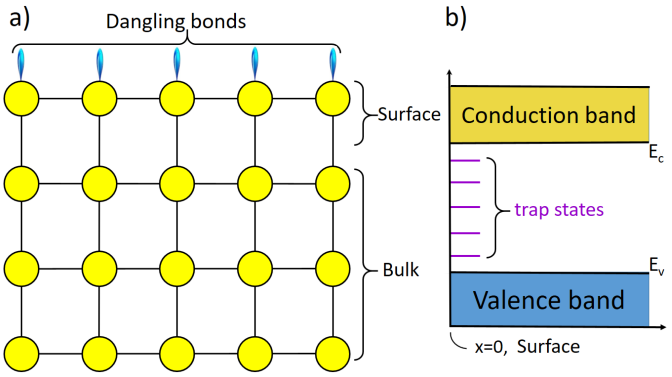

FIGURE 2.18: a) Diagram of dangling bonds (surface defects or crystallographic imperfections) on a semiconductor surface; b) Sketch of the trapping state centers within the band-gap created by the dangling bonds. Taken from [28].

centers minimizes the *effective lifetime* of the excess minority carriers within the semiconductor, limiting the conversion efficiency η of the solar cells. For this reason, in order to boost the performance and quality of the solar cells, it is crucial to have a low *surface recombination velocity* S_r and hence reduce the number of dangling bonds in the silicon crystal lattice. This can be accomplished in two different ways:
1) first, S_r can be made low by reducing the trap density N_{sT}. In semiconductor technology, by depositing a thin layer of a suitable material onto the semiconductor surface can reduce the defect density. Because of this layer, the valence electrons on the surface can form covalent bonds, such that N_{sT} is reduced. This technique is known as *surface passivation* and it will be discussed in more detail in section 2.8.

2) Secondly, the excess minority carrier concentration (of electrons n_s and holes p_s) at the surface can be reduced, for example by high doping of the region just underneath the surface in order to create a barrier. Because of this barrier, the minority carrier concentration is reduced and hence the recombination rate R_s.

2.6 Series and shunt resistances

In a real device, parasitic resistive losses due to a *series resistance* R_s and a *shunt* (or parallel) resistance R_{sh} have to be considered. Accounting for these, the illuminated *I-V* cell characteristics (see equation (2.64)) become,

$$J(V) = J_0 \left[exp\, \frac{q(V - J(V)R_s)}{kT} - 1 \right] + \frac{V - J(V)R_s}{R_{sh}} - J_{ph} \tag{2.96}$$

where V is the voltage at the cell terminals.

The series resistance of a solar cell consists of the resistance of the metal grid, the contact resistances, and the bulk and emitter resistances, while shunt resistance is typically related to crystal defects and impurity precipitates, as well as leakage currents across the *p-n* junction around the edges of the cell. The influence of these resistive components on the dark and illuminated *I-V* characteristics is shown in Fig. 2.19. In particular, focusing on the dark characteristics (Fig. 2.19c) and d)), it is worth noting that a high series resistance causes a deviation from the ideal dark *I-V* curve at high current densities, while a low shunt resistance influences the dark *I-V* curve at small current densities.

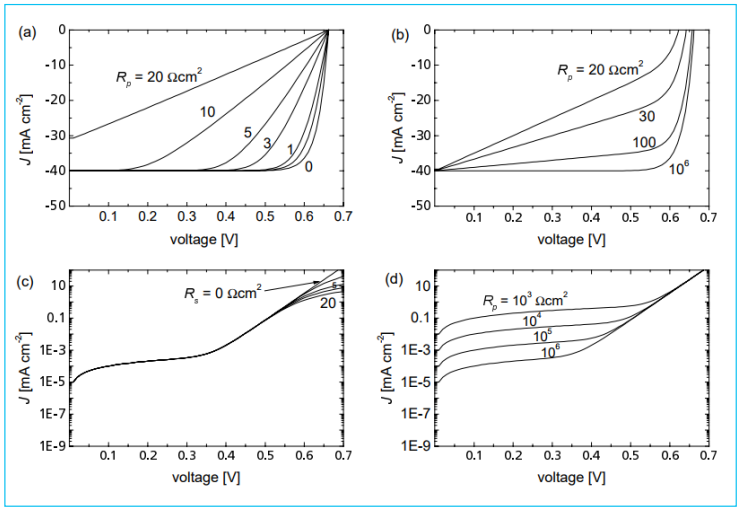

FIGURE 2.19: Influence of series resistance R_s and shunt resistance R_{sh} on the *I-V* cell characteristics: a) illuminated curves for different R_s. b) illuminated curves for different R_{sh}. c) dark curves (logarithmic scale) for different R_s. d) dark curves (logarithmic scale) for different R_{sh}. Taken from [69].

2.7 Effective Lifetime

The minority carrier lifetime of a semiconductor material, symbolized by τ_n or τ_p, is the average time excited carriers spend, immediately after the generation of an electron-hole pair before recombining to re-establish thermal equilibrium. This process is commonly known as *lifetime* and plays a crucial role to assess material quality because it takes into account all kinds of recombination mechanisms. However, some of these mechanisms are

more important than others because the ones with the highest recombination will dominate the measured value of the effective carrier lifetime τ_{eff}. Likewise, *lifetime* depends on the recombination rate which is subordinated upon the minority carriers concentration, as described in equation (2.82). Since the different recombination mechanisms in the bulk (section 2.5.1) and at the surface (section 2.5.2) will typically occur simultaneously within the semiconductor sample, the effective minority carrier recombination lifetime τ_{eff} is defined by,

$$\frac{1}{\tau_{eff}} = \frac{1}{\tau_{Bulk}} + \frac{1}{\tau_{SURF}} \tag{2.97}$$

where τ_{Bulk} and τ_{SURF} represent the bulk and surface recombination lifetimes respectively.

Regarding the bulk recombination, this can be obtained by adding the recombination rates of every single mechanism described in equation (2.84):

$$R_{Bulk} = (R_{RADIATIVE}) + R_{AUGER} + R_{SRH}$$

As the recombination lifetime is inversely proportional to the recombination rate, the total bulk lifetime τ_{Bulk} can be calculated from the inverse sum of the reciprocal carrier lifetimes contributions, as follows,

$$\frac{1}{\tau_{Bulk}} = \frac{1}{\tau_{RAD}} + \frac{1}{\tau_{AUGER}} + \frac{1}{\tau_{SRH}} \tag{2.98}$$

where τ_{RAD} is the lifetime related to the band-to-band or direct recombination, τ_{AUGER} represents the Auger lifetime and τ_{SRH} is the Shockley-Read-Hall lifetime associated with the substrate/bulk defect recombination. In this matters, the contributions of every related carrier lifetime to the total bulk lifetime τ_{Bulk} are depicted in Fig. 2.20. Observe that due to the inverse addition of each lifetime contribution, the τ_{Bulk} is dominated by the recombination process with the lowest minority carrier lifetime at a given injection level.

Hence, by taking into account all recombination mechanisms discussed in section 2.5 the measured τ_{eff} can be calculated using equation (2.83). Thereby, the effective lifetime value is written as,

$$\frac{1}{\tau_{eff}} = \frac{1}{\tau_{RAD}} + \frac{1}{\tau_{AUGER}} + \frac{1}{\tau_{SRH}} + \frac{1}{\tau_{SURF}} \tag{2.99}$$

where τ_{SURF} it refers specifically to the surface recombination lifetime. It is worth highlighting that, the contribution of τ_{SRH} and τ_{SURF} are accounted as an effective extrinsic recombination lifetime, defined by,

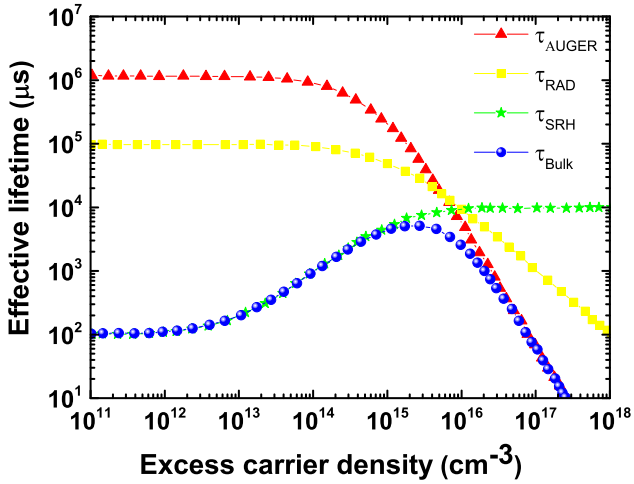

FIGURE 2.20: Validation of the effective lifetime as a function of injection level Δn for all bulk recombination mechanisms discussed in section 2.5.1. The total bulk effective lifetime τ_{Bulk} is shown as a blue line with bubbles ($\tau_{n0} = 100\mu s$, $\tau_{p0} = 1000\mu s$ and $N_A = 1 \times 10^{15} cm^{-3}$). Redesigned with data presented in [79]

$$\frac{1}{\tau_{extr}} = \frac{1}{\tau_{SRH}} + \frac{1}{\tau_{SURF}} \tag{2.100}$$

In the same way, τ_{RAD} and τ_{AUGER} contributions represent the effective intrinsic lifetime extracted from [80], as follows,

$$\frac{1}{\tau_{intr}} = \frac{1}{\tau_{RAD}} + \frac{1}{\tau_{AUGER}} \tag{2.101}$$

In effect, the intrinsic lifetime due to Radiative and Auger recombination is only contingent upon the doping type and concentration. |

Hence, the modeled effective lifetime can be expressed as,

$$\frac{1}{\tau_{eff,modeled}} = \frac{1}{\tau_{intr}} + \frac{1}{\tau_{extr}} \tag{2.102}$$

It is worth mentioning that, in addition to carrier lifetime, carrier transport and diffusion length are also essential to estimate the collection efficiency. For this reason, TCAD Sentaurus suite provides most of these models or either allows updating them (e.g., as the

Auger recombination in our case), in order to perform accurate simulations. In our case of study, depending on the structure, a solar cell made from silicon wafers with a high minority carrier lifetime will generally ensure a better performance and higher efficiency than PV cells made from wafers with short minority carrier lifetimes [81, 82]. Practically, the enhanced effective carrier lifetime τ_{eff} indicates a silicon wafer with a long lifetime. This can be guaranteed by using a high-quality passivation technique on the semiconductor surface (chemical passivation), which basically ties up a portion of the dangling bonds (i.e. impurities or disruptions) in the crystal lattice, notably reducing the defect density N_{sT} and thus, the surface recombination velocity S_r. Recent leading research shows that typical materials used for these chemical passivation layers are silicon nitrides Si_xN_y and thermally grown silicon oxides SiO_x.

Essentially, a silicon nitride layer Si_3N_4 is formed by using plasma enhanced chemical vapour deposition (PE-CVD). And, a silicon oxide SiO_2 layer is deposited by heating up the silicon surface in an oxygen-rich atmosphere, lading to the oxidation of the surface Si atoms. The application of both passivation layers result in a suitably low surface recombination velocity. Therefore, the passivation technique implemented in this thesis is based on the use of Si_3N_4 and SiO_2, powerful strategies of anti-reflective coating (ARC) materials [28].

2.8 Surface passivation techniques

As it was mentioned above, silicon solar cells efficiency continues being degraded and limited by the recombination losses of photogenerated carriers (i.e. electron-hole pairs) that take places at the interfaces and surfaces of the device. However, currently there is a large research activity focus on the implementation of effective processes to minimize the contamination control during fabrication and harmful surface defects. These innovations have let experts to understand that further advances in *c*-Si wafers would be based on interface passivation, carrier-selective contact structures, and tunnel oxide contacts. In order to enhance the quality and performance of solar cells, it is essential to limit the presence of crystallographic defects and external undesirable impurities (i.e. dangling bonds), while also keeping the surface recombination as low as possible. This is accomplished by the growth of an appropriate passivating film on the semiconductor surface (chemical passivation), or by immersing the sample into polar liquids [83–85]. Surface passivation is achieved by the chemical process of depositing a thin layer of a different material on top of a semiconductor surface, which partially restores the bonding periodicity of the atoms in the silicon crystal lattice [86–91]. This leads to a lessened interface defect density of traps N_{sT} and a reduced surface recombination velocity S_r at the Si surface [92].

Surface passivation is a process dependent and highly influenced by many factors such as the cleanliness of chemical baths, surface quality of Si substrate, type of wafer,

processing conditions and timing. Among the useful materials, employed to create thin passivation layers are dielectrics such as silicon oxide [90, 93–97], silicon nitride [98–101], silicon carbide [102, 103] and aluminum oxide [83, 104–106]. Other well-used materials are semiconductors with disordered structure, for example intrinsic hydrogenated amorphous silicon [107, 108] and/or others described in [109]. On the other hand, a passivation layer cannot extract carriers for itself, because they are either insulating or insufficiently conductive. To efficiently extract the photogenerated carriers to the external metal terminals, two-carrier-selective contact structures are required. Ideally, these inner structures exhibit efficient transport of only one type of carrier (e.g., electrons) while blocking the transport of the other type of carrier (e.g., holes). The recombination mechanism process requires the interaction of both types of carriers. Blocking the transport of one of them reduces the recombination probability in the device.

Nonetheless, to suppress recombination mechanism efficiently, it is necessary to place an inter-facial passivation layer over the structure. Therefore, a selective contact presents simultaneously high conductivity for just one of the two carriers while minimizing the recombination rate. Furthermore, regarding the design of high-efficiency solar cells, it is possible to choose to cover most of the wafer surface with a passivation dielectric material and to extract photogenerated carriers selectively through local openings in the insulator [31] or by depositing carrier-selective materials on the full wafer surface using a proper interface-passivation strategy. It is important to carefully select the required material for contact formation considering the optical properties of each material. Passivation layers should be made from a low refractive index material so that it operates like a backside mirror. In practice, it will reflect the light above 900 nm which is not absorbed during the first pass back into the absorber layer. This process enhances the absorption path length by minimizing reflection, and also the parasitic absorption losses, leading to high-efficiency solar cells.

2.9 Loss effects on main figures of merit of solar cells

The performance of a solar cell can be impaired by many factors that can cause losses in the conversion efficiency of the device. Additional effects can negatively impact the three main figures of merit: the short-circuit current J_{sc}, open-circuit voltage V_{oc} and fill factor *FF*. Among the principal losing effects in solar cells, we emphasize the following ones:

- ***Recombination losses***

  The *recombination losses* impact the short-circuit current J_{sc} as well as the open-circuit voltage V_{oc}. This process usually takes place in the bulk, at the surfaces, and also in the depletion region of the solar cell. Since light generated carriers look for re-establishing their thermal equilibrium through the recombination, they must be generated within a diffusion length of the junction. The presence of high surface recombination centers essentially pushes carriers to keep them away from the

junction and help them to recombine quickly. This action drastically affects the V_{oc}. Thus, in order to attenuate these effects, a reduced recombination velocity should be considered. This can be accomplished by applying a surface passivation layer or a doped layer (*back surface field*, BSF) that repeals minority carriers. However, since the BSF region is highly doped, the Auger recombination increases whereas the diffusion length falls, leading to a trade-off between a notable increment of the recombination in the bulk and a decrement of the surface recombination.

- ***Optical losses***

  The *optical losses* are the factor that principally affect the power from a solar cell by reducing the short-circuit current J_{sc}. This effect consists of the reflection of a portion of the incident light from the top and bottom of the silicon surface, preventing the generation of electron-hole pairs, as shown in Fig. 2.21. Nonetheless, the optical losses can be highly reduced using different techniques such as the insertion of a surface texturization and an anti-reflection coatings layer to increase light trapping. Moreover, the presence of front contacts also causes shadowing losses, which is one of the most common sources of optical losses, especially in conventional solar cells.

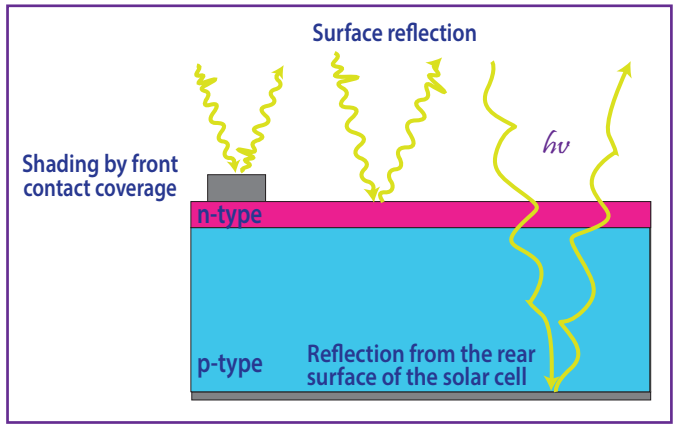

FIGURE 2.21: Schematic of a conventional solar cell illustrating the optical losses effect. Sunlight can be reflected or blocked by the metallic front and back contacts, or either, from the top or rear surface without being absorbed.

- ***Parasitic resistance effects***

  A particular characteristic of solar cells is the presence of an associated parasitic series and shunt resistance losses. The effect of these resistive components on the *I-V* characteristics of a solar cell has been already discussed in section 2.6, and shown in Fig. 2.19. Parasitic resistive losses mainly affect the fill factor of a solar cell. However,

very high values of R_s, and very low values of R_{sh} can also reduce J_{sc} and V_{oc}, respectively, as illustrated in Fig. 2.22 and Fig. 2.23.

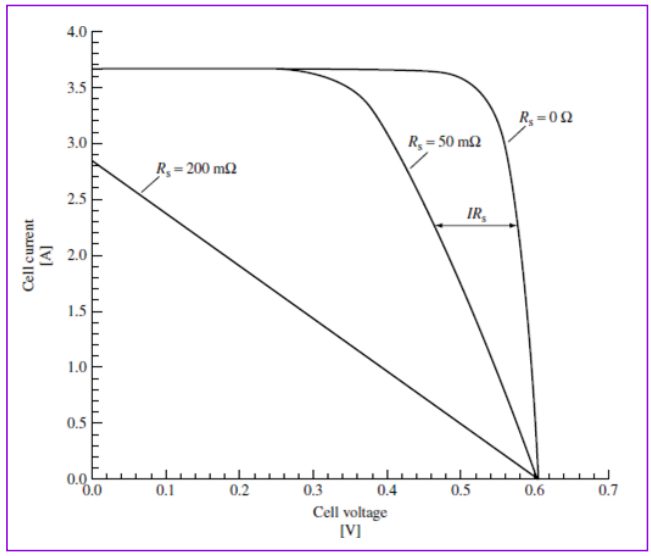

FIGURE 2.22: Effect of the series resistance R_s on the *I-V* characteristics of a solar cell. Taken from [62].

The impact of the series resistance on the FF can be analytically described through the following approximate expression proposed by Green in [68],

$$FF = FF_0 \left(1 - \frac{R_s}{R_{ch}}\right) \tag{2.103}$$

where FF_0 denotes the ideal FF in the absence of parasitic resistances, and $R_{ch} = V_{oc}/I_{sc}$ is defined as the *characteristic resistance* of a solar cell.

A corresponding expression for the effect of the shunt resistance on the FF is given by [68],

$$FF = FF_0 \left[1 - \frac{(V_{oc} + 0.7)}{V_{oc}} \frac{FF_0 R_{ch}}{R_{sh}}\right] \tag{2.104}$$

where V_{oc} is the normalized open-circuit voltage, defined as $V_{oc}/(kT/q)$. The approximated expressions defined by equations (2.103) and (2.104) are particularly accurate under the assumption that $V_{oc} > 10$, $R_s/R_{ch} < 0.4$ and $R_{sh}/R_{ch} > 2.5$ [68].

There are several physical mechanisms responsible for these parasitic resistive effects. The *shunt* or *parallel resistance* R_{sh} is caused by the current leakage across the

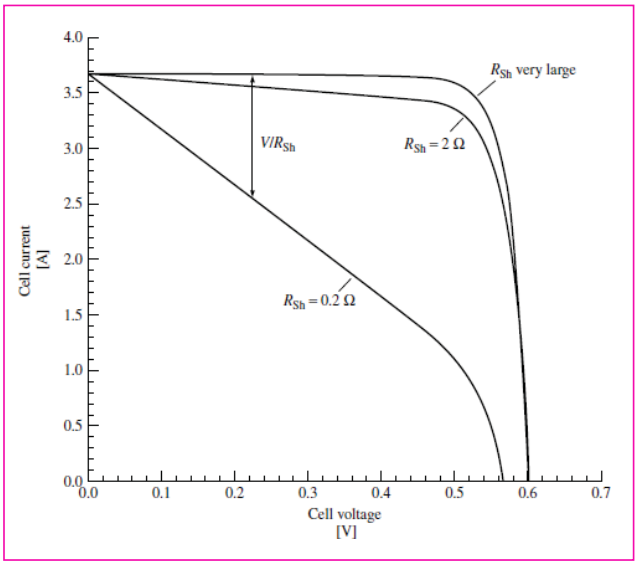

FIGURE 2.23: Effect of the shunt resistance R_{sh} on the *I-V* characteristics of a solar cell. Taken from [62].

p-n junction around the edges of the cell (due to poor edge isolation), and in the regions which present crystal imperfections and impurity precipitates. The total *series resistance* R_s is generally given by the sum of several contributions such as the metal grid resistance, the emitter or diffused layer sheet resistance, the bulk semiconductor resistance and the contact resistance between the metal contact and the silicon interface [110].

- ***Thermal losses (Effect of temperature)***

Semiconductor devices like solar cells are recognized for being sensitive to *temperature* [111]. Recalling equation (2.66), some parameters (e.g., J_{01} and J_{02}) are indeed temperature dependent as follows,

$$J_{01} \propto n_i^2 \tag{2.105}$$

$$J_{02} \propto n_i \tag{2.106}$$

The dark saturation current J_0 increases with temperature according to the next expression,

$$J_0 = BT^{\gamma} exp\left(\frac{-E_{g0}}{kT}\right) \tag{2.107}$$

where B is a parameter independent of temperature, E_{g0} denotes the linearly extrapolated zero temperature band-gap of the semiconductor [68], and γ considers the temperature dependencies of the remaining parameters determining J_0.

The temperature affects some of the most important semiconductor parameters (e.g., the energy band-gap, the minority-carrier lifetime, the diffusion length, the intrinsic carrier density) and, consequently, the performance of a solar cell. The short-circuit current density J_{sc} is not strongly affected by the temperature [68]. Particularly, in silicon-based solar cell devices when the temperature rises, the J_{sc} tends to slightly increase due to the increased light absorption, since the band-gap energy of the semiconductor material *Eg* diminishes, allowing more photons to have enough energy to create electron-hole pairs [66]. This mechanism is known as *band-gap narrowing*, and is also doping dependent. The following expression describes this mechanism,

$$E_g(T) = E_g(0) - \frac{aT^2}{T+b} \tag{2.108}$$

where *a* and *b* represent semiconductor specific coefficients.

In the opposite case, the increment of temperature drastically mitigates the open-circuit voltage V_{oc} (and, hence, the fill factor *FF*, according to equation (2.70)) due to the increase of the saturation current density J_0 [112, 113]. An approximate expression for the variation of V_{oc} in response to a change of the operating temperature is derived by Green in [68],

$$\frac{dV_{oc}}{dT} = -\frac{V_{g0} - V_{oc} + \gamma(kT/q)}{T} \tag{2.109}$$

Where $V_{g0} = E_{g0}/q$ (E_{g0} is the zero temperature band-gap of the semiconductor material), and γ is a temperature-dependent parameter which includes the temperature dependencies of the semiconductor parameters determining J_0 in equation (2.57). Therefore, equation (2.109) predicts an approximately linear decrease of the V_{oc} with increasing temperature. By substituting typical values for a silicon solar cell ($V_{g0} \approx$ 1.2 V, $V_{oc} \approx$ 0.6 V, $\gamma \approx$ 3, T = 300 K), a variation equal to dV_{oc}/d_T=-2.3 mV/°C can be estimated [68]. The considerable decrease of the V_{oc} and, hence, of the *FF*, results in a corresponding decrease of the efficiency of a silicon solar cell with increasing operating temperature.

2.10 Advanced solar cells

During the last thirty years, the PV research community has been focusing their efforts on optimizing the solar cell design and performance, with the main scope of achieving highest efficiencies while reducing typical loss mechanisms and production costs. In this way, innovative cell designs have been studied and developed, stating that the best concepts so far are based on monocrystalline wafers [28]. Silicon-based structures, which feature the highest conversion efficiencies, are classified into three main groups:

- *Passivated Emitter Rear Locally diffused* (PERL) solar cell
- *Silicon Heterojunction solar cell* (SHJ)
- *Interdigitated Back Contact solar cell* (IBC) (also called *back contact-back junction solar cell* (BC-BJ))

In the following sections a short review of these kinds of solar cells is presented.

2.10.1 Passivated Emitter Rear Locally diffused (PERL) solar cell

The *Passivated Emitter Rear Locally diffused* solar cell integrates two important concepts that minimise the recombination centers on the top and bottom of the solar cell. Substantially, the key features of PERL cells are listed as follows, the top surface of the solar cell is textured by using inverted-pyramid structures and covered by double-layer anti-reflecting coating (ARC) which significantly reduces the top surface reflection as well as the amount of carrier recombination. The front metal finger grids are defined by photolithography technology to be very thin therefore minimising metal shading loss. Both inverted-pyramid texturing and fine metal fingers decrease the optical losses which contribute to a higher current for the solar cell (see Fig 2.24). Conversely, at the rear side of the cell, a selective emitter technique is applied (heavily phosphorus diffused regions underneath the metal contacts) whilst the rest of the top surface is lightly diffused to keep excellent "blue response" (absorbing the short-wavelength photons). This can mitigate both contact resistance and recombination at the rear while keeping a good electrical contact. PERL solar cell uses micro-electronic techniques to produce cells with efficiencies approaching 25% under the standard AM1.5 spectrum [31, 55, 114].

2.10.2 Silicon Heterojunction (SHJ) solar cell

The Silicon Heterojunction solar cell is a structure made out of two different silicon-based semiconductor materials. One of these materials is applied as a thin layer between silicon and metal. This technique commonly considers the deposition of a thin amorphous silicon (*a*-Si) layer, demonstrating an evident increment of the open circuit voltage V_{oc} with no need of an expensive patterning process. Since *a*-Si has a wide band-gap layer, V_{oc} is enhanced and the high surface recombination in active metal contacts is lessened. A

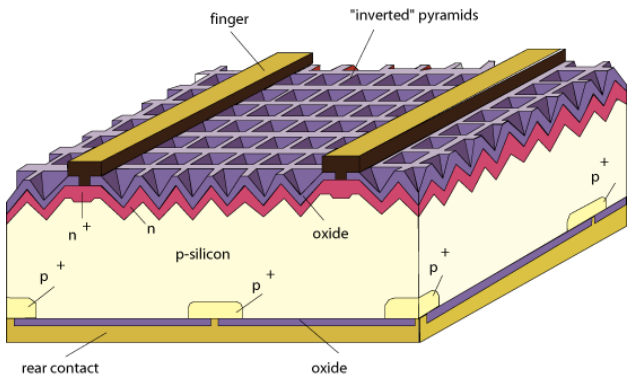

FIGURE 2.24: Structure of a high-efficiency PERL Solar cell. Reprinted from [115].

schematic of a two-dimensional cross view and a band diagram of a typical silicon heterojunction (SHJ) solar cell are illustrated in Fig 2.25. The latest performance record for the heterojunction silicon-based (*c*-Si) concept has reported an open circuit voltage value of $V_{oc} = 0.74V$ and a conversion efficiency equal to $\eta = 25.6\%$ [51].

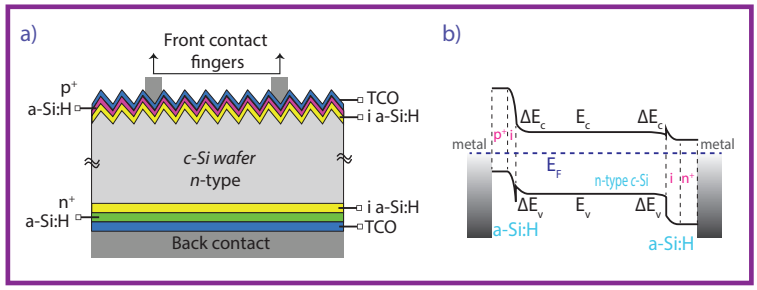

FIGURE 2.25: a) Two-dimensional (2D) cross section of a silicon heterojunction (SHJ) solar cell. b) Corresponding band diagram in dark at equilibrium. Reprinted from [7, 28].

2.10.3 Interdigitated Back Contact solar cell (IBC)

The concept of *Interdigitated Back Contact* solar cell was first analyzed and proposed by Schwartz & Lammert in 1975 as a solution for solar concentrators [30, 116, 117]. This architecture is also known as *back contact-back junction solar cell* (BC-BJ) and consists of a design where both metal contacts are located on the bottom of the *c*-Si wafer, simplifying the cell interconnection at module level. These characteristics of IBC cells also allow boosting the solar cell conversion efficiency η due to the absence of front contact shadowing losses. In

fact, this is the opposite case of traditional PV cells, where metal grids at the front surface are the main cause of electrical shading losses and an attenuated short circuit current J_{sc}. Since back contact-back junction cells are an evolution of conventional solar cells, they offer many other advantages as the possibility of coplanar interconnection and low series resistance, due to the facility of making much larger metallization coverage on the rear side. Nonetheless, some critical parameters must be kept in mind.

Usually, carriers are generated near the top surface because most energetic photons are absorbed almost immediately within the first microns of the wafer. Subsequently, since BC-BJ has the junction on the rear side of the cell, charge carriers have to travel through the whole substrate to reach their respective collection centers, avoiding recombination. With regards to this, *back contact-back junction* solar cells are very sensitive to recombination mechanisms such as SRH in the bulk and at the interfaces [118]. These processes can occur due to an inadequate passivation (i.e. a way to suppress the defects present in the crystal lattice) on the front and back surfaces, and also because of a low effective bulk lifetime τ_{Bulk}, as well as, a high surface recombination velocity at front surface.

Accordingly, the objective of this thesis is mainly focused on the study and analysis of *back contact-back junction* solar cells, because of their attractive advantages and potential design characteristics for enhancing the performance of PV cells [116, 119]. Fig. 2.26 includes a sketch of the structure of a simulated *interdigitated back contact* *n*-type $5\,\Omega\,\mathrm{cm}$ *c*-Si solar cell featuring point contacts on the rear side. This architecture has two alternated phosphorus diffusions (n^+) to create a *front surface field* (FSF) and a *back surface field* (BSF). Likewise, the junction is located on the back side of the cell and it is created by means of the injection of Boron in the *emitter* region.

Thereby, the cell structure has both *n*-type and *p*-type sides alternating on the bottom of the substrate, and they are represented by the BSF and emitter regions, respectively. These regions are responsible for collecting the charge carriers selectively, by directing electrons into the BSF and holes into the emitter. Consequently, collected carriers must flow through their corresponding metal-point contacts located just below the n-type and p-type regions in order to extract power from the PV cell, as illustrated in Fig. 2.26.

On the other hand, the reflective losses on the top side of the cell can be attenuated by the deposition of double-layered anti-reflective coating (ARC) and a texturing on the front surface, using materials such as silicon nitride (Si_3N_4) combined with silicon oxide (SiO_2). Additionally, these can be complemented by a slightly diffused *n*- type layer which generally inhibits the concentration of holes close to the pyramidal texturing in the surface. The same passivation technique is also implemented at the bottom surface of the wafer by placing a thin insulating layer of silicon oxide (SiO_2) [120].

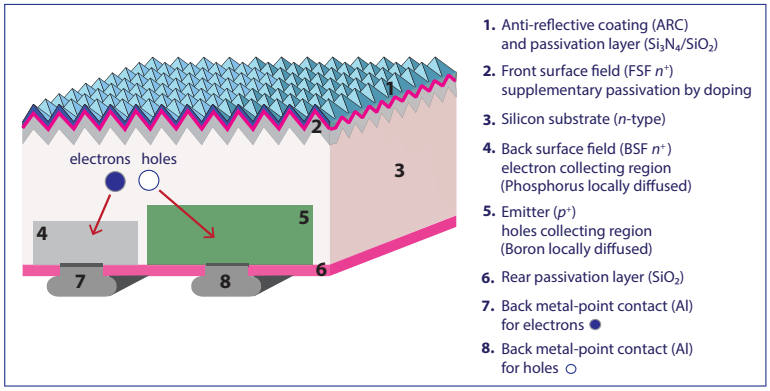

FIGURE 2.26: Diagram of a simulated back contact-back junction (BC-BJ) solar cell featuring point contacts on the rear side. A brief description of all its components is included.

In particular, the optimization of the metal-point contact radius is essential for the efficient carrier collection, which depends on the carrier diffusion length, the recombination properties of phosphorus and boron-doped regions, and peak concentrations. Since electron mobility is approximately three times higher than hole mobility in moderately doped silicon, the p^+ region could cover a larger fraction of the rear pitch and thereby increase the area of collection p-n junction. This increment of the emitter size reduces the build-up of hole concentration at the front surface, mitigating the recombination on the top surface. Electrons generally flow in a lateral way towards the n^+ rear contact lines, not only through the n-type wafer but also through the front n^+ diffusion, when present.

The metal-point contacts make electrical contact through local openings etched into the thin insulating passivation layer. Actually, the openings must be sizable enough to extract current with minimum contact resistance losses and adequately small to minimize recombination losses caused by the direct contact between the interface of the silicon and metal. Accordingly, the thin insulating layer between the silicon and metal-point contact lines attenuates parasitic plasmonic absorption of infrared light in the metal layer [121]. Point contact lines are uniformly distributed and placed below the n-type and p-type regions, as they attempt to avoid overlaps with the neighboring contacts. Despite this, they are moderately narrower than the BSF and emitter regions, and they can almost entirely cover the rear surface, contemporaneously acting as a back reflector. Recently, the Interdigitated Back Contact crystalline silicon-based (c-Si) concept achieved the world's highest conversion efficiencies by over 25% [34, 36, 37] and with the potential to go further.

Chapter 3

Modeling of crystalline Silicon Solar Cells

Modeling of solar cell devices is a wide diffused strategy to analyze internal operation mechanisms by using numerical solution techniques that are capable of managing maximum amount of data, providing reliable and predictable results close to the experimental ones. Its robustness also furnishes new fabrication guidelines that indeed contribute to the time-cost reduction when designing process line setups. Initially, solar cell simulations were performed by employing 1D tools which provided a good approximation by assuming a lateral homogeneity throughout the whole device.

However, innovative photovoltaic technology requires dimensional models. Fig. 3.1 includes a sketch of a 2D and 3D BC-BJ (*back contact-back junction*) solar cell structures featuring point contacts. This is a schematic approach to account for the increase of complexity and its impact on the numerical modeling. In particular, novel solar cells afford might demand extensive numerical modeling simulations to accurately understand and improve solar cell design under various operating conditions, where simple analytical models are deficient. Furthermore, this kind of modeling strongly depends on many intrinsic optoelectronic properties of the material such as lifetime of minority carriers and surface recombination velocity among others.

For this reason, numerical simulation device is a mean for accounting an initial definition of certain parameters, including spatial variation as non-uniform doping, temperature response, material impurities, spectral absorption, high-level injection conditions and two and three-dimensional effects. In this chapter, a review of the state-of-the-art crystalline silicon (*c*-Si) modeling and parameters is presented. In particular, focusing on the numerical electro-optical solar cell simulation by means of Sentaurus Technology Computer-Aided Design (TCAD) tools by Synopsis. Sentaurus implements physical models to represent semiconductor device operation from the design to the fabrication at a micro- or even nanoscale, and support further optimization process [45].

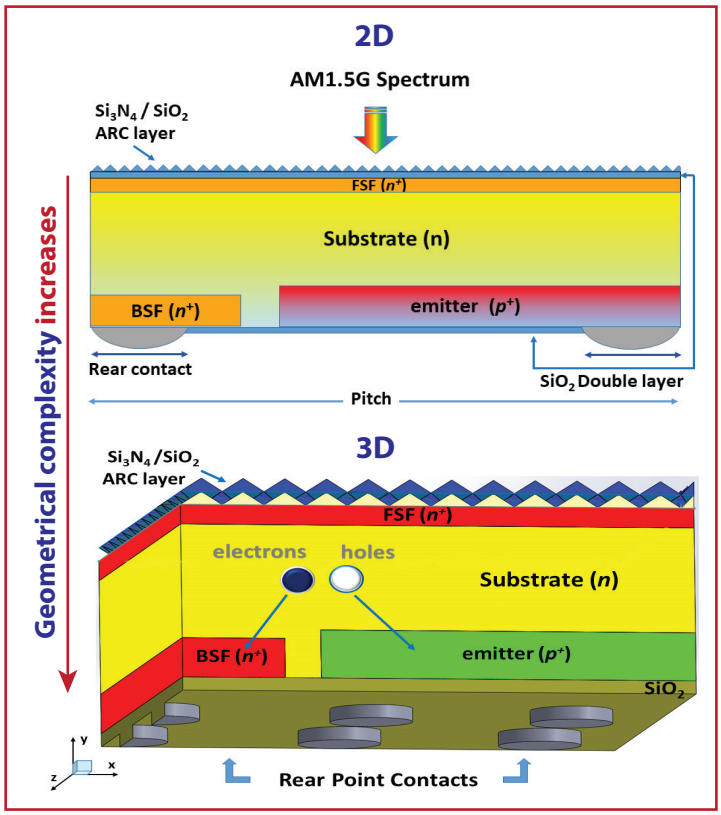

FIGURE 3.1: Schematic of the increase of complexity in novel solar cells, represented by a two-dimensional **2D** and a three-dimensional **3D** BC-BJ solar cell featuring point contacts.

3.1 Numerical simulations

Numerical device simulation is a robust and viable tool that applies a mathematical calculation to emulate real systems, driving to an accurate analysis of solar cell design. Nowadays, many scientific disciplines implement novel numerical modeling to enable the simulation of complex systems under conditions in which experimental analysis demands high-cost, time-consuming and computational resources. Therefore, numerical device simulator is increasingly becoming very important among research groups for the effectiveness on developing innovative projects that require computer simulations to investigate and understand several phenomena that cannot be described by simple analytical models. In this matter, solar cell simulations are based on the mathematical solution of carrier transport problem within a simulation domain including the schematic model of the device. This solution uses a finite element method (FEM) that numerically produce the electrical behavior (i.e.

voltage, current, and charges) of semiconductor devices. Actually FEM is a numerical technique for finding approximate solutions of Maxwell's equations presented in their partial differential or integral form [122]. This simulation approach solves a set of physical device equations that describes the carrier distribution and transport mechanisms according to the so-called Drift-Diffusion Model (TCAD Sentaurus Device). Thus, the solar cell structure approximates to a real device by means of physical properties as geometry, region definition, doping profile and concentration, interfaces and location of electrical contacts. Then, all of them are computed onto a grid-mesh of nodes that are solved numerically, calculating the electrical parameters according to the defined physical and boundary conditions as illustrated in Fig. 3.2.

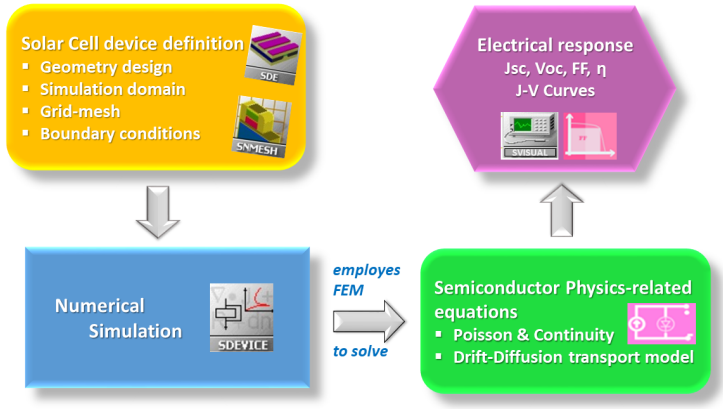

FIGURE 3.2: TCAD Sentaurus-based flowchart for the numerical simulation of solar cells.

Likewise, multidimensional simulations are widely used as the newest standard for accurate modeling, allowing studying the internal behavior of solar cell in detail, pointing out critical issues such as loss mechanisms due to the intrinsic material properties or other specific causes.

3.2 Brief historical overview of solar cell modeling

The first studies on solar cell modeling were made during the 1960's by Bell Labs where a group of Scientists developed an iterative procedure to analytically solve a set of semiconductor device equations with the main objective of applying it to the analysis of photovoltaic devices [123]. Later on, in the early 1980's Purdue University developed the first one-dimensional (1D) solar cell program called SCAP1D (Solar Cell Analysis Program, 1-D) which rapidly was extended to two-dimension analysis [124]. During this time, as the availability of technological resources and computational capacities started being adequate to

support intensive numerical simulations, researchers adopted this method as an essential tool to perform semiconductor device modeling. In particular, several commercial applications were oriented to the specific simulation of silicon materials, typically aimed to one-dimensional numerical modeling. This is the case of the Personal Computer 1 Dimension (PC1D), a wide-spread software package designed for modeling the internal operation of crystalline semiconductor devices with specific features on photovoltaic components [125, 126]. It was developed as a freeware, by Paul A. Basore and Donald A. Clugston from the University of North South Wales (USNW), Australia in the mid-80s [127].

In contrast to other semiconductor modeling software, PC1D is based on a mono-dimensional (axial symmetry) Finite Element Methods (FEM) instead of using finite-difference [128], because FEM hinges on the discretization of semiconductor devices by using grid-mesh. This characteristic allows solving the nonlinear drift-diffusion and Poisson equations by normalizing them in order to simplify the calculations and then discretized the equations on a mesh-grid by applying FEM. In fact, the finite element method is more suitable for the study of complex geometries. Concerning the last process, it assumed some boundary conditions that significantly contributed resolving the semiconductor equations by using a generalized Newton method providing the results of electrostatic potential and carrier concentration at every mesh-grid point. On the other hand, PC1D calculates the doping dependent models for recombination processes that govern the physical phenomena within the solar cell device [129, 130]. It includes a simplified model for the generation enhancement due to texturing and implements fixed trap and charge model.

It is worth pointing out that, research activities and industrial developments on photovoltaic (PV) community have been well supported by PC1D thanks to its specific PV models and continuously improved versions [131, 132]. Therefore, PC1D offers an approach to understanding fundamental solar cell operation [133] by requiring very low computational resources. However, in spite of its success PC1D has some limitations on the accurate analysis of loss mechanisms, the number of time steps in transient simulations [134], and the restricted one-dimensional analysis minimize the possibility to make an accurate investigation of advanced solar cell structures. In addition, PC1D is not suited to perform the modeling analysis of highly doped solar cell regions as back surface field (BSF) and emitter region due to its exclusive implementation of Boltzmann statistics [123]. In the last decades, the imminent necessity and interest for developing novel solar cell structures impelled the adjustment and characterization of general-purpose technological applications capable to accurately solve the set of semiconductor differential equations into a drift-diffusion approximation, accounting for the Fermi-Dirac statistics (Technology Computer-Aided Design, TCAD). As well as, affording multidimensional tools (2D & 3D), to properly undertake PV simulations analysis.

In the early 90s, it appears a new simulator device well known as SIMUL. This software became very famous among the electronic industry because of its improved numerical and mesh-grid methods [135–137]. The University of North South Wales in Sydney, used SIMUL to analyze high-efficiency silicon solar cell [138–140], notably contributing to reaching the new world record efficiency in 1994 [141, 142]. Subsequently, SIMUL was replaced under a brand new version called DESSIS (Device Simulation for Smart Integrated Systems), the former version of the current powerful TCAD modeling software Sentaurus by Synopsis [45]. In particular, DESSIS was especially applied to the analysis of emitters with a mesh structure, rear contacts [143–145] and later its three-dimensional version made solar cell modeling feasible [146]. Hence, DESSIS and Sentaurus gained an important position not only in the research field but also in the recently prominent photovoltaic industry. Nowadays, TCAD modeling software Sentaurus includes a suite of tools which support the simulation process of designing, fabrication and device operation; providing a reliable investigation and the optimization of new semiconductor devices with the main characteristic of reducing time and testing costs [45]. According to the electronic design automation (EDA) software firm, Sentaurus rapidly was quote as a good reference among a set of semiconductor software for simulating the electrical behavior of several types of solar cell devices.

3.3 TCAD-based modeling

This thesis implements numerical simulations of crystalline silicon solar cells performed in TCAD Sentaurus suite by Synopsis, which is a modeling framework featuring a wide variety of tools for designing, simulating, investigate and optimize semiconductor devices. TCAD Sentaurus integrates a multidimensional *Finite Element Method* (FEM) with a set of physical models combined with a broad suite of optical simulators, characteristics that offer the proper tools for undertaking a rigorous and precise analysis of the performance of advanced solar cells. In this work, the modeling approach adopted for the electro-optical numerical simulation of the *interdigitated back contact* (IBC) solar cell is based on the typical TCAD Sentaurus tool flow diagram, depicted in Fig. 3.3.

Basically, TCAD-based simulations include a *device structure definition* also known as Sentaurus Structure Editor (see Fig. 3.3 ①) which allows creating, designing and editing the desired solar cell architecture in two and three dimensions (2D and 3D) by using geometric operations, defining the suitable material properties (e.g., semiconductors, metals and dielectrics), and specifying the doping concentrations of every region in the semiconductor, among other important input parameters [147]. Afterward, by using the Sentaurus Mesh tool, a grid mesh is defined and generated in the created structure. The doping profiles and the generated mesh are then introduced to the electro-optical simulator well-known as Sentaurus Device. At this point, TCAD Sentaurus works separately into an *optical simulation* and an *electrical simulation*. The optical simulation computes the photogeneration

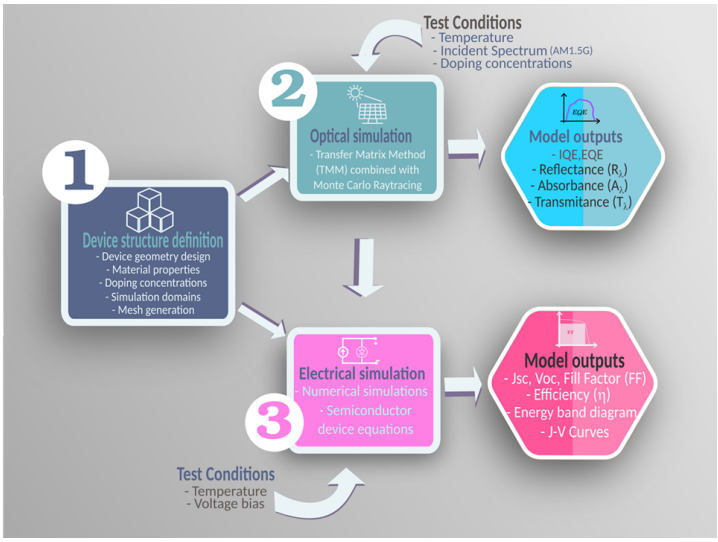

FIGURE 3.3: TCAD Sentaurus-based flow diagram for the electro-optical numerical simulation of solar cells.

rate inside the semiconductor device, taking into account parameters such as the incident solar spectrum and temperature, as illustrated in Fig. 3.3 ②. Then, the output information is used to perform the electrical simulation of a highly symmetric domain area in 2D or 3D, under illuminated conditions, as shown in Fig. 3.3 ③. Finally, the related optical and electrical characterization parameters (i.e. the figures of merit) corresponding to the simulated solar cell, are extracted from the outputs generated through the electro-optical simulation processes by using the Sentaurus Visual from the TCAD suite [45]. In the following section are summarized all the *c*-Si models and parameters used in this work.

3.3.1 Device structure definition

As mentioned in section 3.3 in order to create the *interdigitated back contact* solar cell it is necessary to define some input parameters required by the TCAD simulator. First of all, we have to establish the geometry related to the specific *IBC* architecture such as general dimensions, 2D or 3D ambient, regions distribution, and metallic contact shape and size. Second, the properties of the semiconductor materials like crystalline silicon (*c*-Si), passivation layers such as silicon nitrides Si_xN_y and silicon oxides SiO_x, and the metal coverage like aluminum Al. Subsequently, the doping profiles data and grid mesh are specified to complete the definition of the structure for the electro-optical simulation.

Solar cells are normally large area devices with dimensions in the order of centimeters. Consequently, simulating the whole 3D cell would demand a huge computational effort.

Nonetheless, since the solar cell structures are highly symmetric it is not required to simulate the entire device area. Thereby, the *simulation domain* can be reduced to a geometrically small and periodic segment of the structure that contains most of the physics, representing the behavior of the whole device. In the case of three dimensions cell devices, the simulation domain represents a quarter of the symmetry element, as depicted in Fig. 3.4.

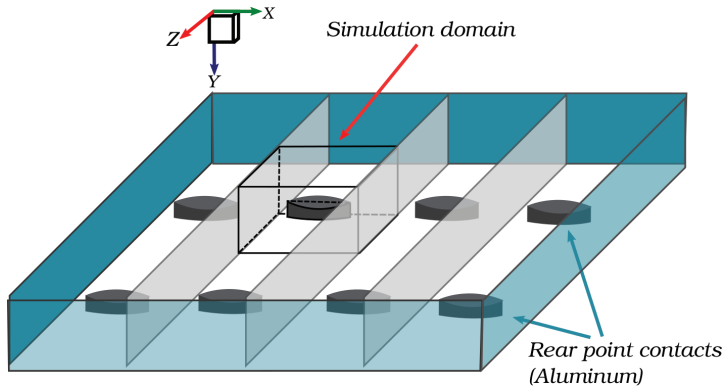

FIGURE 3.4: Simulation domain of a three-dimensional (3D) *interdigitated back contact* (IBC) solar cell, featuring point contacts. Redesigned from [45].

Then, the *discretization grid mesh* of the solar structure is defined, right after the simulation domain is mindfully selected, considering the main characteristics of the device materials and regions in terms of boundaries, doping concentrations and electrical contacts location. In fact, meshing strategy is an essential stage of device modeling because leads to determining an accurate and efficient simulation. Fig. 3.5 illustrates a two-dimensional (2D) and a three-dimensional (3D) generated grid mesh with the considered simulation domain for the simulated point contact (PC) BC-BJ solar cell [45].

On the other hand, it is important to know that the mesh engine does not commonly generate uniform and regular grid because theoretically, in some regions it must be finer enough to get accurate simulation results. Despite this, we have to consider that over-refined mesh normally leads to a very long simulation time without realistic improvements. Therefore, we have to define an adequate mesh strategy accounting for reliable and precise results in an acceptable simulation run-time. In terms of electrical simulations, solar cells mesh refinements are generally necessary in specific areas like the nearby regions to the *p-n* junction (i.e. emitter region and BSF region, where there is a critical doping gradient), at the silicon-metal contact interfaces, where current crowding takes place, and also, at the front surface, where the absorption of most energetic photons occurs (determining the optical

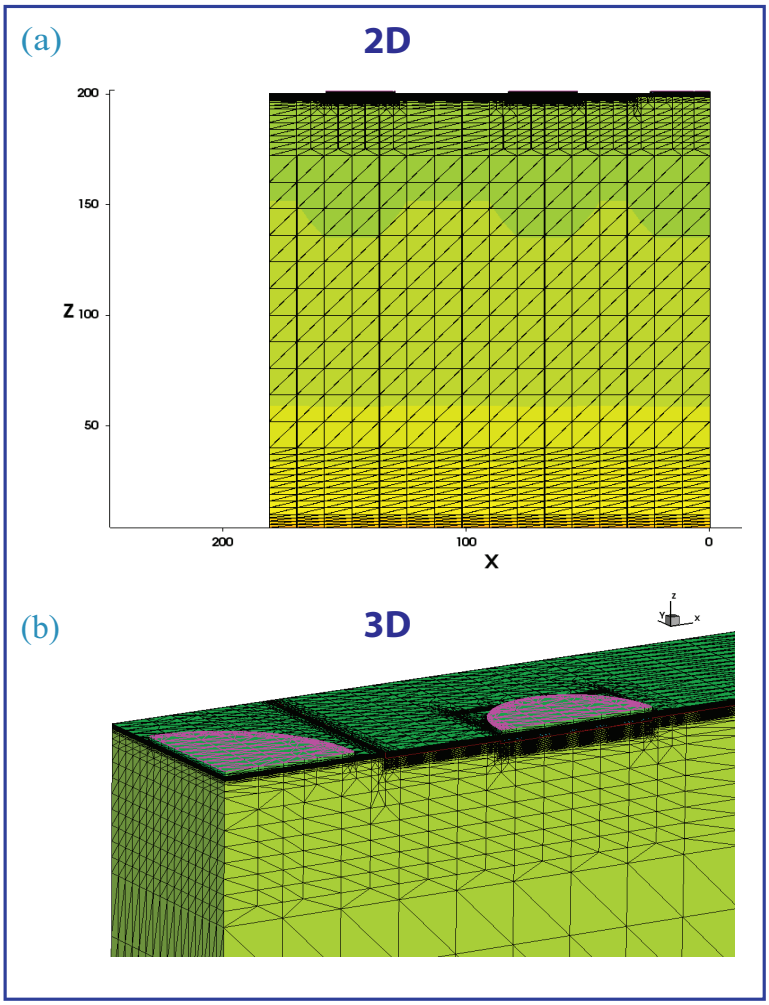

FIGURE 3.5: Schematic of the generated discretization grid mesh in a 2D and 3D simulation domains for the simulated PC BC-BJ solar cell [45].

generation rate of the cell), and the surface recombination requires being modeled properly. Likewise, since the electrical and optical simulations are evaluated independently, the mesh resolution for the optical analysis must consider the effects of surface texturing on the charge collection. So, a solar cell featuring pyramidal front texturing (see Fig. 3.6(a)) needs to model a few or only one pyramid to analyze the optical behavior of the entire device, as depicted in Fig. 3.6(b). Consequently, the generated mesh passes to the electro-optical simulator which calculates the one-dimensional optical generation profile $G(\zeta)$ which is a spatial function that contains the number of the carrier generated through all the thin layer stacks (ARC) and goes as an input to the electrical simulation domain, assigning a value to each 3D-mesh-grid by vertex-based linear interpolation.

The interdigitated back contact solar cells featuring point contact metallization require a three-dimensional simulation domain and cannot be approximated with a two-dimensional finger geometry for the following reasons. First, the *resistive losses* are proportional to ρj^2, where ρ is the contact resistivity and j is the local current density, which differs considerably between finger and point-like geometries. Second, the *recombination losses* depend highly on the minority carrier density, given by the quasi-Fermi level $E_{F,min}$, and is connected to j via $j \propto \nabla E_{F,min}$, (see Fig. 3.6 (c)). So, a two-dimensional approach of point contact scheme can generate errors in the *resistive* and the *recombination losses* [123]. Moreover, in this thesis for the analysis of the point contact *PC* schemes, we have considered that the metallization in the rear surface of the cell is thick and wide, contacting the silicon only via small circular-shaped holes [36]. Specific details are presented in chapter 4, section 4.2.

3.3.2 Optical simulation

The simulation of solar cell devices under illumination conditions requires an accurate modeling of the light propagation and then calculate the carrier generation rate (electron-hole pairs) within the device through all the absorbing layers. The photogeneration rate is not uniform in the semiconductor, it depends on the position. Actually, most of the photogeneration occurs at the first microns of the upper surface of the cell. The optical simulation process ② takes as input the geometry of the various device regions (semiconductor, metals and ARC) accounting for the different optical properties of the materials (see Fig. 3.7).

Then, it calculates the one-dimensional (1D) optical generation rate G(ζ) as a function of position, where ζ is the equivalent distance from the upper surface to the bottom side of the device. The purpose of using ζ rather than depth is that it converts the generation profile under a complicated geometry such as random pyramids to an equivalent generation profile of a planar surface, [149]. The optical generation profile is calculated by taking as input the conventional AM1.5G solar spectrum with data chosen per international standard IEC 60904-3-Ed2 [150] and an integrated irradiance of $1000\,\mathrm{W\,m^{-2}}$, also known as one-sun solar spectrum (see Fig. 3.8), in the wavelength range 0 to infinity.

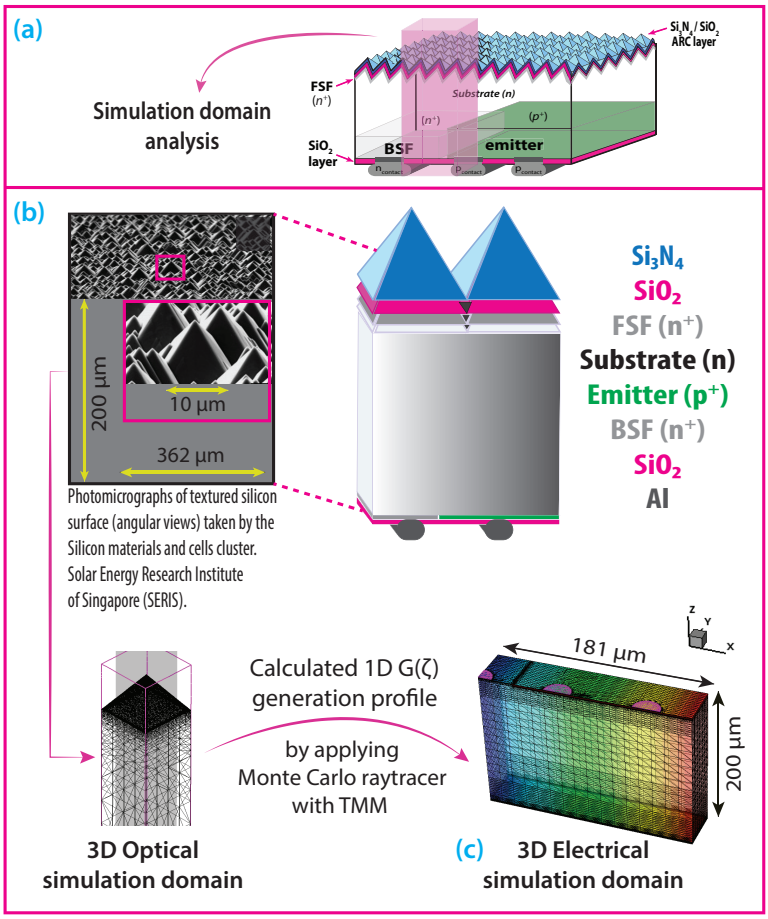

FIGURE 3.6: (a) Three-dimensional IBC solar cell structure featuring point contacts. The simulation domain is highlighted in pink. (b) The 3D optical simulation domain calculates the one-dimensional $G(\zeta)$ optical generation rate by applying the Tranfer Matrix Method (TMM) combined with Monte Carlo Raytracing. (c) The 3D electrical simulation domain implements the generated 1D $G(\zeta)$ optical profile. Redesigned from [148].

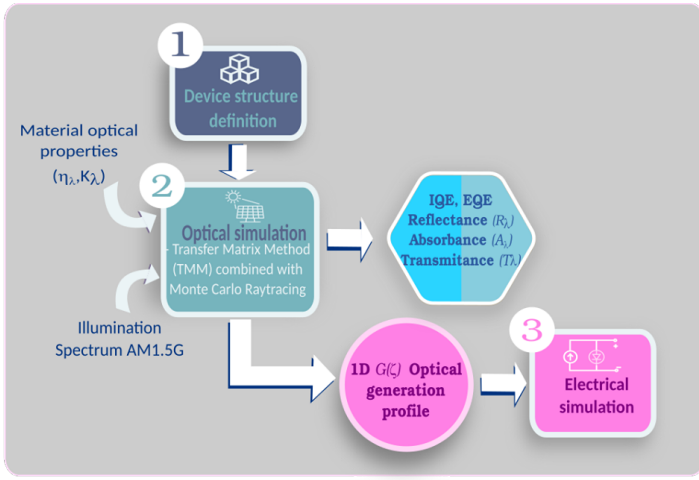

FIGURE 3.7: TCAD Sentaurus-based flow diagram for the optical simulation of solar cells [45].

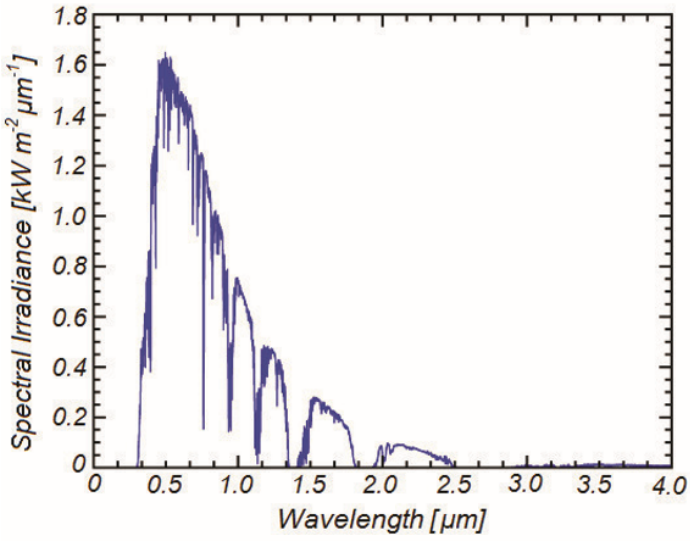

FIGURE 3.8: Conventional AM1.5G solar spectrum with an incident power of $1000\,\mathrm{W\,m^{-2}}$.

In addition to the optical generation rate due to photon absorption of a given wavelength, the spatial distribution of the total optical generation rate G(ζ) is typically extracted from a full-spectrum computation, i.e., by summing the optical generation rates due to photons of all the wavelengths in the solar spectrum. The optical simulation provides also the optical response of the device (i.e., reflectance, transmittance and absorbance) as a function of the wavelength λ of the radiation (see Fig. 3.9).

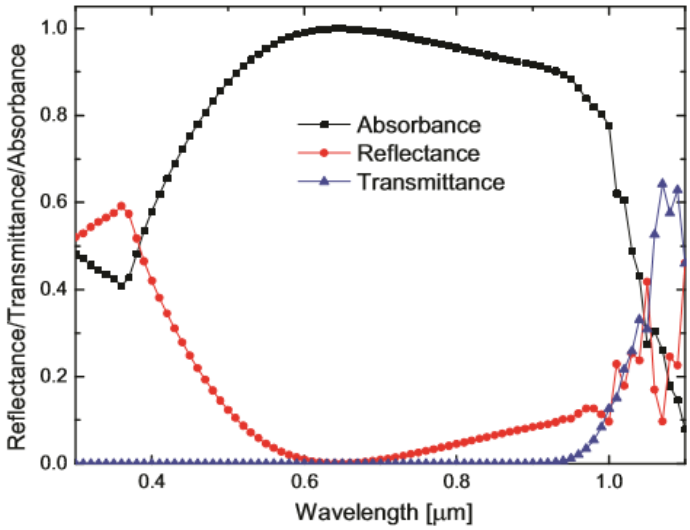

FIGURE 3.9: Example of simulated reflectance, transmittance and absorbance curves for a conventional silicon solar cell.

Once calculated the 1D $G(\zeta)$ optical generation profile, it goes as an input to the electrical simulation process ③, which uses this information to give each mesh-point a generation rate value and predicts the behavior of the device. Fig. 3.10 includes a graphical representation of the main processes related to the TCAD Sentaurus-based electro-optical simulation, considering both simulation domains for a back contact-back junction (BC-BJ) solar cell.

Surface texturing is considered an effective way to increase the solar cell efficiency by improving the light absorption capability [151–154]. However, the modeling complexity increases depending on the type of texturing that should be analyzed. For instance, very irregular ones demand a three-dimensional analysis to obtain accurate results [155]. To solve the optical modeling, it was implemented a three-dimensional (3D) Monte Carlo Raytracing technique allowing to determinate the optic inner interactions of solar cells featuring different patterns of surface texturing. The advantage of using Monte Carlo Raytracing

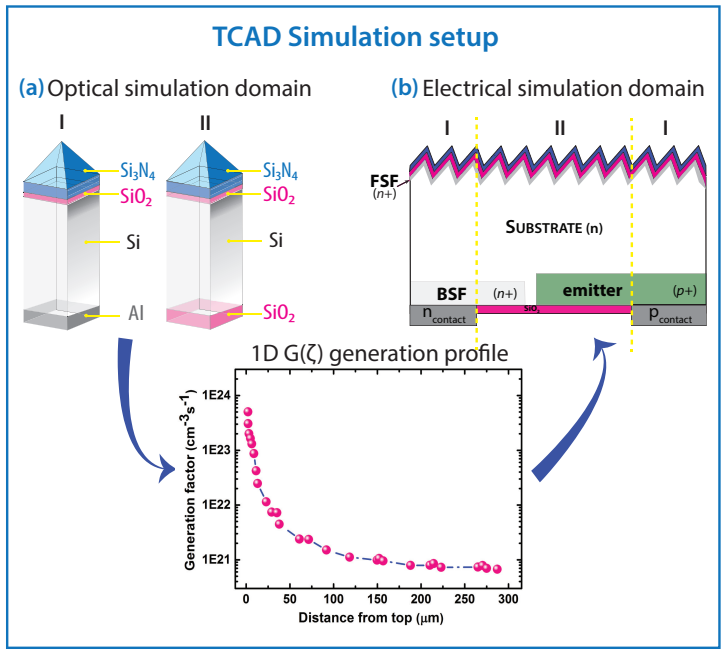

FIGURE 3.10: TCAD Sentaurus-based electro-optical simulation setup for a BC-BJ solar cell.

instead of the regular Raytracing method, it is that the first one only analyzes one propagating beam rather than all split rays for the calculations. So, by far, Monte Carlo Raytracer is faster, but to be statistically consistent it requires an enough higher ray density. For the structures analyzed in this thesis, a distribution of $400\,\mathrm{rays}/\mu\mathrm{m}^2$ over the surface produces comparable results with literature and measurements. The optical output parameters that describe the behavior of solar cells have been described in section 2.4.5.

Nowadays, most of the commercial mono- crystalline silicon solar cells feature front surfaces textured with random arrays of pyramids with a height ranging from $1 - 10\ \mu\mathrm{m}$. Usually, formed by applying a wet an-isotropic chemical etching process over the planar {100} surface of the devices that obtains a pyramidal roughness because it reveals the planes {111} of the silicon [156]. After the texturing step, a double-layer antireflection coating (ARC), formed either silicon nitride (SiN_x) or titanium oxide (TiO_x) combined with silicon oxide (SiO_2) is applied in such a way that covers the surface. The ARC is created by deposition, one on top of another, over the textured silicon surface to reduce even more the reflection losses and also passivate the semiconductor's surface. The combination of both, surface texturing with the ARC layers, improve a lot a solar cell's ability to absorb light but, on the other hand, complicate the numerical assessment of its optics required to computational evaluate its inner working. The surface texture causes that light to reflect many times from the front surface. Thus, reflection, absorption, and transmission must be calculated

for each "bounce" of light and combined correctly to determine the total reflection, absorption, and transmission. In so doing, it is necessary to calculate how the texture alters the angle of incidence and the polarization of the light. The complexity of the optical structure can be resolved by means geometrical ray tracing solver as long as the features of the simulation domain are significant enough to render diffractive effects negligible. To complicate matters further, the ARC layer introduces interference; therefore, reflection, absorption, and transmission are dependents of the thickness, refractive index $\tilde{n}(\lambda)$ and extinction coefficient $\kappa(\lambda)$ that characterizes each material. Moreover, the interference depends on $\tilde{n}(\lambda)$ of the overlying layer and $\tilde{n}(\lambda)$ and $\kappa(\lambda)$ of the underlying semiconductor. Besides, the interference depends on the angle and polarization of the incident light, an ARC can consist of multiple thin films, and $\tilde{n}(\lambda)$ and $\kappa(\lambda)$ can vary significantly with wavelength. In this chapter, it is in-depth analyzed the numerical evaluation of the optical behavior of IBC solar cells by using Sentaurus TCAD and present some interesting results regarding ARC optimization. Simulation of PV devices under illumination requires an accurate modeling of light propagation and optical carrier generation within the absorbing material of solar cell.

The illumination source file numerically coupling, by Sentaurus TCAD, to the simulation domain that contains the geometry structure, meshing and optical physics information of materials to calculate the photogeneration rate of electron-hole pairs by solving the transport equations. Before to resolving the semiconductor device equations for a device operating under illumination, it is necessary first to determine the spatial distribution of the optical generation rate as a function of the wavelength (λ) of the radiation. The solar spectrum file sweeps the wavelength of incident sunlight from the blue region of the spectrum ($300\,\mathrm{nm}$) up to the infrared region ($1200\,\mathrm{nm}$). The solar radiation goes into the simulator as a file created in base the conventional one-sun AM1.5G spectrum with an incident power of $1000\,\mathrm{W\,m^{-2}}$, defined in a text file that has a two-column format. The first column contains the wavelength in $\mu\mathrm{m}$ and the second one contains the intensity in $\mathrm{W\,cm^{-2}}$. This file is calculated based on the air mass 1.5 global tilted irradiance, by the spectral radiation model called SMARTS v 2.9.2 with inputs chosen per international standard IEC 60904-3-Ed2 [157]. The algorithm model allows selecting the frequency interval as well as the step to calculate the irradiance and cumulative photon flux to each wavelength keeping the integral of the intensity as close as possible to the measured. The optical simulator also calculates the effectiveness in transmitting radiant energy (i.e., reflectance, transmittance, and absorbance) as a function of the wavelength (λ) of the radiation.

The key physical parameter, regarding optics, is the complex refractive index $\tilde{n}^*(\lambda)$, that describes how light propagates through the materials. The real part of it accounts for refraction, while the imaginary handles the attenuation. The complex refractive index model used in Sentaurus TCAD is expressed as:

$$\tilde{n}^*(\lambda) = \tilde{n}(\lambda) + i\kappa(\lambda) \tag{3.1}$$

with:

$$\tilde{n}(\lambda) = n_0 + \Delta n_\lambda + \Delta n_T + \Delta n_{carr} + \Delta n_{gain} \tag{3.2}$$

$$\kappa(\lambda) = \kappa_0 + \Delta\kappa_\lambda + \Delta\kappa_{carr} \tag{3.3}$$

The real part, $\tilde{n}(\lambda)$, is composed of the base refractive index n_0, and some correction parameters including the dependency on wavelength, temperature, carrier density, and gain. The imaginary part, $\kappa(\lambda)$, is composed of the base extinction coefficient κ_0 , and the correction terms $\Delta\kappa_\lambda$ and $\Delta\kappa_{carr}$, correspond to the dependency on wavelength and carrier density. More details of the correction factors are discussed in [45].

Furthermore, the absorption coefficient α is computed from κ and wavelength λ according to:

$$\alpha = \frac{4\pi}{\lambda} \cdot \kappa \tag{3.4}$$

The absorption coefficient determines how far inside a material the light, with a particular wavelength, can penetrate before being absorbed to create electron-holes pairs. In materials with a low absorption coefficient or thin enough, light is inefficiently absorbed, and those will appear as transparent (depending on the wavelength). Semiconductor materials can only absorb energy from particles that have sufficient energy to excite an electron from the valence band to the conduction band. It is important to highlight that the analysis limited to sufficiently large enough structures in which the diffraction effects are negligible [158]. The optical simulation domains are *3D* structures that consider three types of top surface geometry: flat, regular pyramid, and random pyramid. The substrate is an *n*-type ($5\,\Omega\,\mathrm{cm}$) *c*-Si that features 10 x 10 x $200\,\mu\mathrm{m}$ with a back flat surface in all three cases. The Front side is covered by a double Si_3N_4/SiO_2 anti-reflective coating (ARC) layer and features a front surface field (FSF) modeled by a Gaussian function with a surface peak doping concentration (C_{peak}) of 3.5×10^{18} cm^{-3} and a junction depth (J_{depth}) of 0.45 μm [159]. The rear side is passivated by a SiO_2 thin layer. The BSF and emitter doping profiles are also modeled by Gaussian functions featuring a C_{peak} of 1.70×10^{20} cm^{-3} and 5×10^{19} cm^{-3}, and a J_{depth} of 0.8 μm and 1 μm, respectively. The 1D optical profiles were extracted from 3D optical simulations, accounting for a texturized front interface with regular pyramids featuring a 10 μm base and a 54.7° base angle, and a planar rear interface with a different bottom internal reflectivity at SiO_2-passivated and contacted surfaces, respectively [160].

It is a common practice to select only a representative portion of a symmetric structure, often half of a symmetric element in two dimensions or a quarter of the symmetric element in three dimensions. However, in this section, due to the asymmetric nature of the random-pyramid textured structure and considering the intention to maintain the same simulation

domain for all three cases, such a simplification is omitted in the flat surface and regular-pyramid surface. The optical solver gives a photogeneration value to each mesh-grid point.

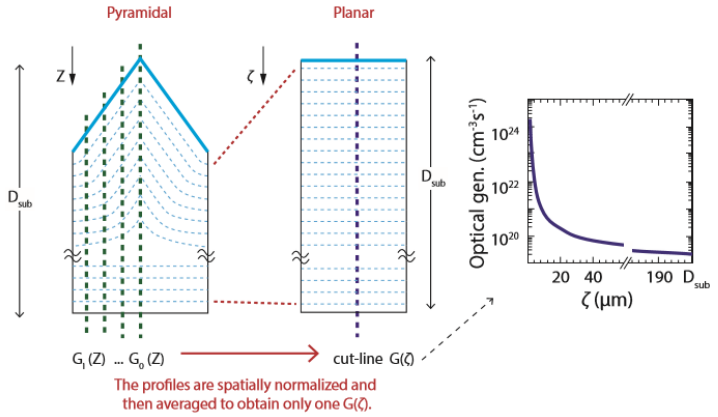

FIGURE 3.11: Two-dimensional view of the normalization and averaging process to extract $G(\zeta)$ in the optical domain.

The generation rate $G(z)$, resulting from the optical simulation, is a 3D spatial function that expresses the inner charge generation produced by the light radiation in the optical domain. By interpolation through all the 3D mesh-grid points, and after averaged and normalized $G(z)$ becomes a one-dimensional spatial function $G(\zeta)$ [161, 162]. This resulting function becomes an input in the electrical domain which does not have texture but instead is flat, as in Fig. 3.11. Since the optical and electrical modeling does not have the same dimensions, neither equal meshing, the simulator interpolates $G(\zeta)$ to give each mesh-point a generation value. Currently, there are not precise analytical methods to predict the 1D profile, because of the complexity of the surface roughness. The analytical expression that defines $G(\zeta)$ is:

$$G(\zeta) = \frac{1}{MN} \sum_{i=1}^{N} \sum_{j=1}^{M} G(x_i, y_j, z) \frac{t_{i,j}}{D_{sub}} \tag{3.5}$$

where $G(x_i, y_j, z)$ is the profile extracted in the point (i, j) (of the plane $x-y$) with an depth from the surface to bottom $t_{i,j}$. The term D_{sub} refers to the substrate thickness of the electrical simulation domain. Meanwhile, M and N are the number of picked points in the axes x and y respectively. Fig. 3.12 shows a comparison of two methods, Opal and Montecarlo-Raytracing implemented to obtain the two optical generation proles $G(\zeta)$ which are quite similar as expected. It is worth mentioning that Opal does not consider the rear thin passivated side (SiO_2) reason why we prefer using Montecarlo-Raytracing.

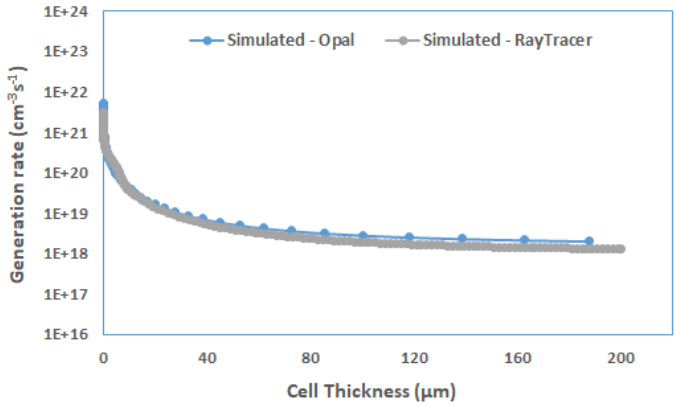

FIGURE 3.12: 1D optical generation profiles $G(\zeta)$ considering two different methods.

3.3.3 Electrical simulation

In order to describe the electrical characteristics of a crystalline silicon (*c*-Si) solar cell, it is necessary to adopt a TCAD-based simulation (by means of numerical discretization employing the finite element method *FEM*) to solve the fully coupled set of semiconductor physics equations within the drift-diffusion approximation, Poisson and continuity equations, accounting also for the Fermi-Dirac statistics. [45, 135]. The constitutive semiconductor equations already mentioned have been described in detail in section 2.3. As shown in Fig. 3.13, the electrical simulation process ③ takes as input a file including the 1D, 2D or 3D generated grid mesh and the doping profiles of the solar cell from the device structure definition process ①.

Additionally, the electrical simulation process depends on the physical models and parameters implemented in the device simulator and especially on the setting of the boundary conditions at the cell device interfaces (i.e. at metal-silicon and at silicon-dielectric surfaces). Then, the 3D electrical simulation implements the generated 1D $G(\zeta)$ optical profile and performs voltage sweeps, and calculates the output current density in presence or absence of the incident sunlight. Subsequently, the simulator provides the *J-V* characteristics of the solar cell under illumination conditions or by an applied forward bias, also known as dark simulation.

It is worth mentioning that in order to run realistic electrical simulations of solar cells it is required to adjust various physical models like the minority carrier mobility, intrinsic carrier density and recombination mechanisms (i.e. Shockley-Read-Hall (SRH), Auger and surface recombination at passivated interfaces), among others.

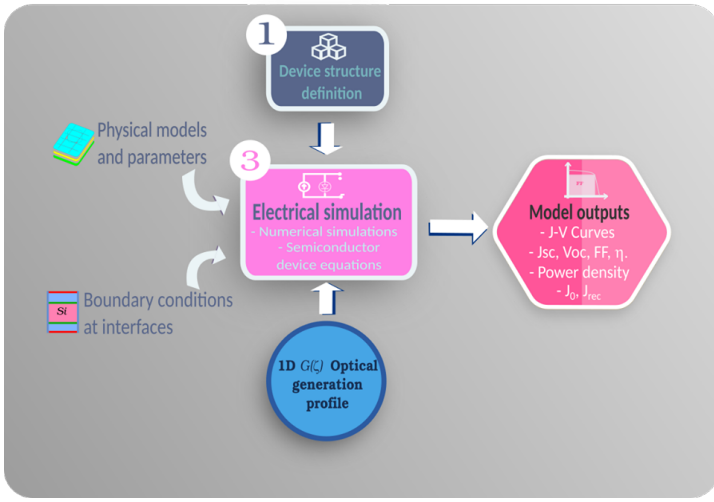

FIGURE 3.13: TCAD Sentaurus-based flow diagram for the electrical simulation of solar cells[45].

3.3.4 Boundary conditions

To properly emulate the simulation domain of the solar cell we have to do some considerations. The boundary conditions need to be carefully specified for the accuracy of the electro-optical simulations. Firstly, in the *electrical simulation*, the boundary condition has to be specified at the edges of the solar cell where the rear metal-contacts are placed, in order to model the conditions in which the cell device has to be evaluated (i.e. different voltages to build *J-V* curve). In this analysis, current and charges are assumed to be symmetrical, so, there is no charge crossing from one symmetry element to another. On the other hand, the electrical rear metal-contacts can be either ohmic or Schottky contact, while series and parallel resistances are considered extern to the TCAD-based simulations [45].

Secondly, in the *optical simulation*, the boundaries between symmetry elements need to be set with an appropriate reflectivity to accurately account the behavior of the entire device. Moreover, for emulating the anti-reflective coating (ARC) effects in the front and back surfaces, we have considered the Monte Carlo Raytracing because is an indirect method that determines the total absorption inside the device by obtaining the total reflectance and transmittance without considering the interfaces (see Fig. 3.14) [164].

The angle at which rays are incident on the ARC passes as inputs to the TMM (Transfer Matrix Method) solver, which returns the reflectance, transmittance, and absorbance for both parallel and perpendicular polarizations to the ray tracer. The ray tracer calculates each angle of refraction according to Snell's law, details in-depth are cover in [45].

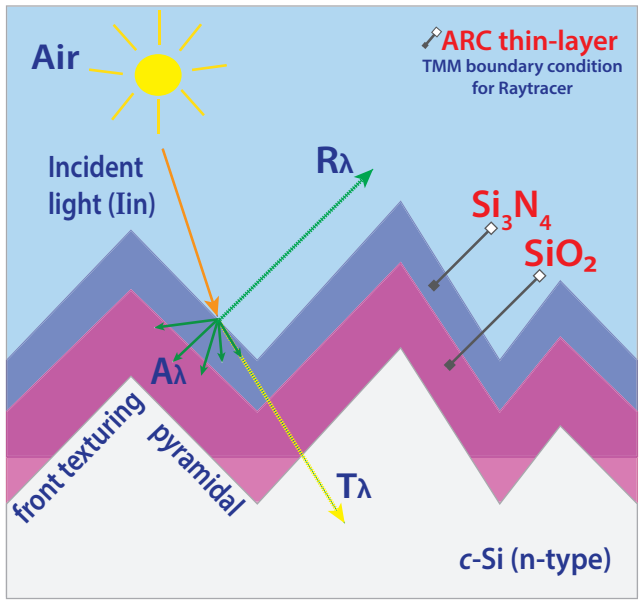

FIGURE 3.14: Sketch of a thin-layer-stack boundary condition for a simulated anti-reflective coating (ARC) layer. Redesigned from [163].

3.4 *c*-Si modeling and parameters

An essential part of the simulations of crystalline silicon *c*-Si solar cells are the input parameters and models, which accurately described the behavior of the device. These common entries to all the performed simulations including the choice of parameterization for modeling silicon properties have been carefully studied and are reported in Table 3.1. It is worth pointing out that models and parameters described are directly related to the Drift-Diffusion transport model.

Moreover, parameters related to the semiconductor material *c*-Si are considered intrinsic, and those related to fabrication process are extrinsic. On the other hand, most of the specified models are implemented by default in the TCAD Sentaurus simulator. Nonetheless, this is not the case of the intrinsic recombination *Radiative and Auger* proposed by Richter et al. [80]. The model was introduced in the simulator using a physical model interface (PMI) which allows adding models to express physical properties.

To validate the implemented model, Fig. 3.15 shows the intrinsic lifetime in a *p*-type substrate τ_{intr} picked-up from the paper and the modeled results from TCAD, with the same characteristics as are defined in it. It can be note that for a Δn range from 10^{10} to 10^{20} cm^{-3} and for a N_{dop} (net dopant concentration) range from 10^{15} to 10^{19} cm^{-3} both are in

very good agreement. Intrinsic physical models are implemented according to the state-of-the-art, while the extrinsic physical models are implemented by calibration or measured parameters.

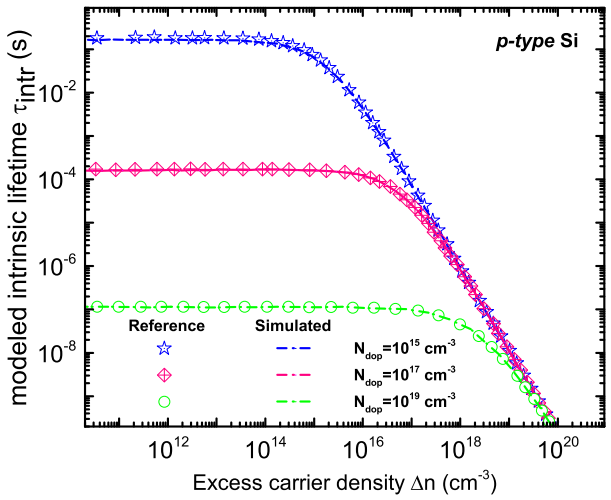

FIGURE 3.15: Validation of the implemented intrinsic lifetime τ_{eff} in Sentaurus TCAD with the data presented in [80]

The surface SRH recombination velocity model, implemented in the phosphorus doped passivated regions, such as the FSF, BSF, and bulk, is based on a more accurate formula to fit the experimental data and it has been proposed by Altermatt et al. [77]. This consist in a very precise semi-empirical parameterization for the surface recombination velocity dependent on doping concentration N_{dop} which uses the Fermi–Dirac statistics, improved models, and parameters for recombination mechanisms, as follows,

$$S_p = S_{p1}\left(\frac{N_{dop}}{N_{p1}}\right)^{\gamma_{p1}} + S_{p2}\left(\frac{N_{dop}}{N_{p2}}\right)^{\gamma_{p2}} \tag{3.6}$$

This model is numerically evaluated in the pre-processing of the simulator, reading the doping parameter at the interface N_{dop} and assigning a value of surface recombination. The parameters in equation (3.6) are all dependent on the doping concentration, passivation material and geometry of the surface which can be planar or textured. The fitting of measured data with the modeling curves is depicted in Fig. 3.16. Note that the textured surfaces cause larger *surface recombination velocities* due to the increment of defect density N_{sT} on the surface of a textured wafer, as evidenced in [77]. Also, it is partially attributed to the bigger area of the textured surfaces as compared to planar surfaces.

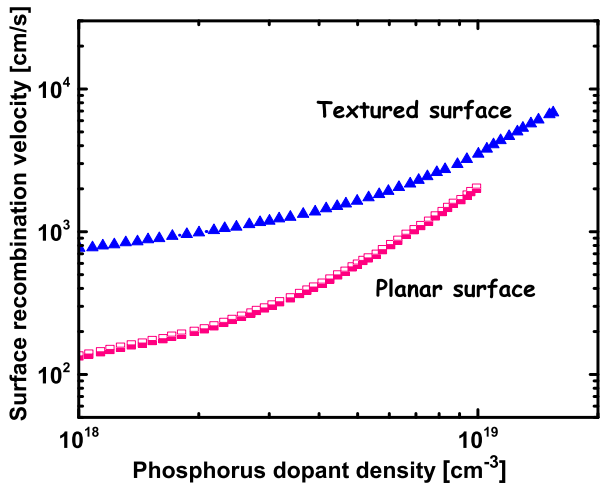

FIGURE 3.16: Surface recombination velocity as a function of the doping level at passivated n^+-silicon textured and planar surfaces, denoted by the blue triangles and pink boxes, respectively. Both lines are parameterization of equation (3.6). Taken from [77].

Moreover, the values of these parameters for some experimental data set corresponding to different surface passivation conditions are described in Table I of [77]. According to equation (3.6) Altermatt et al. states that the surface recombination velocity increases more progressively at low than at high surface doping concentrations. On the other hand, the values of surface recombination velocity for the boron doped region also known as emitter, are reported in [165]. In addition, the considered intrinsic lifetime for all simulations in a *n*-type silicon wafer was set to 2 ms [166] and the temperature for the simulations is set to 300 K.

Device simulation	
Equations numerically solved	Semiconductor equations [167]
Temperature	300 K
Free carrier statistics	Fermi-Dirac [147]
Band gap narrowing	Schenk [168]
Free carrier mobility	Klaassen's unified mobility model [169]
Intrinsic carrier density	Misiakos, Altermatt [170, 171] (ni =9.65 $\times$ 10^9 cm^{-3} at 300 K)
Intrinsic recombination: Auger and radiative	Semi-empirical models by Richter et al. [80]
Metal/Silicon interface recombination velocity	$S_n = S_p = 1{\times}10^7$ cm/s (thermal velocity) [147]
SRH lifetime	Scharfetter relation (by default in Sentaurus TCAD) [166] (τ_{max} = 2 ms for bulk lifetime)
Surface recombination velocity (SRV) at passivated interfaces	Semi-empirical model for Phosphorous- and Boron-doped regions by Altermatt et al. [77, 165]
Specific contact resistance (ρ_c)	emitter (p-contact): $\rho_{c,em} = 3.90 \times 10^{-3}$ $\Omega{\cdot}cm^2$ BSF (n-contact): $\rho_{c,BSF} = 2.20 \times 10^{-3}$ $\Omega{\cdot}cm^2$ [36, 147]
Aluminum resitivity (ρ_{al})	$\rho_{al} = 2.65 \times 10^{-6}$ $\Omega{\cdot}$cm [172]
Optical simulation	
Solar spectrum	Air Mass 1.5 Global Spectrum (AM1.5G - 1000 W/m^2) [150]
Optical properties *c*-Si	Green [173]
ARC layers	[174, 175]
Monte Carlo Raytracing technique combined with Transfer Matrix Method (TMM)	[45, 155, 176]

TABLE 3.1: Summary of the relevant physical models and parameters used in the electro-optical modeling of *c*-Si solar cells.

Chapter 4

Point Contact BC-BJ solar cell

In this chapter, the performance of the simulated three-dimensional back contact-back junction (BC-BJ) crystalline silicon (*c*-Si) solar cell will be analyzed with respect to the impact of the adoption of a rear *point contact* (PC) pattern. Moreover, a comparison of four different BC-BJ rear contact schemes will be examined. Basically, the analyzed point contact solar cell is compared with a conventional BC-BJ solar cell featuring a linear-contact (LC) pattern at the rear side. Furthermore, both architectures were evaluated by varying the contact fraction (CF) at the rear side of the cell. The trends in the related figures of merit will be detailed and explained, providing useful insight for a better understanding of the implemented design process.

4.1 Overview of Point Contact scheme

As it was exposed in section 2.10.3 an alternative to improve the conventional two-sided contacted *c*-Si solar cell is the implementation of the *interdigitated back contact* (IBC) cells [116]. This solar cell architecture also known as *back contact-back junction solar cell* (BC-BJ) has both collecting diffused regions, i.e. back surface field (BSF) and emitter, as well as the electrodes, positioned on the rear side of the silicon substrate, as illustrated in Fig. 4.1 [30, 117]. Back contact-back junction (BC-BJ) solar cells based on crystalline silicon (*c*-Si) technology represent an evolution of conventional solar cells and a valuable concept to reach higher conversion efficiency both in heterojunction [37] and homojunction [36] structures. Among several advantages of BC-BJ solar cells over front contact-front junction (FC-FJ) architectures, it is worth mentioning the absence of optical shading losses at the front side leading to higher current density, and the simplified module-interconnection process since both electrodes are at the rear side. However, a high minority-carrier bulk lifetime and a high-quality front and rear surface passivation are just some of the main issues that BC-BJ architectures have to face for optimizing their performance [36, 177].

Moreover, several works show that an optimum design of the cell geometry and the doping profiles is fundamental to boost the efficiency of BC-BJ solar cells [160, 178–185]. In

particular, the optimization of the rear metallization in terms of choice of contact materials, formation process and geometric pattern plays a crucial role to achieve a good trade-off among electrical shading effects [186], recombination losses occurring at rear interfaces and series resistance losses related to current paths, contact and metal resistance. Thereby, the metallization process normally is one of the most critical and costly steps in the manufacturing process of solar cells [187].

Regarding this, the development of alternative low-cost, high-efficiency printing techniques to replace the expensive clean room metallization processes is one of the most important achievements in the photovoltaic industry [188]. As a matter of fact, screen-printing is the most widely used technique in large-area BC-BJ solar cells featuring the typical metallization pattern with interdigitated linear contact fingers [189–191]. However, the adoption of more complex metallization schemes including a *point contact* (PC) pattern at the rear side can further enhance the solar cell performance, as already demonstrated for both FC-FJ [192–196] and BC-BJ [36, 119, 177–180] cell architectures due to the considerable reduction of recombination losses at defective metal/c-Si interfaces.

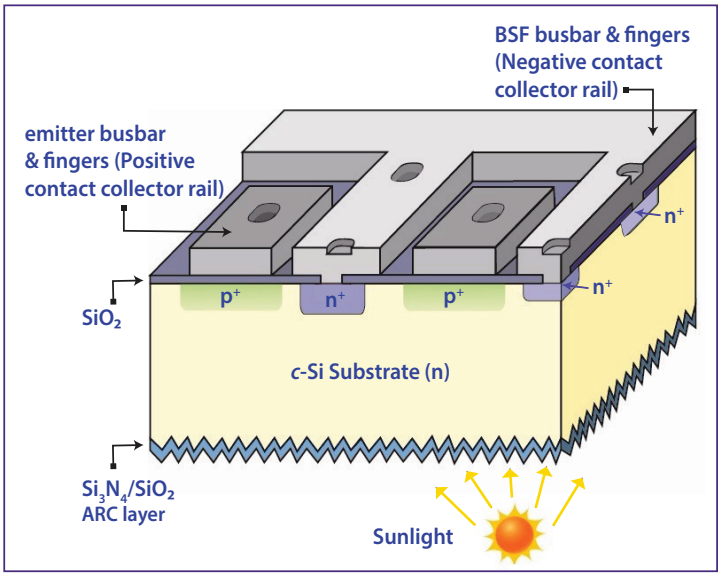

FIGURE 4.1: View of a 3D BC-BJ Point contact solar cell. All contacts are placed on the rear side of the structure and can thus be made as thick as desired. Redesigned from [197].

In general, PC scheme rather than having alternating n and p full metallized fingers, it consists of an array of distributed metal points that contact the substrate only via small

openings, typically realized by laser processing [179, 198]. And as stated before, a remarkable feature of this solar cell pattern is that both electrical contacts (i.e., positive and negative contacts) are placed on the backside of the cell structure and thereby no shading effect occurs [38, 116]. The PC architecture is schematically represented in Fig. 4.1. Therefore, a proper design of a rear PC pattern allows one to balance the trade-off between the reduced recombination losses (due to the increase of the rear passivated non-contacted interface area) and the increased series resistance losses (due to the increase of the current crowding effects and contact resistance at the rear side), thus potentially leading to higher conversion efficiency [194].

4.2 Simulation setup

In this section is described the setup of simulations to evaluate the impact of a rear PC scheme in the performance of a *c*-Si back-contact back-homojunction solar cell by means of a three-dimensional (3D) electro-optical device model developed in the state-of-the-art TCAD simulator [45]. Additionally, a comparison of the analyzed point contact solar cell with a conventional BC-BJ solar cell featuring a linear-contact (LC) scheme at the rear side is exposed [159]. Fig. 4.2(a) and (b) include the three-dimensional (3D) sketch and the two dimensional (2D) cross-section, respectively, of the simulated *c*-Si BC-BJ solar cell. Both back surface field (BSF) and emitter regions feature a thick and wide rear metallization that contacts the silicon only via small circular-shaped holes [36]. In particular, the considered PC layout along the *x*-axis has a single point contact in the BSF region and four uniformly-distributed point contacts in the emitter region to minimize the resistive losses related to current paths and then to maximize the conversion efficiency, according to [159].

As discussed in [194, 195], the adoption of a rigorous full 3D modeling approach is mandatory when dealing with a PC geometry to accurately include in the numerical simulations the 3D effects of several competing physical mechanisms, e.g., the current crowding effects occurring at point contacts and the carrier lateral transport. On the other hand, 3D numerical simulations typically demand an additional effort in the construction of the mesh grid to reach a suitable trade-off between the computational cost and the simulation accuracy. Exploiting the symmetry of the PC solar cell, the 3D simulation domain used in the electrical simulations can be limited to the smallest periodic 3D structure, which is representative of the whole device. As shown in Fig. 4.3, the lateral size (W_x) of the considered 3D simulation domain along the *x*-axis is half of the rear pitch, while the depth (W_z) is half of the point contacts pitch along the *z*-axis (d_z), i.e. the distance between the centers of two adjacent point contacts along the same axis. The point contacts pitch along the *x*-axis (d_x) is given by [159],

$$d_x = \frac{W_{em}}{N_{c,em}} \tag{4.1}$$

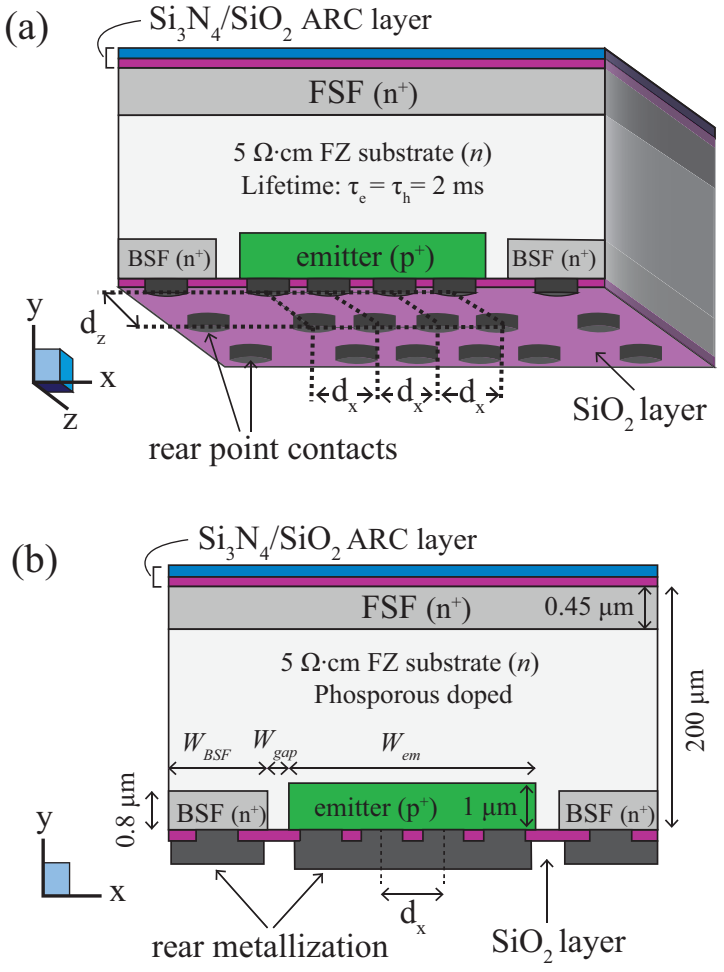

FIGURE 4.2: (a) Three-dimensional (3D) sketch and (b) corresponding two-dimensional (2D) cross-section of the simulated point-contact (PC) BC-BJ solar cell (both pictures are not in scale and the bottom metallization underneath the point contacts is omitted in the 3D sketch to highlight the PC layout).

where W_{em} is the width of the emitter region and $N_{c,em}$ is the number of contacts along the *x*-axis in the emitter region (i.e., 4 in our case). For the sake of symmetry, we use the same pitch along the *z*-axis for the point contacts in the BSF region, where the single point contact is right in the middle of the *x*-axis, as depicted in Fig. 4.3. The height of the 3D simulation domain along the *y*-axis is equal to the substrate thickness. This setup allows limiting the run-time for light *J-V* simulations to about 2 hours by using an optimized 3D mesh grid with about 150,000 nodes on a 8-core 16-GB 3.40-GHz Intel i7-3770 processor.

As shown in Fig. 4.2, the developed geometrical model includes a 200 μm-thick, 5 Ω·cm resistivity float-zone (FZ) *c*-Si *n*-type substrate. Front side is covered by a double Si_3N_4/SiO_2 anti-reflective coating (ARC) layer and features a front surface field (FSF) modeled by a Gaussian function with a surface peak doping concentration (C_{peak}) of 3.5×10^{18} cm^{-3} and a junction depth (J_{depth}) of 0.45 μm [159]. The rear side is passivated by a SiO_2 thin layer. The BSF and emitter doping profiles are also modeled by Gaussian functions featuring a C_{peak} of 1.70×10^{20} cm^{-3} and 5×10^{19} cm^{-3}, and a J_{depth} of 0.8 μm and 1 μm, respectively [159]. It is worth mentioning that in this thesis all the used doping profile typology in the simulation setup are Gaussian functions. The emitter-BSF spacing gap (W_{gap}) at the rear side is 1 μm, while the BSF width (W_{BSF}) and W_{em} are set to 60 μm and 300 μm [159], respectively, thus leading to a rear pitch of 362 μm.

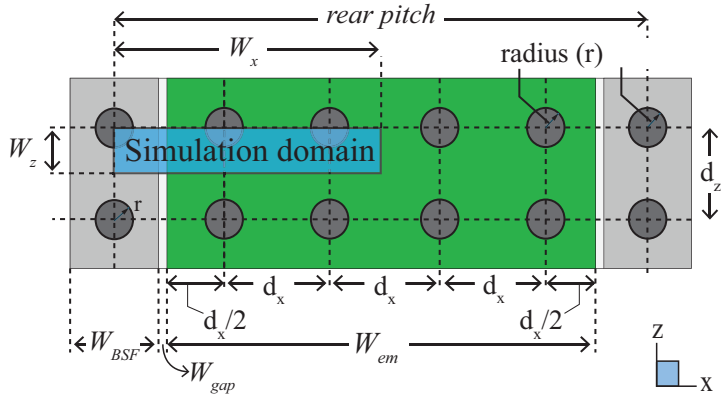

FIGURE 4.3: Bottom view of the rear side with the considered simulation domain for the simulated point-contact (PC) BC-BJ solar cell (here the rear SiO_2 layer and the bottom metallization underneath the point contacts are omitted).

Electrical simulations were performed by exploiting the well-known drift-diffusion model. To accurately model highly doped regions in the simulated solar cell, we enabled Fermi-Dirac statistics in the simulations. Moreover, as suggested in [43], we made an *ad-hoc* refinement of several physical models and parameters implemented in the TCAD simulator to achieve more realistic predictions on the performance of the considered solar cells.

This calibration procedure was carried out by taking into account more recent parameterizations proposed in literature [44, 147]. In particular, the bulk minority carrier lifetime was set to about 2 ms according to the substrate doping, while the surface recombination velocity (SRV) at rear passivated BSF and emitter interfaces was set to about 10^5 and 10^3 cm/s, respectively, according to the surface peak doping concentration of BSF and emitter doping profiles.

Finally, the losses due to the parasitic series resistance associated to the rear contact resistance were directly accounted in the outcomes of electrical simulations by setting in the simulated device the contact resistivity (ρ_c) at BSF ($\rho_{c,BSF}$) and emitter metal/silicon interfaces ($\rho_{c,em}$) to 2.20×10^{-3} $\Omega\cdot$cm^2 and 3.90×10^{-3} $\Omega\cdot$cm^2 [159], respectively. Concerning the optical modeling, the 3D map of the optical generation within the simulated device was built by interpolating on the 3D mesh grid, used as input for the electrical simulation, two different one-dimensional (1D) profiles of the optical generation rate in correspondence to rear passivated and contacted interfaces, respectively. The 1D optical profiles were extracted from 3D optical simulations, accounting for a texturized front interface with regular pyramids featuring a 10 μm base and a 54.7° base angle, and a planar rear interface with a different bottom internal reflectivity at SiO_2-passivated and contacted surfaces, respectively [160].

In particular, optical simulations were performed at 1-sun illumination condition (i.e., assuming direct illumination with a standard AM1.5G 1000 W/m^2 solar spectrum) by using the Monte Carlo ray tracing technique [155, 176] combined with the Transfer Matrix Method (TMM) to correctly model the interference mechanisms occurring at the front ARC and the rear thin oxide layer [175]. Similarly to the electrical model, we made an accurate calibration of the parameters included in the optical model. More specifically, the optical properties of silicon and ARC layers were set according to [173] and [174], respectively.

4.3 Comparison of the impact of the point contact (PC) and linear contact (LC) schemes in the BC-BJ solar cell

The impact of the adoption of the PC scheme in the considered BC-BJ solar cell was evaluated by varying the rear contact fraction (*CF*), i.e. the ratio of the contacted area (A_c) to the total cell area (A_{TOT}) at the rear side. The *CF* was changed by varying the radius (r) of the circular point contacts while keeping constant the point contacts pitch. In particular, we considered that the point contacts are uniformly distributed in the emitter region, i.e. the PC layout features the same pitch along x- and z-axis (i.e. $d_x = d_z = d$), as shown in Fig. 4.4(a). It is worth pointing out that, from our simulation results, we observed that such a pattern maximizes the efficiency of the PC solar cell due to the proper distribution of the

carrier collecting paths inside the device. Therefore, according to Fig. 4.4(a), the *CF* of the simulated PC solar cell is expressed as follows

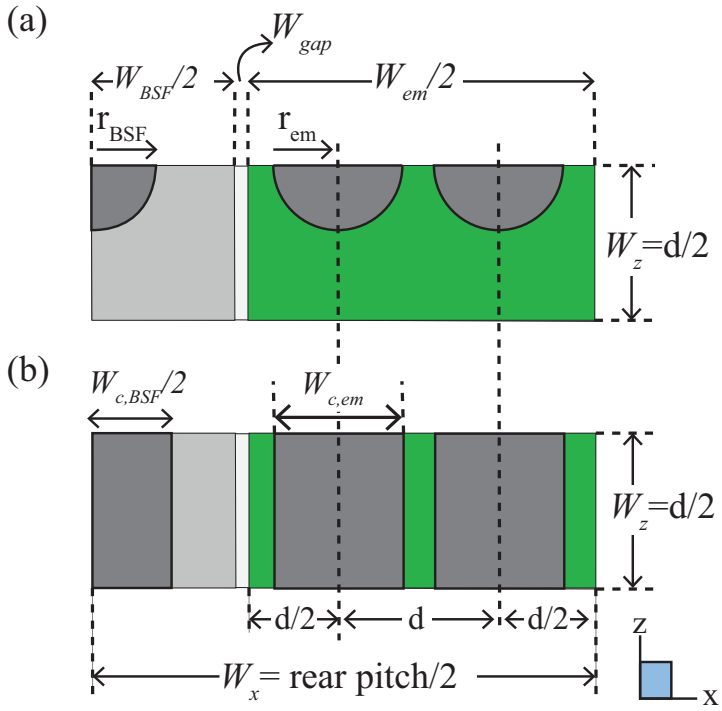

FIGURE 4.4: Bottom view of the considered simulation domain for (a) the point-contact (PC) and (b) the linear-contact (LC) BC-BJ solar cell. The rear SiO_2 layer and the bottom metallization underneath the point contacts are omitted.

$$CF_{PC} = \frac{A_c}{A_{TOT}} = \frac{A_{c,BSF} + A_{c,em}}{A_{TOT}} = \\ = \frac{\left(\frac{\pi \cdot r_{BSF}^2}{4}\right) + \pi \cdot r_{em}^2}{\left(\frac{W_{BSF}}{2} + W_{gap} + \frac{W_{em}}{2}\right) \cdot \frac{d}{2}} \tag{4.2}$$

where r_{BSF} and r_{em} represent the radius of point contacts in the BSF and emitter region, respectively.

The simulated PC BC-BJ solar cell was compared to a corresponding conventional BC-BJ solar cell, i.e. featuring a LC scheme with a single contact line in the BSF region and four contact lines equidistantly distributed in the emitter region [159]. The three-dimensional linear contact (LC) structure is schematically represented in Fig. 4.5(a), with its corresponding simulation domain in Fig. 4.5(b). In this case, the *CF* was changed by varying the width of contact lines while keeping constant the pitch (*d*) along the *x*-axis in the emitter region. Therefore, according to Fig. 4.4(b), the *CF* of the simulated LC solar cell is defined by

$$CF_{LC} = \frac{A_c}{A_{TOT}} = \frac{A_{c,BSF} + A_{c,em}}{A_{TOT}} = \\ = \frac{\frac{W_{c,BSF}}{2} + 2 \cdot W_{c,em}}{\left(\frac{W_{BSF}}{2} + W_{gap} + \frac{W_{em}}{2}\right)} \tag{4.3}$$

where $W_{c,BSF}$ and $W_{c,em}$ represent the width of linear contacts in the BSF and emitter region, respectively.

It is worth noting that simulation results of the LC solar cell also account for the series resistance losses due to the metal fingers, considering a finger thickness (T_f) of 2 μm, a finger length (L_f) of 1.5 cm and a metal resistivity (ρ_m) of 2.65×10^{-6} Ω·cm [159], whereas the contribution of these losses is quite negligible in the simulated PC solar cell due to the relatively thicker and wider rear metallization (see Fig. 4.2(b)). Accordingly, the series resistance losses in the LC solar cell include both contact interface resistance (r_c) and metal finger resistance (r_m) contributions, modeled with a distributed resistance in Ω·cm^2 [199], as follows,

$$r_l = r_c + r_m \tag{4.4}$$

It is noteworthy that these resistance contributions are weighted along the active cell area. In particular, the analysis regarding the estimated resistance due to the metal fingers is exhibited in the schematic of Fig. 4.6 and it is described by the following integral,

$$r_{m,est} = \frac{1}{L_f} \int_0^{L_f} \rho_m \frac{L_f - x}{W_c \cdot T_f} dx \tag{4.5}$$

where ρ_m represents the metal (aluminum) resistivity. Solving the integral we obtained the next expression,

$$r_{m,est} = \frac{\rho_m}{L_f \cdot W_c \cdot T_f} \frac{L_f^2}{2} \tag{4.6}$$

Subsequently, the analysis considers the area of the metal contact with the semiconductor material, defined by,

$$A_c = W_c \cdot L_f \tag{4.7}$$

Thus, the weighted resistance contribution of each metal finger is determined by,

$$r_{m,est} = \frac{\rho_m}{L_f \cdot W_c \cdot T_f} \frac{L_f^2}{2} \cdot W_c \cdot L_f \tag{4.8}$$

Hence, according to [200], r_l along the *BSF* and *emitter* regions can be written as,

$$r_{l,BSF} = \frac{\rho_m \cdot L_f^2}{2 \cdot T_f \cdot 1 \times 10^{-4}} + \rho_{c,BSF} \tag{4.9}$$

$$r_{l,em} = \left(\frac{\rho_m \cdot L_f^2}{2 \cdot T_f \cdot 1 \times 10^{-4}} \cdot \frac{1}{N_{c,em}} \right) + \rho_{c,em} \tag{4.10}$$

where $N_{c,em}$ is the number of contacts along the *x*-axis in the emitter region, $\rho_{c,BSF}$ and $\rho_{c,em}$ represent the specific contact resistivity in the BSF and emitter regions, respectively, and a conversion factor of $1{\times}10^{-4}$ is required to change the units of T_f (μm) into cm. In the end, as it was mentioned above the distributed resistance is obtained in $\Omega{\cdot}\text{cm}^2$. For both considered cell architectures, two different cases were investigated: the first one refers to the use of contacts of the same size in BSF and emitter regions, while in the second case the size of BSF contacts was kept to a fixed value such as to obtain a highly-contacted BSF region. Therefore, four different rear contact schemes were analyzed as a function of the rear contact fraction (*CF*):

(i) a PC BC-BJ solar cell by varying the contact radius both in the BSF and emitter regions where $r_{BSF} = r_{em}$

(ii) a PC BC-BJ solar cell by varying the contact radius only in the emitter region with a fixed r_{BSF} of 25 μm

(iii) a LC BC-BJ solar cell by varying the contact width both in the BSF and emitter regions where $W_{c,BSF} = W_{c,em}$

(iv) a LC BC-BJ solar cell by varying the contact width only in the emitter region with a fixed $W_{c,BSF}$ of 50 μm.

Note that *d* was set to 75 μm, as given by equation (4.1), in all the structures that feature a W_{em} of 300 μm and a $N_{c,em} = 4$.

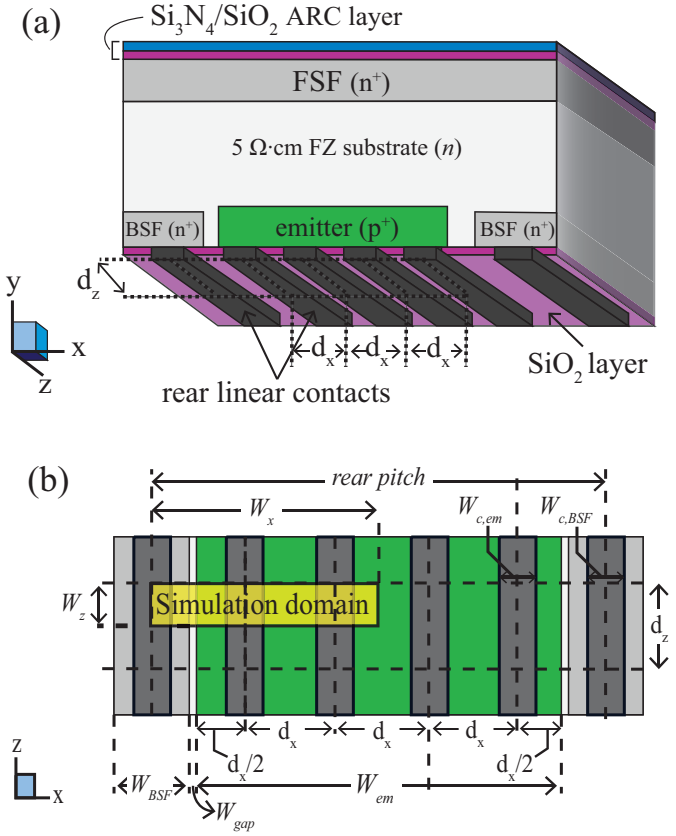

FIGURE 4.5: (a) Three-dimensional (3D) sketch and (b) bottom view of the rear side with the considered simulation domain for the simulated linear-contact (LC) BC-BJ solar cell.

4.4 Simulation results and discussion

With the aim of analyzing the effects of the four different rear point- and linear contact schemes in the conversion efficiency of the simulated BC-BJ solar cell, a set of experiments has been performed by varying the contact sizing (i.e. radius and width, respectively), both in the BSF and emitter regions; and also by keeping constant the contact size in the BSF region while it varies only in the emitter region.

Fig. 4.7 reports the results in terms of the principal solar cell figures-of-merit (FOMs), such as open circuit voltage (V_{oc}), short circuit current density (J_{sc}), fill factor (*FF*) and conversion efficiency (η), as a function of the rear *CF* for all the simulated solar cells. As expected, both V_{oc} and J_{sc} decrease when increasing the rear contacted area, as illustrated

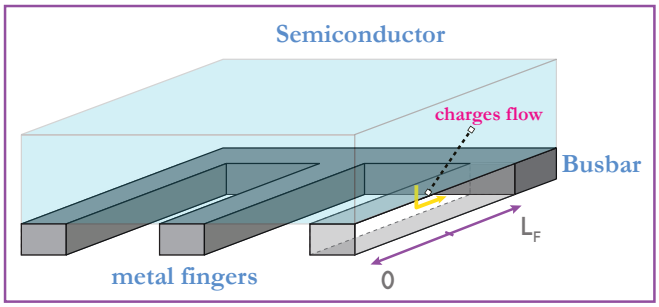

FIGURE 4.6: Schematic in 3D of the simulated linear-contact (LC) BC-BJ solar cell featuring rear metallization.

in Fig. 4.7(a) and (b), this is due to the increase of the surface recombination losses, whereas *FF* exhibits an opposite trend with the *CF*, as shown in Fig. 4.7(c), due to the reduction of the series resistance losses including both the contributions related to the rear metal contacts and the lateral carrier transport within the device, respectively.

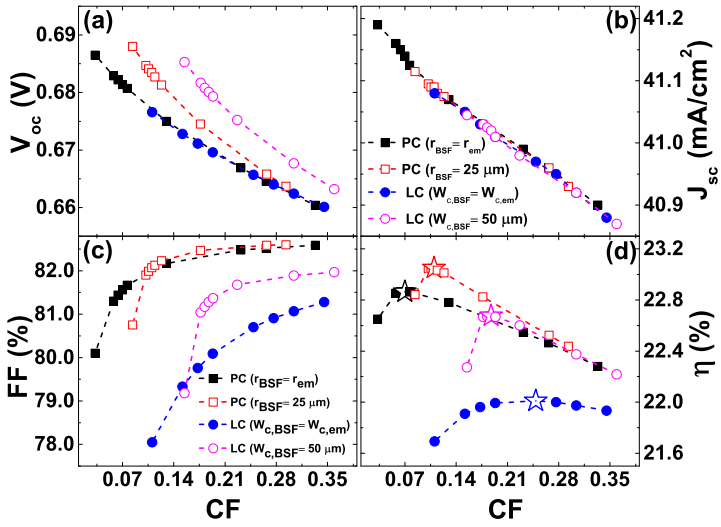

FIGURE 4.7: FOMs, such as (a) V_{oc}, (b) J_{sc}, (c) FF and (d) η, as a function of the rear contact fraction (*CF*) for the different PC and LC structures.

As a consequence, all efficiency curves in Fig. 4.7(d) show a bell shape with a maximum value (η_{max}) corresponding to an optimum *CF* (CF_{opt}), which changes in the different simulated cell structures. We can also observe that, at the same *CF*, the different solar cells show a similar J_{sc} (see Fig. 4.7(b)), while V_{oc} is slightly larger in the cells with the highly-contacted BSF region (see Fig. 4.7(a)). This is due to the fact that, at a specific *CF*, these cell

structures have a smaller contacted area and hence a larger passivated area in the emitter region, where the SRV at SiO_2/silicon interface is smaller than the BSF region due to the lowly-doped profile, as already described in section 4.2. Accordingly, the cell structures with the highly-contacted BSF region feature a smaller effective rear SRV and thus lower surface recombination losses at the rear side with respect to the cells with the same contact size in BSF and emitter regions, thus leading to higher V_{oc}.

As reported in Fig. 4.7(c), when compared to the corresponding cell structures with the same contact size in BSF and emitter regions, both the PC and LC solar cells with higher contact size in the BSF show higher *FF* at high *CF* because of the reduction of the series resistance losses related to the lateral carrier transport, and lower *FF* at low *CF* due to the increase of the series resistance losses related to the smaller metal contacts in the emitter region. Moreover, Fig. 4.7(c) shows that LC solar cells exhibit lower *FF* than PC structures because of the contribution of the metal finger resistance, which is quite negligible in the PC cells, as stated above.

Therefore, according to Fig. 4.7(d), the results of our analysis on the simulated BC-BJ solar cells, featuring a narrower highly-doped BSF and a wider lowly-doped emitter, demonstrate that (i) a highly-contacted BSF region is convenient both in PC and LC cell structures, and (ii) the adoption of a thick and wide rear metallization contacting the silicon only via small holes allows boosting the cell efficiency. In particular, as illustrated in Fig. 4.7(d), the PC solar cell with the highly-contacted BSF shows a η_{max} of 23.05% at a CF_{opt} of 11%. This corresponds to an efficiency improvement of about $0.2\%_{abs}$ with respect to the PC cell with the same contact size in BSF and emitter, and of about $0.37\%_{abs}$ with respect to the LC cell with the highly-contacted BSF, mainly due to the higher V_{oc} (see Fig. 4.7(a)) and to the higher *FF* (see Fig. 4.7(c)), respectively.

Besides light *J-V* simulations, we also performed dark *J-V* simulations to better explain the observed FOMs trends in the considered solar cells [201–205]. The performed dark analysis is based on the assumption that the solar cell can be described with a standard two-diode equivalent model, as follows,

$$J(V) = J_{01}\left[exp\left(\frac{q(V-J(V)R_s)}{n_1 kT}\right)-1\right] + J_{02}\left[exp\left(\frac{q(V-J(V)R_s)}{n_2 kT}\right)-1\right] + \frac{V-J(V)R_s}{R_{sh}} \tag{4.11}$$

where J_{01} and J_{02} are the dark saturation current densities of the two diodes, respectively. Meanwhile, $n1$ and $n2$ are the ideality factors of the two diodes, and R_s and R_{sh} denote the series and the shunt resistances, respectively.

In this regard, Fig. 4.8 illustrates the R_s and the J_0 extracted from dark *J-V* curves as a function of the rear *CF* for the PC solar cell with the highly-contacted BSF. According to the

above results, two opposite trends are observed as *CF* increases: J_0 linearly rises due to the increase of recombination losses at metal/silicon rear interfaces, while R_s drops because of the reduction of the contact resistance and spreading resistance contributions.

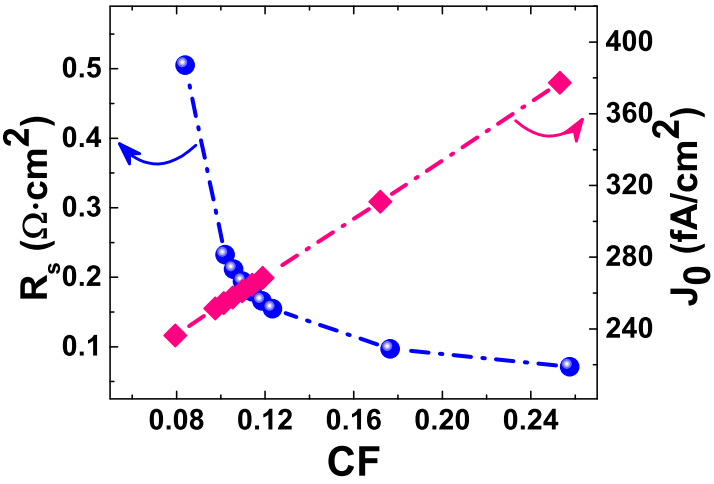

FIGURE 4.8: Series resistance (R_s) and total dark saturation current density (J_0) as a function of the rear contact fraction (*CF*) for the point-contact (PC) solar cell.

Additionally, Fig. 4.9 reports the plot of the extracted shunt resistance (R_{sh}) as a function of the rear contact fraction (*CF*) for the simulated BC-BJ PC solar cell, featuring a highly-contacted BSF region. According to the obtained results, R_{sh} exhibits extremely high values (i.e., in the order of 10^8 $\Omega{\cdot}\text{cm}^2$) and therefore its impact on the point-contact *PC* solar cell performance is negligible.

4.5 Conclusions

In this chapter, it has been presented a detailed analysis of mechanisms working on the introduction of a point contact (PC) scheme on the backside of the BC-BJ solar cell structure and how this pattern impacts the cell performance. The analysis was performed by using a full 3D electro-optical device model implemented on a state-of-the-art TCAD simulator. In particular, the performance of a BC-BJ solar cell with a PC scheme was evaluated as a function of the rear contact fraction (*CF*) and compared with a corresponding conventional BC-BJ solar cell featuring a linear-contact (*LC*) layout at the rear side of the structure. As a result of the analysis, the simulations show that the adoption of a thick and wide rear metallization contacting the silicon only via small circular-shaped holes both in BSF and emitter regions allows an efficiency improvement of about $0.37\%_{abs}$ with respect to the LC

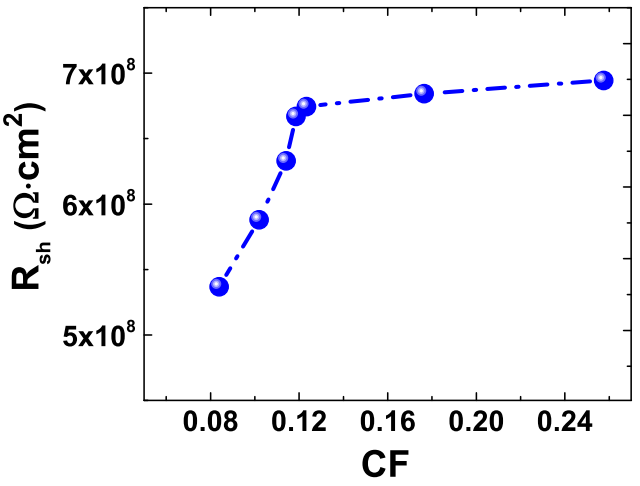

FIGURE 4.9: Shunt resistance (R_{sh}) as a function of the rear contact fraction (*CF*) for the point-contact (PC) solar cell.

cell mainly due to the reduction of series resistance losses related to the metal finger resistance, which is almost negligible in the considered PC structure. It is worth highlighting that in the case of a conventional (front contact) solar cell the typical peak conversion efficiency achieved is reported around to 18% - 19% [206].

It has been demonstrated that a typical screen-printed solar cell featuring a uniformly contacted back surface such as the linear-contact layout, is significantly affected by high recombination losses at the rear side of the device. Thereby, the realization of a rear point contact scheme is a potential strategy to enhance the performance of crystalline silicon (*c*-Si) solar cells. This alternative is normally implemented in advanced high-efficiency PERL (Passivated Emitter Rear Locally diffused) and PERC (Passivated Emitter Rear Cell) solar cells [115, 195, 207] due to its capacity of minimizing the effective rear surface recombination velocity because of the passivation techniques applied on the non-contacted regions. Moreover, the rear passivating layers lead to enhance the effective internal bottom reflectivity due to the larger reflectivity of silicon-dielectric-metal stack interface with regards to the silicon-metal one [208, 209].

Chapter 5

Point Contact BC-BJ solar cell with Selective Emitter

In this chapter, the performance of the 3D simulated BC-BJ *c*-Si point contact solar cell will be analyzed regarding to the effect of the introduction of an optimized selective emitter (SE) design with a local highly-doped (HDOP) profile underneath rear point contacts and a narrower lowly-doped (LDOP) profile at the non-contacted rear interfaces. The behavior of the simulated PC solar cell with a SE design and the resulting trends of the output parameters will be detailed and explained, providing information about the best simulation design guidelines to enhance the efficiency.

5.1 Overview of selective emitter (SE) solar cell

The selective emitter *SE* design is a promising alternative to enhance the performance of the emitter region. In particular, SE solar cell regarding conventional screen-printed industrial *c*-Si cells based on an homogeneously diffused emitter (HE), implements different doping profiles in the metallized and non-metallized regions. Accordingly, the SE technique features a local highly-doped (HDOP) profile under the rear metal-contacted regions and a lowly-doped (LDOP) profile at the non-contacted rear interfaces. This process allows optimizing the HDOP and LDOP emitters independently, contributing significantly to the improvement of the performance of novel *c*-Si solar cells.

The benefits of heavy doping beneath the metal contacts are mainly focused on the reduction of the contact resistance between the metal-silicon interface and in the capability of shielding the high surface recombination velocity metal-silicon interface from the active regions of the cell [210]. The SE is one of the most interesting industrial low-cost concepts used to boost the efficiency of FC-FJ *c*-Si solar cells without a relevant increase in production costs [211, 212] and it is also suitable for back contact solar cells [178, 213]. The Selective emitter contributes significantly to the high performance levels reported by novel solar cell technologies. Finally, selective emitter process ensures a good ohmic metal-silicon contact

(i.e., achieving a low contact resistance) by applying a heavy doping beneath rear point contacts. This technique is an alternative to mitigates the effect of the surface recombination at the metal-silicon interfaces because the contacted-regions can not be passivated by introducing a silicon dioxide layer.

5.2 Simulation setup

In this analysis, the three-dimensional simulation approach follows the same methodology considered in the electro-optical modeling for the simulated point contact (PC) BC-BJ solar cell described in section 4.2. Thus, the element of symmetry of the simulated PC layout with a selective emitter is also represented in Fig. 4.2(b). Since the defined structure of the PC BC-BJ solar cell is highly symmetric, the 3D simulation domain used in the electrical simulations can be reduced to a small periodic 3D structure, which represents the entire device. Fig. 5.1 includes a sketch of a two-dimensional (2D) bottom view of the backside with the considered simulation domain for the simulated point-contact (PC) solar cell with a local highly-doped (HDOP) profile beneath rear point-contacts, represented by the red circle around metal point-contacts.

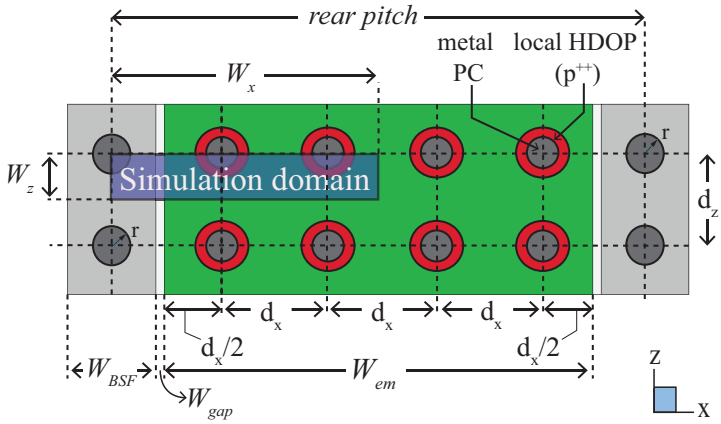

FIGURE 5.1: Two-dimensional (2D) bottom view of the rear side of the simulated point-contact (PC) BC-BJ solar cell featuring a selective emitter design, represented by the red circle around metal point-contacts. The simulation domain is highlighted in blue.

It is worth pointing out that, our simulations considered a uniform distribution of the metal point-contacts in the emitter region, i.e. the PC scheme features the same pitch along x- and z-axis. Thus, $d_x = d_z = d$, where $\boldsymbol{d}$ is calculated by the equation (4.1) and represents the distance between the centers of two adjacent point contacts along the same axis, as depicted in Fig. 5.1.

5.3 Impact of the selective emitter design in the point contact solar cell

With the aim of investigating the impact of the selective emitter (*SE*) designs in the considered BC-BJ solar cell with a point contact (*PC*) scheme at the rear side, an extensive analysis has been performed by evaluating various emitter doping profiles. In contrast with the PC solar cell based on an homogeneously-doped emitter (HE) of Fig. 4.2, the PC-SE cell features different doping profiles in the contacted and non-contacted emitter regions, i.e., a local deeper highly-doped (HDOP) profile underneath rear point contacts and a narrower lowly-doped (LDOP) profile at the passivated interfaces between the point contacts, respectively, as shown in Fig. 5.2.

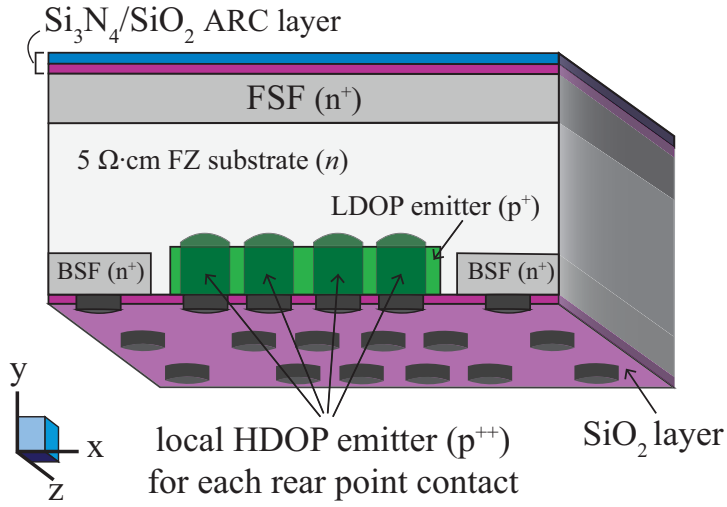

FIGURE 5.2: Three-dimensional (3D) sketch (not in scale) of the simulated point-contact (PC) solar cell with a selective emitter (SE) design at the rear side with highly-doped (HDOP) metal-contacted regions underneath the point contacts and lowly-doped (LDOP) passivated regions between the point contacts.

As reported in Table. 5.1, we investigated two PC-SE solar cells featuring the same HDOP profile (i.e., C_{peak} of 1×10^{20} cm^{-3} and J_{depth} of 1.5 μm) and different LDOP profiles with a C_{peak} of 5×10^{19} cm^{-3} and 1×10^{19} cm^{-3} at the same J_{depth} of 1 μm.

PC-HE solar cell	
C_{peak} (cm^{-3})	J_{depth} (μm)
5×10^{19}	1.0

PC-SE solar cells			
LDOP		**HDOP**	
C_{peak} (cm^{-3})	J_{depth} (μm)	C_{peak} (cm^{-3})	J_{depth} (μm)
5×10^{19}	1.0	2*1$\times10^{20}$	2*1.5
1×10^{19}	1.0		

TABLE 5.1: Parameters of the emitter doping profiles used in the simulated PC-HE (homogeneous emitter) and PC-SE (selective emitter) solar cells.

5.3.1 Simulation results and discussion

In this section, we firstly present and discuss the obtained results of the performed analysis on the influence of the selective emitter designs on the main solar cell figures-of-merit (FOMs). Accordingly, Fig. 5.3 reports the FOMs as a function of rear *CF* for the simulated PC-SE solar cells in comparison with the PC-HE cell presented in chapter 4. As shown in Fig. 5.3(a), the use of the SE is particularly beneficial in terms of V_{oc}, due to the reduction of recombination losses in the emitter regions. Such a reduction can be ascribed to different contributions.

One of these contributions is related to the decrease of surface recombination losses at the contacted emitter interfaces due to the more effective shielding effect of the minority carriers from the metal-silicon interfaces when using a deeper HDOP profile underneath the point contacts. This explains the higher V_{oc} observed at the same *CF* in the PC-SE cell featuring a LDOP profile equal to the emitter profile of the PC-HE cell. As a matter of fact, this V_{oc} increase is more evident when increasing the *CF*, as illustrated in Fig. 5.3(a). Moreover, a further increase of V_{oc} is observed in the PC-SE solar cell featuring the LDOP profile with the lower C_{peak} due to the decrease of both Auger and surface recombination losses in the non-contacted emitter regions.

However, at the same *CF*, this PC-SE cell exhibits a slight reduction of *FF* ascribed to the increased emitter sheet resistance (see Fig. 5.3(c)). Therefore, according to Fig. 5.3(d), the results of our analysis demonstrate that a proper co-optimization of the doping profiles in the LDOP and HDOP emitter regions of the PC-SE solar cell can lead to a further efficiency enhancement as compared to the PC-HE structure. In particular, as shown in Fig. 5.3(d), the PC-SE solar cell featuring the LDOP profile with the lower C_{peak} exhibits a η_{max} of 23.28% at the same CF_{opt} of 11%, thus corresponding to an efficiency improvement

of 0.23%$_{abs}$ with respect to the PC-HE cell.

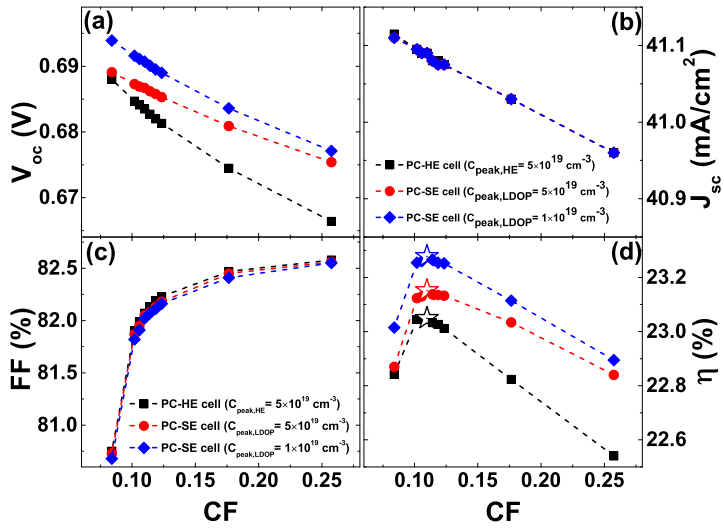

FIGURE 5.3: FOMs, such as (a) V_{oc}, (b) J_{sc}, (c) FF and (d) (η), as a function of the rear contact fraction (CF) for the point-contact (PC) solar cells with homogeneous emitter (HE) and selective emitter (SE) designs at W_{em} = 300 μm.

5.4 Impact of the emitter metallization on the rear geometry of the point contact solar cell

We performed a further analysis by varying the emitter width (W_{em}) and, hence, the rear contact pitch in the simulated PC solar cells, according to equation (4.1). As shown in Fig. 5.3(d), at the same W_{em}, the PC-HE and -SE solar cells exhibit the maximum efficiency at the same CF_{opt}.

5.4.1 Simulation results and discussion

Regarding to this last analysis, Fig. 5.4 reports the CF_{opt} as a function of W_{em}. In particular, we can observe a decreasing trend of CF_{opt} with W_{em}, resulting from the trade-off between the increasing series resistance losses related to the carrier lateral transport inside the device and the decreasing recombination losses.

Such a trade-off also explains the trends observed in Fig. 5.5, where the FOMs at the CF_{opt} as a function of W_{em} are reported for the PC-HE and -SE solar cells. In fact, in all the

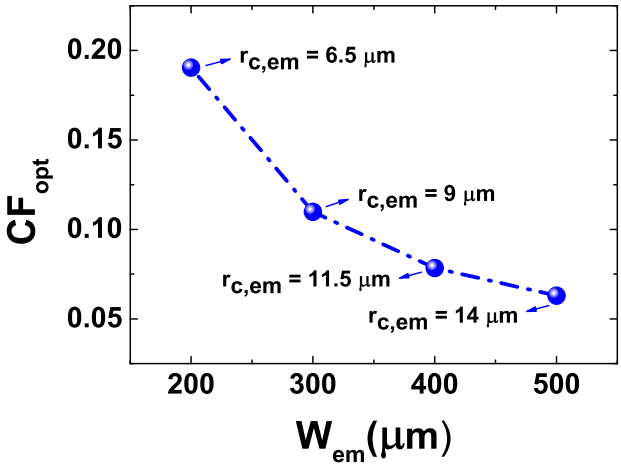

FIGURE 5.4: Optimum rear contact fraction (CF_{opt}) with the corresponding optimum PC radius in the emitter region as a function of the emitter width (W_{em}) in the PC-HE and -SE solar cells.

simulated cells, when increasing W_{em}, both V_{oc} and J_{sc} increase, as shown in Fig. 5.5(a) and (b), while at the same time the FF decreases (see Fig. 5.5(c)). As a consequence, the efficiency curves of Fig. 5.5(d) exhibit a maximum value at a common optimum W_{em} value of 300 μm in all the simulated cells. Furthermore, in Fig. 5.5(d), thanks to the aforementioned recombination losses reduction for PC-SE cells in the emitter region, we also observe that the efficiency improvement achieved by the PC-SE design with respect to the PC-HE cell increases with W_{em}, ranging from about 0.19%$_{abs}$ at W_{em} = 200 μm up to about 0.25%$_{abs}$ at W_{em} = 500 μm.

5.5 Conclusions

In this chapter, we explored the effects of physical cell parameters on the BC-BJ solar cell performance, to optimize a novel point contact (PC) layout with a selective emitter. Basically, the study was focused on the impact of the SE design, featuring a local deeper highly-doped (HDOP) profile underneath rear point contacts and a narrower lowly-doped (LDOP) profile at the passivated rear interfaces in the emitter region by means of three-dimensional (3D) TCAD-based numerical simulations.

The results of such an analysis show that a co-optimization of the doping profiles in the LDOP and HDOP emitter regions leads to a further efficiency enhancement. In particular, the efficiency improvement of the PC-SE solar cell, as compared to the PC solar cell with

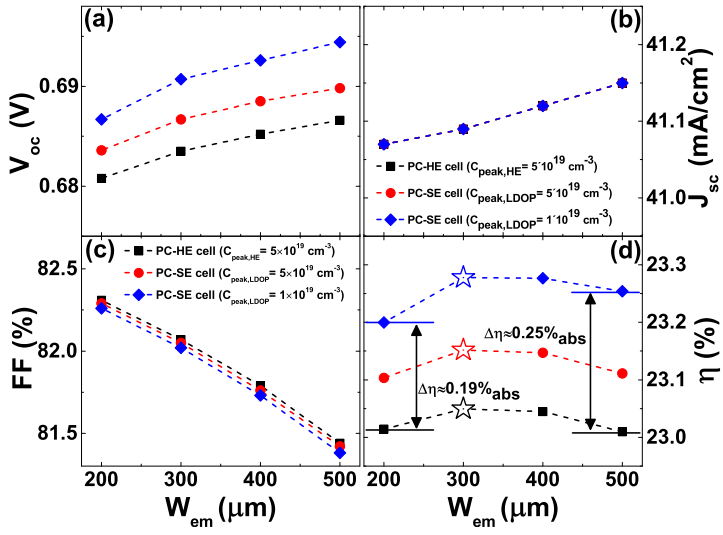

FIGURE 5.5: FOMs, such as (a) V_{oc}, (b) J_{sc}, (c) *FF* and (d) η, at the optimum rear contact fraction (CF_{opt}) as a function of the emitter width (W_{em}) for the point-contact (PC) solar cells with homogeneous emitter (HE) and selective emitter (SE) designs.

the homogeneously-doped emitter (HE), is more significant when increasing the emitter width (W_{em}), ranging from about 0.19%$_{abs}$ at W_{em} = 200 μm up to about 0.25%$_{abs}$ at W_{em} = 500 μm.

Conclusions

Nowadays, new ways of green energy become an important matter of study with a particular attention to the *solar power*, which is a remarkably renewable source of energy that we can freely harness on without fear of it ends one day. Photovoltaic (PV) research groups are focused on developing low-cost feasible manufacturing technology to enhance the performance of solar cell modules and thus, commercialize it as a real alternative to supply electrical power to rural and urban communities. The photovoltaic market is dominated by the crystalline silicon *c*-Si solar cell devices because of the specific and beneficial characteristics of this semiconductor material in the electronic industry. Therefore, the research on *c*-Si has a fundamental importance especially due to the low costs achieved and the promising wide enhancements on the future electronic applications.

Regarding PV architecture, conventional solar cells have some limitations affecting the short circuit current due to the presence of front contact grid pattern with bus bars leading to surface shadowing values of 7% to 8%. As a matter of fact, such losses have been strongly reduced by Sunpower, which developed the interdigitated back contact (IBC) solar cells initially proposed by Schwartz and Lammert [30, 116]. This structure has both contacts (back surface field (BSF) and emitter) located on the rear side of the cell and produced with an alternate diffusion process at high temperature. This technique allows the sun-ward side completely exposed thus maximizing the sunlight absorption. Since the IBC solar cells offer many advantages with respect to typical architecture it has become a very attractive structure to study among the PV industry and research groups. Therefore, this work of thesis is focused on the analysis of the favorable features of the back contact-back junction solar (BC-BJ) cell technology. To this purpose, the use of multidimensional simulation tools becomes essential to investigate and then optimize the architecture of the related BC-BJ solar cells, under standard test conditions (STC) in a quickly and economical way.

In the first chapter, an overall view on the current global warming effects, the advantages of adopting green energies such as solar power and a brief review of PV developments and recycling issues have been presented. Followed by the description of the main concepts related to the physics of the semiconductor devices, required to properly understand the behavior of solar cell structures. Then in the third chapter a general state-of-the-art properties related to *c*-Si solar cells were described. In particular, the *c*-Si models and parameters were presented with the aim to calibrate and implement a simulation platform that describes accurately the physics inside the studied BC-BJ solar cells. In the fourth

chapter a theoretical study based on a three-dimensional (3D) electro-optical device model simulations of the impact of a rear point-contact (PC) scheme on main figures of merit of a *c*-Si back contact-back-homojunction solar cells was presented.

The study was developed by means of the state-of-the-art TCAD simulations focused on the analysis of the main design parameters identifying dominant mechanisms that improve or degrade conversion efficiency. In particular, the performance of a BC-BJ solar cell with a PC scheme was evaluated as a function of the rear contact fraction (*CF*) and compared with a conventional BC-BJ solar cell featuring a linear-contact (*LC*) layout at the rear side of the structure. As a result of the analysis, the simulations show that the adoption of a thick and wide rear metallization contacting the silicon only via small circular-shaped holes (both in the BSF and emitter regions) allows an efficiency improvement of about 0.37$\%_{abs}$ with respect to the LC cell, mainly due to the reduction of series resistance losses related to the metal finger resistance, which is almost negligible in the PC structure.

On the other hand, It has been demonstrated that a typical screen-printed solar cell featuring a uniformly contacted back surface such as the linear-contact layout, is significantly affected by high recombination losses at the rear side of the device. Thereby, the realization of a rear point contact scheme is a potential strategy to enhance the performance of crystalline silicon (*c*-Si) solar cells. Additionally, PC layout is one of the most promising approaches to mitigate recombination losses at the backside of the cell device. In addition, three- dimensional (3D) TCAD-based numerical simulations were performed to investigate an advanced high- efficiency point contact (PC) BC-BJ solar cell with a selective emitter. Basically, we explored the effects of physical cell parameters related to the introduction of a selective emitter (SE) design with local highly-doped (HDOP) profile underneath rear point contacts and a narrower lowly-doped (LDOP) profile at the passivated rear interfaces in the emitter region simulations. The results of such an analysis show that a co-optimization of the doping profiles in the LDOP and HDOP emitter regions leads to a further efficiency enhancement. In particular, the efficiency improvement of the PC-SE solar cell, as compared to the PC solar cell with the homogeneously-doped emitter (HE), is more significant when increasing the emitter width (W_{em}), ranging from about 0.19$\%_{abs}$ at W_{em} = 200 μm up to about 0.25$\%_{abs}$ at W_{em} = 500 μm.

The results of the most relevant simulated back contact-back junction (BC-BJ) solar cells featuring LC and PC layouts, as well as PC with a selective emitter at the optimum contact fraction CF_{opt} are presented in chapters 4 and 5. Table. 5.2 reports the principal solar cell FOMs (i.e., J_{sc}, V_{oc}, FF and η) extracted from light *J-V* simulations, and the corresponding series resistance (R_s) and total dark saturation current density (J_0) extracted from dark *J-V* simulations.

BC-BJ solar cells	CF_{opt} (%)	J_{sc} (mA/cm^2)	V_{oc} (mV)	FF (%)	η (%)	R_s (Ω·cm^2)	J_0 (fA/cm^2)
LC-HE	18.8	41.02	680.1	81.28	22.68	0.37	274.4
PC-HE	11	41.09	683.5	82.07	23.05	0.19	257.5
PC-SE	11	41.09	690.7	82.02	23.28	0.21	227.0

TABLE 5.2: Summary results of the simulated BC-BJ solar cells at the optimum contact fraction (CF_{opt}) for W_{em} = 300 μm.

According to the above discussion, the LC-HE solar cell at the CF_{opt} exhibits higher R_s and J_0, thus corresponding to lower FF and V_{oc}, respectively, with respect to PC cells. Moreover, when compared to the PC-HE structure, the PC solar cell with the SE shows a slight R_s increase and, hence, a small FF decrease due to the increased emitter resistance in the LDOP regions, and a considerable J_0 decrease, mainly due to the reduced surface recombination losses at the contacted and non-contacted emitter interfaces, which results in higher V_{oc} and, consequently, higher conversion efficiency.

List of Publications

Journal Articles

- N. Guerra, R. De Rose, M. Guevara, P. Procel, M. Lanuzza, F. Crupi. “Understanding the impact of point-contact scheme and selective emitter in a c-Si BC-BJ solar cell by full 3D numerical simulations”. Accepted by Solar Energy, Elsevier (2017).
- M. Guevara, P. Procel, R. De Rose, N. Guerra, F. Crupi, M. Lanuzza. “Design guidelines for a metallization scheme with multiple-emitter contact lines in BC-BJ solar cells”. J. Comput. Electron., pp. 1–7, 2016.

Conference Papers

- S. Pierro, P. Procel, A. Ingenito, O. Isabella, M. Zeman, M. Guevara, N. Guerra, F. Crupi, G. Cocorullo. "Strategies of 1D optical profile extraction for bulk Silicon solar cell simulations". EOS (European Optical Society) Topical meetings, Italy (2015).
- M. Guevara, P. Procel, N. Guerra, S. Pierro, V. Maccaronio, F. Crupi, G. Cocorullo. “Numerical simulation of back contact-back junction solar cells with emitter double contact”. Italian Conference on Photonics Technologies, Fotonica AEIT, Torino 2015.
- P. Procel, M. Guevara, V. Maccaronio, N. Guerra, F. Crupi, G. Cocorullo. “Understanding the optimization of the emitter coverage in BC-BJ solar cells”. Conference on 140 Crystalline Silicon Photovoltaics, Energy Procedia, Volume 77, pp. 149–152 Konstanz 2015.

Bibliography

[1] S. Subak, P. Raskin, and D. Von Hippel, "National greenhouse gas accounts: Current anthropogenic sources and sinks", *Climatic Change*, vol. 25, no. 1, pp. 15–58, 1993.

[2] Q. Ma, *NASA, Greenhouse Gases: Refining the Role of Carbon Dioxide*, 1998.

[3] V. Quaschning, *Understanding renewable energy systems*. Routledge, 2016.

[4] A. A. Lacis, G. A. Schmidt, D. Rind, and R. A. Ruedy, "Atmospheric co2: Principal control knob governing earth's temperature", *Science*, vol. 330, no. 6002, pp. 356–359, 2010.

[5] N. J. Abram, H. V. McGregor, J. E. Tierney, M. N. Evans, N. P. McKay, D. S. Kaufman, K. Thirumalai, B. Martrat, H. Goosse, S. J. Phipps, E. J. Steig, K. H. Kilbourne, C. P. Saenger, J. Zinke, G. Leduc, J. A. Addison, P. G. Mortyn, M.-S. Seidenkrantz, M.-A. Sicre, K. Selvaraj, H. L. Filipsson, R. Neukom, J. Gergis, M. A. J. Curran, and L. von Gunten, "Early onset of industrial-era warming across the oceans and continents", *Nature*, vol. 536, no. 7617, pp. 411–418, 2016.

[6] IPCC, "Intergovernmental panel on climate change: Change, intergovernmental panel on climate", *Climate change*, 2014.

[7] K. Mertens, *Photovoltaics: Fundamentals, technology and practice*. Wiley, 2013.

[8] W. M. Organization, *World Meteorological Organization: WMO's Greenhouse Gas Bulletin*, 2014.

[9] International Energy Agency (IEA), "Energy and Climate, World energy outlook special report", 2015.

[10] J. M. Agency, *Japan Meteorological Agency: Global Average Surface Temperature Anomalies*, 2017.

[11] N. Aeronautics and S. Administration, *NASA, NOAA Data Show 2016 Warmest Year on Record Globally*, 2017.

[12] ——, *NASA, February 2017 Was Second Warmest February On Record*, 2017.

[13] A. Savaresi, "The paris agreement: A new beginning?", *Journal of Energy & Natural Resources Law*, vol. 34, no. 1, pp. 16–26, 2016.

[14] J. Rogelj, M. Den Elzen, N. Höhne, T. Fransen, H. Fekete, H. Winkler, R. Schaeffer, F. Sha, K. Riahi, and M. Meinshausen, "Paris agreement climate proposals need a boost to keep warming well below 2 c", *Nature*, vol. 534, no. 7609, pp. 631–639, 2016.

[15] United Nations - Framework Convention on Climate Change (UNFCCC), "Adoption of the Paris Agreement", 2015.

[16] European Commission, "Implementing the Paris Agreement - Progress of the EU towards the at least -40% target. Climate action.", 2016.

[17] REN21, *Renewables 2016, Global status report*, 2016.

[18] Solargis, "GIS data and maps", 2016.

[19] Solar Power Europe, "Solar Market Report 2015", 2016.

[20] Gestore servizi energetici, "Rapporto statistico Solare fotovoltaico, GSE", 2015.

[21] Trasmissione Elettrica Rete Nazionale, "Elaborazione Anie Rinnovabili, Dati GAUDì (Gestione Anagrafica Unica degli Impianti), TERNA", 2016.

[22] Construction21.eu, "Sustainable Urban Building Award: Omnia Energia Corp.", 2013.

[23] S. Weckend, A. Wade, and G. Heath, "End-of-life management: Solar photovoltaic panels", NREL (National Renewable Energy Laboratory (NREL), Golden, CO (United States)), Tech. Rep., 2016.

[24] V. M. Fthenakis, "End-of-life management and recycling of pv modules", *Energy Policy*, vol. 28, no. 14, pp. 1051–1058, 2000.

[25] V. Fthenakis and P. Moskowitz, "Thin-film photovoltaic cells: Health and environmental issues in their manufacture use and disposal", *Progress in Photovoltaics: Research and Applications*, vol. 3, no. 5, pp. 295–306, 1995.

[26] P. D. Moskowitz, V. M. Fthenakis, R. S. Crandall, and B. P. Nelson, "Analyzing risks associated with hazardous production materials", *Solid State Technology*, vol. 37, no. 7, pp. 121–126, 1994.

[27] U. DOE, "The potential of renewable energy: An interlaboratory white paper", *Paper DE90000322, Washington, DC*, 1990.

[28] A. Smets, K. Jäger, O. Isabella, R. Swaaij, and M. Zeman, *Solar energy: The physics and engineering of photovoltaic conversion, technologies and systems*. UIT Cambridge, 2016.

[29] D. M. Chapin, C. Fuller, and G. Pearson, "A new silicon p-n junction photocell for converting solar radiation into electrical power", *Journal of Applied Physics*, vol. 25, no. 5, pp. 676–677, 1954.

[30] R. Schwartz and M. Lammert, "Silicon solar cells for high concentration applications", in *Electron Devices Meeting, 1975 International*, IEEE, vol. 21, 1975, pp. 350–352.

[31] J. Zhao, A. Wang, and M. A. Green, "24· 5% efficiency silicon pert cells on mcz substrates and 24· 7% efficiency perl cells on fz substrates", *Progress in Photovoltaics: Research and Applications*, vol. 7, no. 6, pp. 471–474, 1999.

[32] M. A. Green, "The path to 25% silicon solar cell efficiency: History of silicon cell evolution", *Progress in Photovoltaics: Research and Applications*, vol. 17, no. 3, pp. 183–189, 2009.

[33] S. S. Hegedus and A. Luque, "Status, trends, challenges and the bright future of solar electricity from photovoltaics", *Handbook of photovoltaic science and engineering*, pp. 1–43, 2003.

[34] K. Masuko, M. Shigematsu, T. Hashiguchi, D. Fujishima, M. Kai, N. Yoshimura, T. Yamaguchi, Y. Ichihashi, T. Mishima, N. Matsubara, *et al.*, "Achievement of more than 25% conversion efficiency with

crystalline silicon heterojunction solar cell", *IEEE Journal of Photovoltaics*, vol. 4, no. 6, pp. 1433–1435, 2014.

[35] D. D. Smith, P. Cousins, S. Westerberg, R. De Jesus-Tabajonda, G. Aniero, and Y.-C. Shen, "Toward the practical limits of silicon solar cells", *IEEE Journal of Photovoltaics*, vol. 6, no. 4, pp. 1465–1469, 2014.

[36] E. Franklin, K. Fong, K. McIntosh, A. Fell, A. Blakers, T. Kho, D. Walter, D. Wang, N. Zin, M. Stocks, *et al.*, "Design, fabrication and characterisation of a 24.4% efficient interdigitated back contact solar cell", *Progress in Photovoltaics: research and applications*, vol. 24, no. 4, pp. 411–427, 2016.

[37] K. Yoshikawa, H. Kawasaki, W. Yoshida, T. Irie, K. Konishi, K. Nakano, T. Uto, D. Adachi, M. Kanematsu, H. Uzu, and K. Yamamoto, "Silicon heterojunction solar cell with interdigitated back contacts for a photoconversion efficiency over 26%", *Nature Energy*, vol. 2, p. 17 032, 2017.

[38] R. M. Swanson, S. K. Beckwith, R. A. Crane, W. D. Eades, Y. H. Kwark, R. Sinton, and S. Swirhun, "Point-contact silicon solar cells", *IEEE Transactions on Electron Devices*, vol. 31, no. 5, pp. 661–664, 1984.

[39] Fraunhofer Institute for Solar Energy Systems, ISE, "Photovoltaics Reports, 17 November", 2016.

[40] Solar Power Europe, "Global Market Outlook for Solar Power 2016-2020. SPE former EPIA (European Photovoltaic Industry Association)", 2016.

[41] Massachusetts Institute of Technology, "Solar photovoltaic technologies, MIT", 2015.

[42] P. Altermatt, S Steingrube, Y Yang, C Sprodowski, T Dezhdar, S Koc, B Veith, S Herrman, R Bock, K Bothe, *et al.*, "Highly predictive modelling of entire si solar cells for industrial applications", in *Proc. 24th Eur. Photovoltaic Solar Energy Conf.*, 2009, pp. 901–906.

[43] R. De Rose, M. Zanuccoli, P. Magnone, E. Sangiorgi, and C. Fiegna, "Open issues for the numerical simulation of silicon solar cells", in *Ultimate Integration on Silicon (ULIS), 2011 12th International Conference on*, IEEE, 2011, pp. 1–4.

[44] P. P. Altermatt, "Models for numerical device simulations of crystalline silicon solar cells—a review", *Journal of Computational Electronics*, vol. 10, no. 3, pp. 314–330, 2011.

[45] *Synopsys Inc., Sentaurus Device User Guide. Version J-2014.09*, Mountain View, CA, USA, 2014.

[46] J. L. Gray, *The physics of the solar cell*. John Wiley & Sons, Ltd, 2011, pp. 82–129.

[47] A. R. Burgers, *New metallisation patterns and analysis of light trapping for silicon solar cells*. Energieonderzoek Centrum Nederland, 2005.

[48] M. Tao, *Terawatt solar photovoltaics: Roadblocks and opportunities*. Springer, 2014.

[49] E. Lorenzo, *Solar electricity: Engineering of photovoltaic systems*. Earthscan/James & James, 1994.

[50] *National instruments in academia*, Photovoltaic Cell Overview (Part I), National Instruments Corporation, Dec. 2009.

[51] M. A. Green, K. Emery, Y. Hishikawa, W. Warta, and E. D. Dunlop, "Solar cell efficiency tables (version 45)", *Progress in photovoltaics: research and applications*, vol. 23, no. 1, pp. 1–9, 2015.

[52] D. Adachi, J. L. Hernández, and K. Yamamoto, "Impact of carrier recombination on fill factor for large area heterojunction crystalline silicon solar cell with 25.1% efficiency", *Applied Physics Letters*, vol. 107, no. 23, p. 233 506, 2015.

[53] F Feldmann, M Simon, M Bivour, C Reichel, M Hermle, and S. Glunz, "Carrier-selective contacts for si solar cells", *Applied Physics Letters*, vol. 104, no. 18, p. 181 105, 2014.

[54] S. Glunz, F Feldmann, A Richter, M Bivour, C Reichel, H Steinkemper, J Benick, and M Hermle, "The irresistible charm of a simple current flow pattern—25% with a solar cell featuring a full-area back contact", in *Proceedings of the 31st European Photovoltaic Solar Energy Conference and Exhibition*, 2015, pp. 259–263.

[55] M. A. Green, K. Emery, Y. Hishikawa, W. Warta, and E. D. Dunlop, "Solar cell efficiency tables (version 47)", *Progress in Photovoltaics: Research and Applications*, vol. 24, no. NREL/JA-5J00-65643, 2016.

[56] M. Taguchi, A. Yano, S. Tohoda, K. Matsuyama, Y. Nakamura, T. Nishiwaki, K. Fujita, and E. Maruyama, "24.7% record efficiency hit solar cell on thin silicon wafer", *IEEE Journal of Photovoltaics*, vol. 4, no. 1, pp. 96–99, 2014.

[57] J. Geissbühler, J. Werner, S. M. De Nicolas, L. Barraud, A. Hessler-Wyser, M. Despeisse, S. Nicolay, A. Tomasi, B. Niesen, S. De Wolf, *et al.*, "22.5% efficient silicon heterojunction solar cell with molybdenum oxide hole collector", *Applied Physics Letters*, vol. 107, no. 8, p. 081 601, 2015.

[58] L. Tous, M. Aleman, R. Russell, E. Cornagliotti, P. Choulat, A Uruena, S. Singh, J. John, F. Duerinckx, J. Poortmans, *et al.*, "Evaluation of advanced p-perl and n-pert large area silicon solar cells with 20.5% energy conversion efficiencies", *Progress in Photovoltaics: Research and Applications*, vol. 23, no. 5, pp. 660–670, 2015.

[59] M. R. Payo, F Duerinckx, Y Li, and E Cornagliotti, "Advanced Doping Profiles By Selective Epitaxy Energy Pert Cells in N-Type", in *31st European Photovoltaic Solar Energy Conference and Exhibition*, WIP, 2015, pp. 433–439.

[60] A. Becquerel, "Memoire sur les effects delectriques produits sous linfluence des rayons solaires", *Annalen der Physick und Chemie*, vol. 54, pp. 35–42, 1841.

[61] A. Einstein, "On a heuristic point of view concerning the generation and transformation of light", *Ann. Phys.*, vol. 322, no. 6, pp. 132–148, 1905.

[62] A. Luque and S. Hegedus, *Handbook of photovoltaic science and engineering*. Wiley, 2011.

[63] R. De Rose, "Investigation of silicon solar cells by means of electro-optical numerical simulations", PhD thesis, 2012.

[64] B. Van Zeghbroeck, "Principles of semiconductor devices", *Colarado University*, 2004.

[65] S. M. Sze, *Semiconductor devices: Physics and technology, 2nd ed.* John Wiley Sons Inc, New York, NY, 2002.

[66] S. Sze and K. Ng, *Physics of semiconductor devices, 3rd ed.* Wiley, 2006.

[67] C. Hu, *Modern semiconductor devices for integrated circuits*. Prentice Hall, 2010.

[68] M. A. Green, "Solar cells: Operating principles, technology, and system applications", 1982.

[69] J. O. Schumacher, "Numerical simulation of silicon solar cells with novel cell structures", PhD thesis, 2000.

[70] M Haouari-Merbah, M Belhamel, I Tobias, and J. Ruiz, "Method of extraction and analysis of solar cell parameters from the dark current-voltage curve", in *Electron Devices, 2005 Spanish Conference on*, IEEE, 2005, pp. 275–277.

[71] H. J. Snaith, "The perils of solar cell efficiency measurements", *Nature Photonics*, vol. 6, no. 6, pp. 337–340, 2012.

[72] H Schlangenotto, H Maeder, and W Gerlach, "Temperature dependence of the radiative recombination coefficient in silicon", *physica status solidi (a)*, vol. 21, no. 1, pp. 357–367, 1974.

[73] P. Auger, "Sur les rayons β secondaires produits dans un gaz par des rayons x", *C.R.A.S.*, vol. 177, pp. 169–171, 1923.

[74] W. Shockley and W. T. Read, "Statistics of the recombinations of holes and electrons", *Physical Review*, vol. 87, no. 5, p. 835, 1952.

[75] R. N. Hall, "Electron-hole recombination in germanium", *Phys. Rev.*, vol. 87, no. 2, p. 387, 1952.

[76] S. Glunz, S Sterk, R Steeman, W Warta, J Knobloch, and W Wettling, "Emitter dark saturation currents of high-efficiency solar cells with inverted pyramids", in *Proceedings of the 13th European Photovoltaic Solar Energy Conference*, 1995, pp. 409–12.

[77] P. P. Altermatt, J. O. Schumacher, A. Cuevas, M. J. Kerr, S. W. Glunz, R. R. King, G. Heiser, and A. Schenk, "Numerical modeling of highly doped si: P emitters based on fermi-dirac statistics and self-consistent material parameters", *Journal of Applied Physics*, vol. 92, no. 6, pp. 3187–3197, 2002.

[78] D. Roulston, N. Arora, and S. Chamberlain, "Modeling and measurement of minority-carrier lifetime versus doping in diffused layers of n+-p silicon diodes", *IEEE Transactions on Electron Devices*, vol. 29, no. 2, pp. 284–291, 1982.

[79] H. Haug, "New methods for investigation of surface passivation layers for crystalline silicon solar cells", PhD thesis, Faculty of Mathematics and Natural Sciences, University of Oslo, Norway, Mar. 2014.

[80] A. Richter, S. W. Glunz, F. Werner, J. Schmidt, and A. Cuevas, "Improved quantitative description of auger recombination in crystalline silicon", *Physical Review B*, vol. 86, no. 16, p. 165 202, 2012.

[81] R. Sinton and R. Swanson, "Recombination in highly injected silicon", *Electron Devices, IEEE Transactions on*, vol. 34, no. 6, pp. 1380 –1389, 1987.

[82] P. P. Altermatt, R. Sinton, and G. Heiser, "Improvements in numerical modelling of highly injected crystalline silicon solar cells", *Solar Energy Materials and Solar Cells*, vol. 65, 149–155(7), 2001.

[83] R Hezel and K Jaeger, "Low-temperature surface passivation of silicon for solar cells", *Journal of the Electrochemical Society*, vol. 136, no. 2, pp. 518–523, 1989.

[84] A. G. Aberle, "Surface passivation of crystalline silicon solar cells: A review", *Progress in Photovoltaics: Research and Applications*, vol. 8, no. 5, pp. 473–487, 2000.

[85] B. Richards, "Comparison of tio2 and other dielectric coatings for buried-contact solar cells: A review", *Progress in Photovoltaics: Research and Applications*, vol. 12, no. 4, pp. 253–281, 2004.

[86] E Yablonovitch, D. Allara, C. Chang, T Gmitter, and T. Bright, "Unusually low surface-recombination velocity on silicon and germanium surfaces", *Physical review letters*, vol. 57, no. 2, p. 249, 1986.

[87] D. Fenner, D. Biegelsen, and R. Bringans, "Silicon surface passivation by hydrogen termination: A comparative study of preparation methods", *Journal of Applied Physics*, vol. 66, no. 1, pp. 419–424, 1989.

[88] G. W. Trucks, K. Raghavachari, G. S. Higashi, and Y. J. Chabal, "Mechanism of hf etching of silicon surfaces: A theoretical understanding of hydrogen passivation", *Phys. Rev. Lett.*, vol. 65, pp. 504–507, 4 1990.

[89] J. J. Boland, "Scanning tunnelling microscopy of the interaction of hydrogen with silicon surfaces", *Advances in physics*, vol. 42, no. 2, pp. 129–171, 1993.

[90] S. Glunz, D Biro, S Rein, and W Warta, "Field-effect passivation of the sio2si interface", *Journal of Applied Physics*, vol. 86, no. 1, pp. 683–691, 1999.

[91] B Hoex, J. Gielis, M. Van de Sanden, and W. Kessels, "On the c-si surface passivation mechanism by the negative-charge-dielectric al2o3", *Journal of Applied Physics*, vol. 104, no. 11, p. 113 703, 2008.

[92] A. G. Aberle, *Crystalline silicon solar cells: Advanced surface passivation and analysis*. Centre for Photovoltaic Engineering. University of New South Wales, 1999.

[93] W. D. Eades and R. M. Swanson, "Calculation of surface generation and recombination velocities at the si-sio2 interface", *Journal of applied Physics*, vol. 58, no. 11, pp. 4267–4276, 1985.

[94] E Yablonovitch, R. Swanson, W. Eades, and B. Weinberger, "Electron-hole recombination at the si-sio2 interface", *Applied Physics Letters*, vol. 48, no. 3, pp. 245–247, 1986.

[95] A. G. Aberle, S. Glunz, and W. Warta, "Impact of illumination level and oxide parameters on shockley–read–hall recombination at the si-sio2 interface", *Journal of Applied Physics*, vol. 71, no. 9, pp. 4422–4431, 1992.

[96] K Yasutake, Z Chen, S. Pang, and A Rohatgi, "Modeling and characterization of interface state parameters and surface recombination velocity at plasma enhanced chemical vapor deposited sio2–si interface", *Journal of applied physics*, vol. 75, no. 4, pp. 2048–2054, 1994.

[97] O Schultz, S. Glunz, and G. Willeke, "Short communication: Accelerated publication: Multicrystalline silicon solar cells exceeding 20% efficiency", *Progress in Photovoltaics: Research and Applications*, vol. 12, no. 7, pp. 553–558, 2004.

[98] T. Lauinger, J. Schmidt, A. G. Aberle, and R. Hezel, "Record low surface recombination velocities on 1 Ω cm p-silicon using remote plasma silicon nitride passivation", *Applied Physics Letters*, vol. 68, no. 9, pp. 1232–1234, 1996.

[99] M. Kerr, J Schmidt, A Cuevas, and J. Bultman, "Surface recombination velocity of phosphorus-diffused silicon solar cell emitters passivated with plasma enhanced chemical vapor deposited silicon nitride and thermal silicon oxide", *Journal of Applied Physics*, vol. 89, no. 7, pp. 3821–3826, 2001.

[100] H Mackel and R Ludemann, "Detailed study of the composition of hydrogenated sinx layers for high-quality silicon surface passivation", *Journal of Applied Physics*, vol. 92, no. 5, pp. 2602–2609, 2002.

[101] A. G. Aberle, "Overview on sin surface passivation of crystalline silicon solar cells", *Solar Energy Materials and Solar Cells*, vol. 65, no. 1, pp. 239–248, 2001.

[102] I Martin, M Vetter, A Orpella, J Puigdollers, A Cuevas, and R Alcubilla, "Surface passivation of p-type crystalline si by plasma enhanced chemical vapor deposited amorphous sicx: H films", *Applied Physics Letters*, vol. 79, no. 14, pp. 2199–2201, 2001.

[103] S Janz, S Riepe, M Hofmann, S Reber, and S Glunz, "Phosphorus-doped sic as an excellent p-type si surface passivation layer", *Applied Physics Letters*, vol. 88, no. 13, 2006.

[104] G Agostinelli, A Delabie, P Vitanov, Z Alexieva, H. Dekkers, S De Wolf, and G Beaucarne, "Very low surface recombination velocities on p-type silicon wafers passivated with a dielectric with fixed negative charge", *Solar Energy Materials and Solar Cells*, vol. 90, no. 18, pp. 3438–3443, 2006.

[105] B. Hoex, J. Schmidt, P Pohl, M. Van de Sanden, and W. Kessels, "Silicon surface passivation by atomic layer deposited al2o3", *Journal of Applied Physics*, vol. 104, no. 4, p. 044 903, 2008.

[106] G. Dingemans and W. Kessels, "Status and prospects of al2o3-based surface passivation schemes for silicon solar cells", *Journal of Vacuum Science & Technology A*, vol. 30, no. 4, p. 040 802, 2012.

[107] J. Pankove and M. Tarng, "Amorphous silicon as a passivant for crystalline silicon", *Applied Physics Letters*, vol. 34, no. 2, pp. 156–157, 1979.

[108] S. Olibet, E. Vallat-Sauvain, and C. Ballif, "Model for a-si: H/c-si interface recombination based on the amphoteric nature of silicon dangling bonds", *Physical Review B*, vol. 76, no. 3, p. 035 326, 2007.

[109] M. Z. Rahman and S. I. Khan, "Advances in surface passivation of c-si solar cells", *Materials for Renewable and Sustainable Energy*, vol. 1, no. 1, p. 1, 2012.

[110] D. K. Schroder and D. L. Meier, "Solar cell contact resistance—a review", *IEEE Transactions on electron devices*, vol. 31, no. 5, pp. 637–647, 1984.

[111] K. Emery, J. Burdick, Y. Caiyem, D. Dunlavy, H. Field, B. Kroposki, T. Moriarty, L. Ottoson, S. Rummel, T. Strand, *et al.*, "Temperature dependence of photovoltaic cells, modules and systems", in *Photovoltaic Specialists Conference, 1996., Conference Record of the Twenty Fifth IEEE*, IEEE, 1996, pp. 1275–1278.

[112] E. Radziemska, "The effect of temperature on the power drop in crystalline silicon solar cells", *Renewable Energy*, vol. 28, no. 1, pp. 1–12, 2003.

[113] D. L. King, J. A. Kratochvil, and W. E. Boyson, "Temperature coefficients for pv modules and arrays: Measurement methods, difficulties, and results", in *Photovoltaic Specialists Conference, 1997., Conference Record of the Twenty-Sixth IEEE*, IEEE, 1997, pp. 1183–1186.

[114] J Zhao, "Passivated emitter rear locally diffused solar cells", *Bulletin of advanced technology research*, vol. 5, no. 8, 2011.

[115] M. A. Green, *Silicon solar cells: Advanced principles & practice*. Centre for Photovoltaic Devices and Systems, University of New South Wales, 1995.

[116] M. D. Lammert and R. J. Schwartz, "The interdigitated back contact solar cell: A silicon solar cell for use in concentrated sunlight", *IEEE Transactions on Electron Devices*, vol. 24, no. 4, pp. 337–342, 1977.

[117] P. Verlinden, "Interdigitated back contact solar cells", *Photovoltaic Solar Energy: From Fundamentals to Applications*, p. 92, 2017.

[118] F Granek, M Hermle, C Reichel, O Schultz-Wittmann, and S. Glunz, "High-efficiency back-contact back-junction silicon solar cell research at fraunhofer ise", in *Proceedings of the 23rd European Photovoltaic Solar Energy Conference*, 2008, pp. 991–995.

[119] R. Sinton, Y. Kwark, J. Gan, and R. M. Swanson, "27.5-percent silicon concentrator solar cells", *IEEE Electron Device Letters*, vol. 7, no. 10, pp. 567–569, 1986.

[120] W. P. Mulligan, D. H. Rose, M. J. Cudzinovic, D. M. De Ceuster, K. R. McIntosh, D. D. Smith, and R. M. Swanson, "Manufacture of solar cells with 21% efficiency", *Proc. 19th EPVSEC*, vol. 387, 2004.

[121] Z. C. Holman, S. De Wolf, and C. Ballif, "Improving metal reflectors by suppressing surface plasmon polaritons: A priori calculation of the internal reflectance of a solar cell", *Light: Science & Applications*, vol. 2, no. 10, e106, 2013.

[122] J.-M. Jin, *The finite element method in electromagnetics*. John Wiley & Sons, 2015.

[123] P. P. Altermatt, "Models for numerical device simulations of crystalline silicon solar cells—a review", *Journal of computational electronics*, vol. 10, no. 3, p. 314, 2011.

[124] J. Gray, "Two-dimensional modeling of silicon solar cells. [scap2d]", 1982.

[125] M. Burgelman, J. Verschraegen, S. Degrave, and P. Nollet, "Modeling thin-film pv devices", *Progress in Photovoltaics: Research and Applications*, vol. 12, no. 2-3, pp. 143–153, 2004.

[126] M Belarbi, A Benyoucef, and B Benyoucef, "Simulation of the solar cells with pc1d, application to cells based on silicon", *Advanced Energy: An International Journal (AEIJ)*, vol. 1, pp. 1–10, 2014.

[127] University of North South Wales (USNW). School of Photovoltaic and Renewable Energy Engineering, *PC1D - Software for modelling a solar cell | School of Photovoltaic and Renewable Energy Engineering*, 2014.

[128] G. Thorson and P. Basore, "Semiconductor device modeling on personal computers: Pc-1d version 2", *Electrosoft*, vol. 2, no. 1, pp. 6–12, 1991.

[129] R. Brendel, "Modeling solar cells with the dopant-diffused layers treated as conductive boundaries", *Progress in Photovoltaics: Research and Applications*, vol. 20, no. 1, pp. 31–43, 2012.

[130] C Vázquez, J Alonso, M. Vázquez, L. Caballero, R Romero, and J. Ramos-Barrado, "Efficiency of commercial cz-si solar cell with a shallow emitter", *Materials Science and Engineering: B*, vol. 172, no. 1, pp. 43–49, 2010.

[131] P. Basore, "Pc-1d version 3: Improved speed and convergence", in *Photovoltaic Specialists Conference, 1991., Conference Record of the Twenty Second IEEE*, IEEE, 1991, pp. 299–302.

[132] D. A. Clugston and P. A. Basore, "Pc1d version 5: 32-bit solar cell modeling on personal computers", in *Photovoltaic Specialists Conference, 1997., Conference Record of the Twenty-Sixth IEEE*, IEEE, 1997, pp. 207–210.

[133] S. Sepeai, S. H. Zaidi, M. Desa, M. Sulaiman, N. Ludin, M. A. Ibrahim, and K Sopian, "Design optimization of bifacial solar cell by pc1d simulation", *parameters*, vol. 3, no. 5, 2013.

[134] K. Wang and I. Perez-Wurfl, "A method to overcome the time step limitation of pc1d in transient excitation mode", *Energy Procedia*, vol. 55, pp. 155–160, 2014.

[135] R. E. Bank, D. J. Rose, and W. Fichtner, "Numerical methods for semiconductor device simulation", *SIAM Journal on Scientific and Statistical Computing*, vol. 4, no. 3, pp. 416–435, 1983.

[136] S Muller, K. Kells, and W. Fichtner, "Automatic rectangle-based adaptive mesh generation without obtuse angles", *IEEE transactions on computer-aided design of integrated circuits and systems*, vol. 11, no. 7, pp. 855–863, 1992.

[137] G. Heiser, C. Pommerell, J. Weis, and W. Fichtner, "Three-dimensional numerical semiconductor device simulation: Algorithms, architectures, results", *IEEE transactions on computer-aided design of integrated circuits and systems*, vol. 10, no. 10, pp. 1218–1230, 1991.

[138] A. G. Aberle, G. Heiser, and M. A. Green, "Two-dimensional minority carrier flow in high-efficiency silicon solar cells at short-circuit, open-circuit and maximum power point operating conditions", *Solar energy materials and solar cells*, vol. 34, no. 1-4, pp. 149–160, 1994.

[139] G. Heiser, A. G. Aberle, S. R. Wenham, and M. A. Green, "Two-dimensional numerical simulations of high-efficiency silicon solar cells", *Microelectronics journal*, vol. 26, no. 2, pp. 273–286, 1995.

[140] A. G. Aberle, P. P. Altermatt, G. Heiser, S. J. Robinson, A. Wang, J. Zhao, U. Krumbein, and M. A. Green, "Limiting loss mechanisms in 23% efficient silicon solar cells", *Journal of Applied Physics*, vol. 77, no. 7, pp. 3491–3504, 1995.

[141] J Zhao, A Wang, P Altermatt, and M. Green, "Twenty-four percent efficient silicon solar cells with double layer antireflection coatings and reduced resistance loss", *Applied Physics Letters*, vol. 66, no. 26, pp. 3636–3638, 1995.

[142] P. P. Altermatt, G. Heiser, A. G. Aberle, A. Wang, J. Zhao, S. J. Robinson, S. Bowden, and M. A. Green, "Spatially resolved analysis and minimization of resistive losses in high-efficiency si solar cells", *Progress in photovoltaics: research and applications*, vol. 4, no. 6, pp. 399–414, 1996.

[143] S. Glunz, J Schumacher, W Warta, J Knobloch, and W Wettling, "Solar cells with mesh-structured emitter", *Progress in Photovoltaics: Research and Applications*, vol. 4, no. 6, pp. 415–424, 1996.

[144] F. Granek, M. Hermle, D. M. Huljić, O. Schultz-Wittmann, and S. W. Glunz, "Enhanced lateral current transport via the front n+ diffused layer of n-type high-efficiency back-junction back-contact silicon solar cells", *Progress in photovoltaics: research and applications*, vol. 17, no. 1, pp. 47–56, 2009.

[145] S. Kluska, F. Granek, M. Rüdiger, M. Hermle, and S. W. Glunz, "Modeling and optimization study of industrial n-type high-efficiency back-contact back-junction silicon solar cells", *Solar Energy Materials and Solar Cells*, vol. 94, no. 3, pp. 568–577, 2010.

[146] P. Helm, H. Ossenbrink, W. Freieslenben, and W. Palz, *Proceedings of the 13th european photovoltaic solar energy conference*. Earthscan/James & James, 1996.

[147] A. Fell, K. R. McIntosh, P. P. Altermatt, G. J. M. Janssen, R. Stangl, A. Ho-Baillie, H. Steinkemper, J. Greulich, M. Müller, B. Min, K. C. Fong, M. Hermle, I. G. Romijn, and M. D. Abbott, "Input parameters for the simulation of silicon solar cells in 2014", *IEEE Journal of Photovoltaics*, vol. 5, no. 4, pp. 1250–1263, 2015.

[148] A. Ingenito, O. Isabella, and M. Zeman, "Nano-cones on micropyramids: Modulated surface textures for maximal spectral response

and high-efficiency solar cells", *Progress in Photovoltaics: Research and Applications*, vol. 23, no. 11, pp. 1649–1659, 2015.

[149] S. C. Baker-Finch and K. R. McIntosh, "One-dimensional photogeneration profiles in silicon solar cells with pyramidal texture", *Progress in Photovoltaics: Research and Applications*, vol. 20, no. 1, pp. 51–61, 2012.

[150] I. E. Commission *et al.*, "Photovoltaic devices—part 3: Measurement principles for terrestrial photovoltaic (pv) solar devices with reference spectral irradiance data", *IEC 60904–3 ed2*, 2008.

[151] E. Yablonovitch, "Statistical ray optics", *JOSA*, vol. 72, no. 7, pp. 899–907, 1982.

[152] P. Campbell and M. A. Green, "Light trapping properties of pyramidally textured surfaces", *Journal of Applied Physics*, vol. 62, no. 1, pp. 243–249, 1987.

[153] P Campbell, "Light trapping in textured solar cells", *Solar energy materials*, vol. 21, no. 2-3, pp. 165–172, 1990.

[154] ——, "Enhancement of light absorption from randomizing and geometric textures", *JOSA B*, vol. 10, no. 12, pp. 2410–2415, 1993.

[155] V. Moroz, J. Huang, K. Wijekoon, and D. Tanner, "Experimental and theoretical analysis of the optical behavior of textured silicon wafers", in *2011 37th IEEE Photovoltaic Specialists Conference*, IEEE, 2011, pp. 002 900–002 905.

[156] K. E. Bean *et al.*, "Anisotropic etching of silicon", *IEEE Transactions on Electron Devices*, vol. 25, no. 10, pp. 1185–1193, 1978.

[157] C. Gueymard, *Smarts2: A simple model of the atmospheric radiative transfer of sunshine: Algorithms and performance assessment*. Florida Solar Energy Center Cocoa, FL, 1995.

[158] J. Pla, J. Duran, D. Skigin, and R. Depine, "Ray tracing vs. electromagnetic methods in the analysis of antireflective textured surfaces [of solar cells]", in *Photovoltaic Specialists Conference, 1997., Conference Record of the Twenty-Sixth IEEE*, IEEE, 1997, pp. 187–190.

[159] M. Guevara, P. Procel, R. De Rose, N. Guerra, F. Crupi, and M. Lanuzza, "Design guidelines for a metallization scheme with multiple-emitter contact lines in bc-bj solar cells", *Journal of Computational Electronics*, vol. 15, no. 4, pp. 1498–1504, 2016.

[160] P. Procel, M. Zanuccoli, V. Maccaronio, F. Crupi, G. Cocorullo, P. Magnone, and C. Fiegna, "Numerical simulation of the impact of design parameters on the performance of back-contact back-junction solar cell", *Journal of Computational Electronics*, vol. 15, no. 1, pp. 260–268, 2016.

[161] C Zechner, P Fath, G Willeke, and E Bucher, "Two-and three- dimensional optical carrier generation determination in crystalline silicon solar cells", *Solar energy materials and solar cells*, vol. 51, no. 3, pp. 255–267, 1998.

[162] O. Isabella, H. Sai, M. Kondo, and M. Zeman, "Full-wave optoelectrical modeling of optimized flattened light-scattering substrate for high efficiency thin-film silicon solar cells", *Progress in Photovoltaics: Research and Applications*, vol. 22, no. 6, pp. 671–689, 2014.

[163] Z. Holman and M. Boccard, "Light management in silicon solar cells", *Photovoltaic Solar Energy: From Fundamentals to Applications*, p. 136, 2017.

[164] T. Yagi, Y. Uraoka, and T. Fuyuki, "Ray-trace simulation of light trapping in silicon solar cell with texture structures", *Solar Energy Materials and Solar Cells*, vol. 90, no. 16, pp. 2647 –2656, 2006.

[165] P. P. Altermatt, H Plagwitz, R Bock, J. Schmidt, R Brendel, M. J. Kerr, A. Cuevas, *et al.*, "The surface recombination velocity at boron-doped emitters: Comparison between various passivation techniques", in *Proceedings of the 21st European Photovoltaic Solar Energy Conference*, WIP Renewable Energies Dresden, Germany, 2006, pp. 647–650.

[166] J. Fossum, R. Mertens, D. Lee, and J. Nijs, "Carrier recombination and lifetime in highly doped silicon", *Solid-State Electronics*, vol. 26, no. 6, pp. 569 –576, 1983.

[167] W. Van Roosbroeck, "Theory of the flow of electrons and holes in germanium and other semiconductors", *Bell System Technical Journal*, vol. 29, no. 4, pp. 560–607, 1950.

[168] A. Schenk, "Finite-temperature full random-phase approximation model of band gap narrowing for silicon device simulation", *Journal of Applied Physics*, vol. 84, no. 7, pp. 3684–3695, 1998.

[169] D. Klaassen, "A unified mobility model for device simulation—i. model equations and concentration dependence", *Solid-State Electronics*, vol. 35, no. 7, pp. 953–959, 1992.

[170] K. Misiakos and D. Tsamakis, "Accurate measurements of the silicon intrinsic carrier density from 78 to 340 k", *Journal of applied physics*, vol. 74, no. 5, pp. 3293–3297, 1993.

[171] P. P. Altermatt, A. Schenk, F. Geelhaar, and G. Heiser, "Reassessment of the intrinsic carrier density in crystalline silicon in view of band-gap narrowing", *Journal of Applied Physics*, vol. 93, no. 3, pp. 1598–1604, 2003.

[172] P. D. Desai, H. James, and C. Y. Ho, "Electrical resistivity of aluminum and manganese", *Journal of physical and chemical reference data*, vol. 13, no. 4, pp. 1131–1172, 1984.

[173] M. A. Green, "Self-consistent optical parameters of intrinsic silicon at 300k including temperature coefficients", *Solar Energy Materials and Solar Cells*, vol. 92, no. 11, pp. 1305–1310, 2008.

[174] S. Duttagupta, F. Ma, B. Hoex, T. Mueller, and A. G. Aberle, "Optimised antireflection coatings using silicon nitride on textured silicon surfaces based on measurements and multidimensional modelling", *Energy Procedia*, vol. 15, pp. 78–83, 2012.

[175] O. S. Heavens, *Optical properties of thin solid films*. Courier Corporation, 1991.

[176] D. Thorp and S. R. Wenham, "Ray-tracing of arbitrary surface textures for light-trapping in thin silicon solar cells", *Solar Energy Materials and Solar Cells*, vol. 48, no. 1, pp. 295–301, 1997.

[177] P. Ortega, E. Calle, G. von Gastrow, P. Repo, D. Carrió, H. Savin, and R. Alcubilla, "High-efficiency black silicon interdigitated back contacted solar cells on p-type and n-type c-Si substrates", *Progress in Photovoltaics: Research and Applications*, vol. 23, no. 11, pp. 1448–1457, 2015. arXiv: 1303.4604.

[178] J Renshaw, M. Kang, V Meemongkolkiat, A Rohatgi, D Carlson, and M Bennett, "3d-modeling of a back point contact solar cell structure with a selective emitter", in *Photovoltaic Specialists Conference (PVSC), 2009 34th IEEE*, IEEE, 2009, pp. 000 375–000 379.

[179] D. Carrió, P. Ortega, I. Martín, G. López, J. M. López-González, A. Orpella, C. Voz, and R. Alcubilla, "Rear Contact Pattern Optimization based on 3D Simulations for IBC Solar Cells with Point-like Doped Contacts", *Energy Procedia*, vol. 55, pp. 47–52, 2014.

[180] M. Zanuccoli, P. Magnone, E. Sangiorgi, and C. Fiegna, "Analysis of the impact of geometrical and technological parameters on recombination losses in interdigitated back-contact solar cells", *Solar Energy*, vol. 116, pp. 37–44, 2015.

[181] K. Fong, K. Teng, K. McIntosh, A. Blakers, E. Franklin, S. Ngwe, and A. Fell, "Optimisation of n+ diffusion and contact size of ibc solar cells", pp. 851–855, 2013.

[182] P. Procel, V. Maccaronio, F. Crupi, G. Cocorullo, and M. Zanuccoli, "Analysis of the impact of rear side geometry on performance of back-contact back-junction solar cells", in *Photonics Technologies, 2014 Fotonica AEIT Italian Conference on*, IEEE, 2014, pp. 1–4.

[183] P. Procel, V. Maccaronio, F. Crupi, G. Cocorullo, M. Zanuccoli, P. Magnone, and C. Fiegna, "Analysis of the Impact of Doping Levels on Performance of back Contact-Back Junction Solar Cells", *Energy Procedia*, vol. 55, pp. 128–132, 2014.

[184] P. Procel, M. Guevara, V. Maccaronio, N. Guerra, F. Crupi, and G. Cocorullo, "Understanding the Optimization of the Emitter Coverage in BC-BJ Solar Cells", in *Energy Procedia*, vol. 77, Elsevier B.V., 2015, pp. 149–152.

[185] P. Procel, A. Ingenito, R. De Rose, S. Pierro, F. Crupi, M. Lanuzza, G. Cocorullo, O. Isabella, and M. Zeman, "Opto-electrical modelling and optimization study of a novel ibc c-si solar cell", *Progress in Photovoltaics: Research and Applications*, vol. 25, no. 6, pp. 452–469, 2017.

[186] C. Reichel, F. Granek, M. Hermle, and S. W. Glunz, "Investigation of electrical shading effects in back-contacted back-junction silicon solar cells using the two-dimensional charge collection probability and the reciprocity theorem", *Journal of Applied Physics*, vol. 109, no. 2, p. 024 507, 2011.

[187] A. Ebong and N. Chen, "Metallization of crystalline silicon solar cells: A review", in *High Capacity Optical Networks and Emerging/Enabling Technologies*, IEEE, 2012, pp. 102–109.

[188] A. Kalio, A. Richter, M. Hörteis, and S. Glunz, "Metallization of n-type silicon solar cells using fine line printing techniques", *Energy Procedia*, vol. 8, no. April, pp. 571–576, 2011.

[189] E. V. Kerschaver and G. Beaucarne, "Back-contact solar cells: A review", *Progress in Photovoltaics: Research and Applications*, vol. 14, no. 2, pp. 107–123, 2006.

[190] M. M. Desa, S Sapeai, A. Azhari, K. Sopian, M. Y. Sulaiman, N. Amin, and S. H. Zaidi, "Silicon back contact solar cell configuration: A pathway towards higher efficiency", *Renewable and Sustainable Energy Reviews*, vol. 60, pp. 1516–1532, 2016.

[191] M. Hendrichs, M. Padilla, J. Walter, F. Clement, and B. Rech, "Screen-Printed Metallization Concepts for Large-Area Back-Contact Back-Junction Silicon Solar Cells", *IEEE Journal of Photovoltaics*, vol. 6, no. 1, pp. 374–383, 2016.

[192] S. Lee, "Cost effective process for high-efficiency solar cells", *Solar Energy*, vol. 83, no. 8, pp. 1285–1289, 2009.

[193] M Zanuccoli, R De Rose, P Magnone, M Frei, H.-W. Guo, M Agrawal, E Sangiorgi, and C Fiegna, "Numerical simulation and modeling of

rear point contact solar cells", in *Photovoltaic Specialists Conference (PVSC), 2011 37th IEEE*, IEEE, 2011, pp. 001 519–001 523.

[194] M. Zanuccoli, R. De Rose, P. Magnone, E. Sangiorgi, and C. Fiegna, "Performance analysis of rear point contact solar cells by three-dimensional numerical simulation", *IEEE Transactions on Electron Devices*, vol. 59, no. 5, pp. 1311–1319, 2012.

[195] R. De Rose, K. Van Wichelen, L. Tous, J. Das, F. Dross, C. Fiegna, M Lanuzza, E Sangiorgi, A. U. De Castro, and M Zanuccoli, "Optimization of rear point contact geometry by means of 3-d numerical simulation", *Energy Procedia*, vol. 27, pp. 197–202, 2012.

[196] T. Dullweber and J. Schmidt, "Industrial silicon solar cells applying the passivated emitter and rear cell (perc) concept—a review", *IEEE Journal of Photovoltaics*, vol. 6, no. 5, pp. 1366–1381, 2016.

[197] R. Sinton, Y Kwark, S Swirhun, and R. Swanson, "Silicon point contact concentrator solar cells", *IEEE electron device letters*, vol. 6, no. 8, pp. 405–407, 1985.

[198] M. Kim, D. Kim, D. Kim, and Y. Kang, "Impact of laser pulse width on laser ablation process of high performance perc cells", *Solar Energy*, vol. 110, pp. 208–213, 2014.

[199] D. Giaffreda, P. Magnone, M. Meneghini, M. Barbato, G. Meneghesso, E. Zanoni, E. Sangiorgi, and C. Fiegna, "Local shunting in multicrystalline silicon solar cells: Distributed electrical simulations and experiments", *IEEE Journal of Photovoltaics*, vol. 4, no. 1, pp. 40–47, 2014.

[200] A. Goetzberger, J. Knobloch, and B. Voss, "Crystalline silicon solar cells", *editorial John Wiley & Sons Ltd*, vol. 1, 1998.

[201] A. M. Humada, M. Hojabri, S. Mekhilef, and H. M. Hamada, "Solar cell parameters extraction based on single and double-diode models: A review", *Renewable and Sustainable Energy Reviews*, vol. 56, pp. 494–509, 2016.

[202] R. De Rose, P. Magnone, M. Zanuccoli, E. Sangiorgi, and C. Fiegna, "Loss analysis of silicon solar cells by means of numerical device simulation", in *Ultimate Integration on Silicon (ULIS), 2013 14th International Conference on*, IEEE, 2013, pp. 205–208.

[203] V. Tamrakar, S. Gupta, and Y. Sawle, "Single-diode and two-diode pv cell modelling using matlab for studying characteristics of solar cell under varying conditions", *Electrical & Computer Engineering: An International Journal (ECIJ)*, vol. 4, no. 2, pp. 67–77, 2015.

[204] P. Singh and N. Ravindra, "Analysis of series and shunt resistance in silicon solar cells using single and double exponential models", vol. 1, 33–38, Feb. 2012.

[205] M. AlRashidi, K. El-Naggar, and M. AlHajri, "Parameters estimation of double diode solar cell model", *International Journal of Electrical, Computer, Energetic, Electronic and Communication Engineering*, vol. 7, no. 2, pp. 118–121, 2013.

[206] R. De Rose, M. Zanuccoli, P. Magnone, M Frei, E. Sangiorgi, and C. Fiegna, "Understanding the impact of the doping profiles on selective emitter solar cell by two-dimensional numerical simulation", *IEEE Journal of Photovoltaics*, vol. 3, no. 1, pp. 159–167, 2013.

[207] J. Zhao, A. Wang, P. P. Altermatt, S. R. Wenham, and M. A. Green, "24% efficient perl silicon solar cell: Recent improvements in high efficiency silicon cell research", *Solar energy materials and solar cells*, vol. 41, pp. 87–99, 1996.

[208] T. Dullweber, S. Gatz, H. Hannebauer, T. Falcon, R. Hesse, J. Schmidt, and R. Brendel, "Towards 20% efficient large-area screen-printed rear-passivated silicon solar cells", *Progress in Photovoltaics: Research and Applications*, vol. 20, no. 6, pp. 630–638, 2012.

[209] S. W. Glunz, "High-efficiency crystalline silicon solar cells", *Advances in OptoElectronics*, vol. 2007, 2007.

[210] S. Anwar, *Handbook of research on solar energy systems and technologies*. IGI Global, 2012.

[211] R De Rose, M Zanuccoli, P Magnone, D Tonini, M Galiazzo, G Cellere, M Frei, H.-W. Guo, C Fiegna, and E Sangiorgi, "2-d numerical analysis of the impact of the highly-doped profile on selective emitter solar cell performance", in *Photovoltaic Specialists Conference (PVSC), 2011 37th IEEE*, IEEE, 2011, pp. 002556 –002 559.

[212] R. De Rose, M. Zanuccoli, P. Magnone, M. Frei, E. Sangiorgi, and C. Fiegna, "Understanding the impact of the doping profiles on selective emitter solar cell by two-dimensional numerical simulation", *IEEE Journal of Photovoltaics*, vol. 3, no. 1, pp. 159–167, 2013.

[213] G. López, P. R. Ortega, I. Martín, C. Voz, A. B. Morales, A. Orpella, and R. Alcubilla, "Base contacts and selective emitters processed by laser doping technique for p-type ibc c-si solar cells", *Energy Procedia*, vol. 77, pp. 752–758, 2015.